Application of Sweep Frequency Response Analysis and Locked-Rotor Test for Stator Winding Inter-Turn and Broken Rotor Bar Fault Detection of Squirrel-Cage Induction Motors

Prepared By

CHIGOZIE JACOB BONIFACE

Department of Electrical Engineering

University of Cape Town

March 2021

Submitted to the Department of Electrical Engineering at the University of Cape Town in partial fulfilment of the academic requirements for a Master of Science degree in **ELECTRICAL ENGINEERING**

Declaration

This dissertation is submitted to the Department of Electrical Engineering in the Faculty of Engineering and the Built Environment, University of Cape Town, in fulfilment of the requirements for the degree of Master of Science.

I know the meaning of plagiarism and declare that all the work in the document, save for that which is properly acknowledged, is my own. This thesis has been submitted to Turnitin module (or equivalent similarity and originality checking software) and I confirm that my supervisor has seen my report and any concerns revealed by such has been resolved with my supervisor.

CHIGOZIE JACOB BONIFACE

Signed by candidate

March 2021

Acknowledgements

I am deeply grateful to Almighty God for the grace He has given me to complete this study and UCT management for establishing a safe and conducive learning environment.

I am grateful to my supervisor, Prof. P.S Barendse, for his insightful comments, endless suggestions, financial support, most especially my tuition fees all through the duration of my studies and exacting attention to details have been my inspiration and kept my work on track from day one to the final draft of this dissertation.

I am grateful to my parents, Mr., and Mrs. Boniface Ugwu, my cousin, and his wife, Mr., and Mrs. Innocent Nwani, for their unwavering moral support and belief in me and to my siblings for their prayers and words of encouragement. This dissertation is dedicated to them.

I am also grateful to Fabusuyi Akindele Aroge for his guidance and for always been more than a friend even when all hope was lost regarding to personal growth and development. I will never forget your statement, “learn Python programming language to improve your problem-solving skills.”

I wish to show my gratitude to Maysam Soltanian and all the technicians for their technical assistance and electrical equipment provision for my experimental set-up.

I would like to express my deep feelings to Oluchi Augusta Ogbonna for her words of encouragement and spiritual support at the eleventh hour.

Finally, a hearty appreciation goes to Esther Hamatwi, Kingsley Akpeji, Omolola Faloye, Dr. Olufemi Olayiwola, Linda Shelembe, Lebohang Ralikalakala, John Mushenya, Akinola Ajayi-Obe, and other AMES members who have contributed to this project in one way or another.

APPLICATION FORM

Please Note:
Any person planning to undertake research in the Faculty of Engineering and the Built Environment (EBE) at the University of Cape Town is required to complete this form **before** collecting or analysing data. The objective of submitting this application *prior* to embarking on research is to ensure that the highest ethical standards in research, conducted under the auspices of the EBE Faculty, are met. Please ensure that you have read, and understood the **EBE Ethics in Research Handbook** (available from the UCT EBE, Research Ethics website) prior to completing this application form: http://www.ebe.uct.ac.za/ebe/research/ethics1

APPLICANT'S DETAILS		
Name of principal researcher, student or external applicant		CHIGOZIE BONIFACE
Department		ELECTRICAL ENGINEERING
Preferred email address of applicant		chigface@yahoo.com
If Student	Your Degree: e.g., MSc, PhD, etc.	MSc
	Credit Value of Research: e.g., 60/120/180/360 etc	180
	Name of Supervisor (if supervised)	Prof. PAUL BARENDSE
If this is a researchcontract, indicate the source of funding/sponsorship		AMES
Project Title		CONDITION MONITORING OF ENERGY CONVERSION SYSTEM

I hereby undertake to carry out my research in such a way that:

- there is no apparent legal objection to the nature or the method of research; and
- the research will not compromise staff or students or the other responsibilities of the University;
- the stated objective will be achieved, and the findings will have a high degree of validity;
- limitations and alternative interpretations will be considered;
- the findings could be subject to peer review and publicly available; and
- I will comply with the conventions of copyright and avoid any practice that would constitute plagiarism.

SIGNED BY	Full name	Signature	Date
Principal Researcher/ Student/External applicant	CHIGOZIE BONIFACE		**30 Jan 2019**

APPLICATION APPROVED BY	Full name	Signature	Date
Supervisor (where applicable)	Prof. PAUL BARENDSE		**30 Jan 2019**
HOD (or delegated nominee) Final authority for all applicants who have answered NO to all questions in Section1; and for all Undergraduateresearch (Including Honours)	Olabisi Falowo Click here to enter text.		02/04/19 Click here to enter a date.
Chair : Faculty EIR Committee For applicants other than undergraduate students who have answered YES to any of the above questions			

Signatures Removed

Abstract

The field of electromagnetic energy conversion has been dominated by induction motors, where more than 80% are three-phase squirrel-cage induction motors (SCIM) [1], [2]. Despite their flexibility, robustness, and high efficiency, they are susceptible to various types of failures due to external or internal factors. Several studies have shown that 30%-40% [3], [4] and 5-10% [5], [6] of the total failures of induction motor are due to the stator winding breakdown and rotor failures, respectively. Most induction motors have a long service life regardless of types and ratings and warrant minimum maintenance to ensure they work properly. Regular maintenance is recommended to check for signs of insulation damage or other parts that may derate the motor. This reduces motor repair costs, minimizes unscheduled downtime, and enhances industrial processes' reliability [7].

Stator winding faults include inter-turn fault, phase to phase fault, coil to coil fault, and phase to ground fault. The stator winding insulation usually begins with inter-turn faults comprising of a small number of winding turns which makes it more probable than other faults. Manufacturing defects and excessive start-stop cycles or frequent speed changes are mainly the causes of broken rotor bar and end-ring among different rotor fault types [8], but our focus in this study will be on broken rotor bar. Hence, early detection of these faults, both during the manufacturing and operation stages, is essential.

Different techniques have been used for assessing the operating conditions of a rotating machine. One of the more popular techniques is motor current signature analysis (MCSA) [9]-[10], which analyses the spectral content of the stator current in determining the state of health. A popular technique for assessing the stator winding insulation is the DC Hipot test, which involves applying a dc voltage higher than that of the peak ac voltage [11]. Unfortunately, this procedure may lead to winding failure and replacement of the affected coil or winding.

The sweep frequency response analysis (SFRA) approach, developed by Dick and Erven [12], allows for the detection of small changes in the windings due to the effect of short-circuits by analysing the winding impedance over its bandwidth. This technique is mostly used for transformers and very sensitive to inductance and capacitance between winding turns; therefore, any change in the winding geometrical structure can affect frequency response.

Therefore, this project aims to model two devices (inductor to understand better the impedance behaviour of a coil and stator winding) analytically using the impedance transfer function approach. SFRA and locked-rotor test are carried out experimentally on the device under test (DUT) using the impedance transfer function measurement to detect the inter-turn and broken rotor bar fault, respectively. The SFRA technique relies on comparing two measurement results under normal and faults conditions over a wide frequency bandwidth while locked-rotor test relies on a higher excitation current for stator winding impedance extraction as a function of rotor angle to diagnose the SCIM rotor state properly.

The results of this study show that SFRA and locked-rotor test are reliable techniques that enables the detection of damages to SCIM's winding and rotor at their incipient stage before a catastrophic failure occurs. It is observed that inter-turn fault mostly affects the inductive and capacitive region of the impedance response plot which in turns reduces the impedance peak and increases the resonant frequency. The appearance of the sinusoidal profile for the substituted impedance from the locked-rotor test indicates that SCIM rotor bar is faulty. Therefore, applying these two techniques for this study to diagnose SCIM will minimise unplanned outages, thereby reducing repair costs and improving the productivity of the system that uses it.

Table of Contents

List of Figures

List of Tables

Abbreviations

EMDS	Electric Motor-Driven System
IEEE-IAS	Institute of Electrical and Electronics Engineers – Industry Application Society
EPRI	Electric Power Research Institute
IEC	International Electrotechnical Commission
ANNs	Artificial Neural Networks
DUT	Device Under Test
PT	Potential Transformer
CT	Current Transformer
MCSA	Motor Current Signature Analysis
DC	Direct Current
AC	Alternating Current
FRA	Frequency Response Analysis
SFRA	Sweep Frequency Response Analysis
IFRA	Impulse Frequency Response Analysis
CC	Correlation Coefficient
SD	Standard Deviation
DABS	Absolute Average Difference
ASLE	Absolute Sum of Logarithmic Error
FFT	Fast Fourier Transform
DFT	Discrete Fourier Transform
DWT	Discrete Wavelet Transform
CWT	Continuous Wavelet Transform

STFT Short-Time Fourier Transform

EMI Electromagnetic Interference

FEM Finite Element Method

SCIM Squirrel-Cage Induction Motor

NI DAQ National Instrument Data Acquisition

LACOIN Laminated Core Inductor

Chapter 1

Introduction

1.1 Background

Induction machines are electromechanical energy conversion devices that convert electrical energy into mechanical energy in motors and mechanical energy to electrical energy in generators. These machines are reversible in that they can switch easily from the generating to the motoring mode of operation. Induction motors are the most extensively used prime mover in industries and are considered workhorses due to their reliability, low cost, ruggedness, minimal maintenance, and operation. They are applied to most electrical systems used in our daily life, such as air and ground transportations, various cooling systems in electrical devices, home energy conversion systems, and cell phone vibration systems.

About 46% of the world's total electrical energy was estimated to be consumed by electric motor-driven systems (EMDS) [13] and converted into mechanical energy, which is eventually used in the final application or process, such as pumps, compressors, conveyors, high voltage AC systems, etc. More than 80% of the integral horsepower motors are three-phase squirrel-cage induction motors [1], [2]. Despite their flexibility, robustness, and high efficiency, they are susceptible to several types of failures due to environmental or internal factors. Induction motor faults may bring about high energy consumption, drop in efficiency, and unsatisfactory performance if not detected. Therefore, diagnosis of induction motor health is necessary, and this can reduce maintenance costs [14].

Faults in an induction motor can be either mechanical or electrical. These faults can broadly be grouped according to the machine's main components: bearing fault, stator winding fault, rotor fault, and other faults. A survey conducted on 1141 motors under the Motor Reliability Working Group of the IEEE Industry Applications Society (IEEE-IAS) [5], [15], [16] and 6312 motors under the Electric Power Research Institute (EPRI) project [6] respectively, indicates the percentage failure of these components as shown in Fig. 1.1 [5]. The study discovered that stator winding faults are one of the significant causes of induction motor failures.

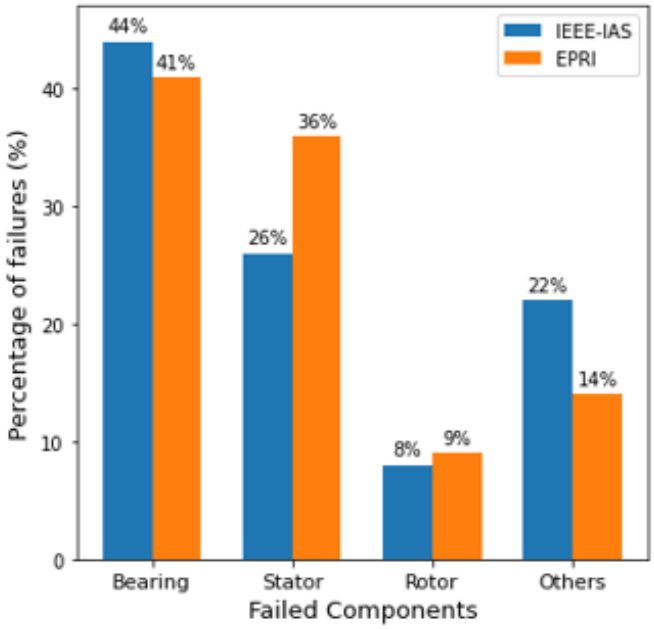

Fig. 1.1: Percentage failure by component in an induction machine

Stator winding failures can be broadly divided into five groups: line to line, line to ground, inter-turn, inter-coil, and winding open faults [17]. These are established categories of electrical faults in an induction motor. Some of the related rotor failures in an induction motor are broken rotor bar fault, rotor mass unbalance fault, bowed rotor fault, etc [18]. Amongst these faults, stator inter-turn and broken rotor bar faults are the most common and will be considered in this study. The inter-turn short-circuit progresses to other winding faults while the broken rotor bar may spread to other bars, leading to fracture of multiple bars of the rotor, resulting in the motor's breakdown if both are not attended to at an early stage. These faults can cause industry production cessation.

This dissertation details the research work done by focusing on impedance measurements for stator winding inter-turn and broken rotor bar faults detection in an induction motor. An initial investigation is first carried out on a silicon steel laminated core inductor to provide the basis for understanding the healthy and faulty condition of a coil. Relevant conditional parameters are also investigated. These involve both analytical and experimental approaches. For fault identification, various existing approaches were reviewed. Some of the limitations are highlighted and discussed. The method and procedures applied are useful for efficient offline stator winding inter-turn and broken rotor bar fault detection of an induction motor to prevent either permanent winding damage or rotor failure.

1.2 Motivation for Research

Induction motors demand protective diagnostic techniques to ensure their continuous operating condition. Once the stator winding on an induction motor has been damaged, the machine's ability to resist further damage is diminished. A squirrel-cage induction motor (SCIM) with a broken rotor bar loses connectivity in the affected bar, which prevents current flow resulting in a magnetic disturbance [19]. An induced current is produced in the stator winding due to the magnetic disturbance linking the stator coil [20]. This induced current distorts the internal symmetry, and consequently, magnetic asymmetry arises [19]. It has been noticed that in SCIM, rotor asymmetry occurs mainly due to manufacturing defects such as during the brazing process and centrifugal forces, which may cause extra stresses on the rotor bars due to heavy end rings of the rotor [18]. There is a need to effectively identify both damages highlighted at its incipient stage and schedule preventative maintenance to avoid a complete interruption of energy delivery. Therefore, determining efficient and reliable fault diagnostic methods is highly important.

Studies relating to the detection of the stator winding and broken rotor bar faults of induction motors have typically been oriented towards the measurement and analysis of vibrations [21], [22], axial leakage flux [23], [24], [25] and stray flux [26]. While these techniques have demonstrated success in identifying induction motor's incipient failures, they demand the use of expensive sensors and are sometimes unsuitable when operating the motor in an unsafe environment. The use of artificial neural networks (ANNs) [27], [28], [29] has been demonstrated for both inter-turn and broken rotor bar fault detection. However, training is essential for their operation using priori fault data which impedes the practical application of such methods, as it is unusual to have comprehensive fault data. An elliptical shape that coincides with the motor current Park's Vector representation was proposed in [30] to detect stator winding inter-turn faults. This method does not give a sharp signature; hence, the distinction between the healthy and faulty induction motor becomes difficult.

There are several occasions where there is a need to verify a machine's integrity or sensitivity, which does not require a complete teardown, such as quality check during maintenance, after transport, or relocation. Literature [31], [32], [33] has shown that frequency response analysis can be used for this purpose without disassembling the motor. Also, most of the work reveals the state of the machine's winding at higher frequencies using the peak magnitude at resonance frequency as indicators. In this study, getting the induction motor stator winding information

under healthy and faulty conditions at low frequencies was considered using impedance transfer function measurement. This will, in turn, reduces the time taken to extract data during the experiment for diagnostic purposes. It is straightforward to carry out with available sinusoidal signal generators and precise measurement equipment. Also, the transfer functions of complicated functions can be determined experimentally which could be extended to non-linear systems. To a limited extent, impedance transfer function measurements have been used as diagnostic tools in electrical machines to detect electrical and mechanical failures. The asymmetry produced due to the broken rotor bar leads to a change in rotor resistance and inductance as a function of rotor position angles. Hence, the impedance parameter of SCIM with a broken rotor bar could be obtained by measuring from the stator side using a locked-rotor test and a pulsating magnetic field. Therefore, in this study, the two fault detection schemes, SFRA and locked-rotor test, will be applied to SCIM with inter-turn and broken rotor bar fault using their impedance transfer function measurements as a diagnostic indicator.

1.3 Objectives of this Study

The main objectives of this research work are:

- Investigate a silicon steel laminated core inductor winding to understand the impedance behaviour of a coil fully.
- Adopt Dowell's equation for the inductor model to include skin and proximity effects.
- Extract the parameters of a laminated core inductor as a function of frequency analytically.
- Experimentally verify the validity of the derived equation for silicon steel laminated core inductor equivalent impedance.
- Conduct a detailed literature review on induction motor diagnostic approaches.
- Induction motor impedance estimation and signal processing will be reviewed.
- Model the stator winding of an induction motor analytically for parameter extraction and impedance behaviour at different frequencies.
- Diagnose a squirrel-cage induction motor with the stator winding inter-turn fault using impedance transfer function method of sweep frequency response analysis (SFRA).
- Compare the impedance response of an induction motor with and without squirrel-cage rotor to investigate the rotor's effect on the stator winding impedance response.

- Investigate the effect of broken rotor bars on the stator winding impedance response at different rotor angles using the impedance transfer function method of SFRA.
- Obtain and compare the substitute impedance of the squirrel-cage induction motor under healthy and broken rotor bar conditions using a locked-rotor test.
- Investigate the effect of current excitation and frequency on change in substitute impedance at different rotor angles using a locked-rotor test.

1.4 Scope and Limitation

This research study focuses on two fault detection schemes for stator winding inter-turn and broken rotor bar fault detection of a squirrel-cage induction motor: sweep frequency response analysis (SFRA) and locked-rotor test at different rotor angle, respectively. A silicon steel laminated core inductor is initially investigated for a detailed understanding of a coil's frequency response. The input current and voltage across the device under test (DUT), such as inductor and stator windings of the induction motor, were the primary measurands to achieve the study's objectives. The effect of broken rotor bars on the stator winding is also investigated using SFRA at different rotor angles.

1.5 Plan of Development

The research presented in this dissertation is divided into the following chapters:

Chapter 2 provides an overview of induction motors with a focus on the stator winding. The inter-turn fault among stator winding faults is reviewed to provide a general understanding of the causes and their impact when not detected for an extended period. The existing diagnostic techniques are also identified with a focus on frequency response analysis.

Chapter 3 includes frequency response analysis focusing on sweep frequency response analysis, and Fast Fourier Transform (FFT) as the major signal processing tool.

Chapter 4 includes a silicon steel laminated core inductor model and parameter extraction from its geometrical structure for impedance behavioural study. The impedance response simulated results and their components (real and imaginary part) are discussed and presented.

Chapter 5 discusses the principles of internal models for rotating machines models. An equivalent circuit consisting of resistance and inductance connected in series and a shunt capacitance for impedance analysis was adopted. An analytical representation for each

parameter was discussed while accounting for skin effect in the stator winding. The results for the simulated series resistance, reactance and equivalent impedance response were also presented. Since the stator winding number of turns is inversely proportional to the percentage number of inter-turn short-circuit faults, the impedance response under these conditions was simulated and presented.

Chapter 6 discusses the experimental setup and testing methodology for impedance response parameter extraction using sweep frequency response analysis and locked-rotor test for inter-turn and broken rotor bar fault detection of each of the devices under test (DUT), respectively.

Chapter 7 discussed and presented the impedance response results for laminated core inductor, SCIM1, and SCIM2 with and without rotor under different winding conditions. The simulated results for SCIM2 impedance response under a healthy and inter-turn fault condition is validated with the experimental result. The imaginary part of the impedance response results and Nyquist plot for each DUT were also presented and discussed.

Chapter 8 discusses the implementation of SFRA on SCIM3 for broken rotor bar (BRB) fault detection. The application of the locked-rotor test for broken rotor bar fault detection at different rotor angles using substitute impedance as an indicator is presented. The effect of current and frequency on the change in substitute impedance for broken rotor bar fault detection at different rotor angles was also investigated and presented.

1.6 Research Outputs

Conference Publications:

1. C. Boniface, P. Barendse, “Impedance Behavioural Study of Silicon Steel laminated Core Inductor”, IEEE SAUPEC/RobMech/PRASA, Cape Town, South Africa, 2020

Papers in preparation:

2. C. Boniface, P. Barendse, “Inter-Turn and Broken Rotor Bar Fault Detection for Squirrel-Cage Induction Motor using the Impedance Transfer Function Measurement”, intended for publication in IEEE Energy Conversion Congress and Exposition, Vancouver Canada, 2021.

Chapter 2

Literature Review of Induction Motor Testing and Diagnostic Techniques for Inter-Turn and Broken Rotor Bar Faults

2.1 Introduction

This chapter presents a literature review on induction machines and associated faults, with testing and diagnostic techniques for stator winding inter-turn and broken rotor bar faults. The general overview of an induction machine and the causes that put them out of service was investigated and discussed.

2.2 Induction Machine

The induction machine is the most widely used in the industry. It can operate both as a motor or generator. It is also called an "asynchronous" machine because its operating speed is slightly less than synchronous motor mode speed and slightly higher than synchronous speed in generator mode, which is rarely used. The induction machine's performance as a generator is not satisfactory for most applications but has been recently found to be well suited for wind-power applications [34]. Induction machine is used in many applications, and in various sizes, e.g., small single-phase induction motor, large three-phase induction motor [35] . The three-phase induction motors are the most common and will be our focus in this study.

2.3 Construction

An induction motor is simply an electric transformer that consists of two relatively movable sections (stator and rotor), one carrying the primary winding (stator) and the other carrying the secondary winding (rotor) separated by an air gap. Electric power is transformed between the stator and rotor with a change of frequency by an electromagnetic field. The active parts (cores, conductors or coils, and air gaps) confine the field as they directly contribute to the energy conversion. The structural parts are essential to the motor's proper operation but do not

contribute to energy conversion. These parts perform the functions highlighted in [36]. The stator of the induction machine consists of [18].

- The motor's outer cylindrical frame is made either of welded shield steel, cast iron, or aluminium alloy, as shown in Fig. 2.1.

Fig. 2.1: Stator frame of induction motor [37]

- The magnetic path, called the core, comprises slotted laminations made of a magnetic substance such as silicon steel pressed into the cylindrical space inside the outer frame, as shown in Fig. 2.2. The core is laminated to reduce losses and heat due to eddy currents.

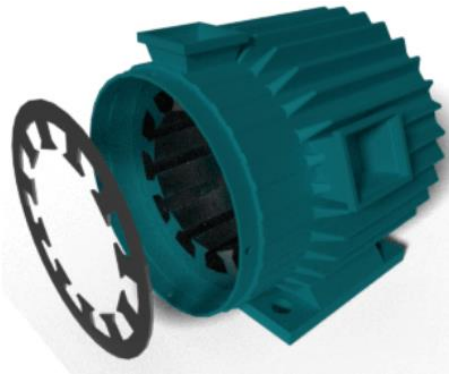

Fig. 2.2: Stator frame with stator core [37]

- A group of insulated electrical windings placed inside the slot of the motor's laminated core.

2.3.1 Types of Stator Winding Construction

The stator winding consists of a one-, two-, or three-phase distributed winding embedded in slots. The motor's winding is termed as distributed because they are not wound as a simple coil but rather wound in a spatially distributed way. A single-phase winding is a system of a group of coils connected in series or parallel. When a coil has one turn only, it is called a single turn

coil. When it consists of more than one turn per coil, then it is called a multiturn coil. Fig. 2.3 shows a coil wound with round wire and a coil group.

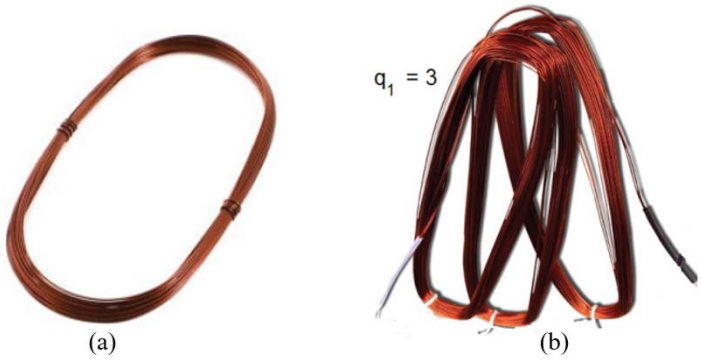

Fig. 2.3: (a) Coil; (b) Coil group wound with round wire [38]

There are three fundamental kinds of constructing stator winding applied to machines ranging from 1 kW to 2 GW [11]:

- **Random-wound stators:** This winding consists of round insulated copper conductors that are wound continuously (by hand or by winding machine) through slots in the stator core to form a coil. They usually operate at voltages greater than or equal to 1000V. Fig. 2.4 shows a portion of a random-wound stator of the induction motor.

Fig. 2.4: A portion of random-wound stator [38]

- **Form-wound stators using multi-turn coils:** This winding is made from insulated coils pre-formed before inserting in the stator core slot and is intended for motors operating at 1000V above.
- **Form-wound stator using Roebel bars:** Most large generators today are not made from multi-turn coils but rather from “half-turn” coils, often referred to as Roebel bars. The Roebel bars are used to prevent mechanical damage to the coil during the insertion

process. With this type of construction, only one half of a turn is inserted into the slot, which is relatively easier than inserting two sides of a coil in two slots simultaneously. Roebel bars are employed in machines with large power output.

Fig. 2.5 shows the circuit diagram of a typical three-phase induction motor stator winding where each phase has one or more parallel paths for current flow. Multiple parallel paths are often necessary as a copper cross-section large enough to carry the entire phase current may result in an uneconomic stator slot size. Each parallel path consists of a few turns of copper conductors formed into a loop.

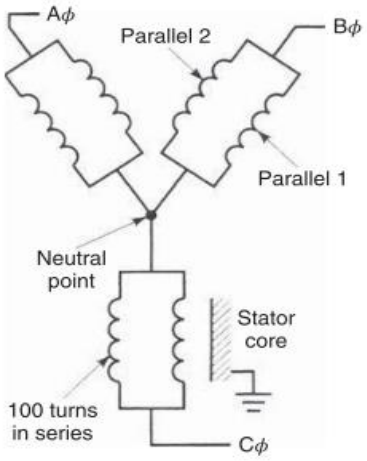

Fig. 2.5: Schematic diagram for a three-phase Y-connected stator winding, with two parallel part per phase [11].

2.3.1.1 Stator Insulation

When conductors are wound into stator slots to form stator windings, electrical insulation is required wherever there is a potential difference between two conductors to prevent a short-circuit. This includes short-circuits of one turn of a coil with adjacent turns, coils with adjacent coils, stator winding with the ground (i.e., stator core), and one phase winding with adjacent phase windings [39]. In an induction motor, the stator insulation system plays a passive role, unlike copper conductors and magnetic steel, which play an active role in magnetic field generation for torque production. It does not help produce magnetic fields or guide its path but has the primary purpose of preventing short-circuits between the conductors or the ground. However, without the insulation, copper conductors would contact one another or the grounded stator core, causing the current to flow in undesired paths and preventing the proper operation of the motor [11].

2.3.2 Types of Rotor Winding Construction

As the name implies, the rotor is the rotating part of an electrical motor in which current is induced by transformer action from a rotating magnetic field. The rotor of the induction motor is of two types: squirrel-cage and wound rotor.

2.3.2.1 Squirrel-Cage Rotor

Induction motors that make use of this type of rotor are known as squirrel-cage induction motors. They consist of aluminium or copper bars embedded in the rotor slots and shorted at both ends by aluminium or copper end rings [35]. It is relatively inexpensive and highly reliable, which is a factor contributing to its immense demand and widespread application. Fig. 2.6 represents a squirrel-cage winding.

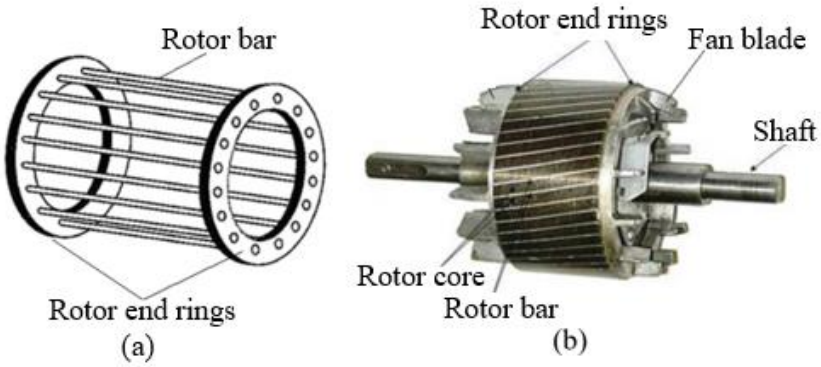

Fig. 2.6: Caged Rotor: (a) cage; (b) complete cage rotor [38]

The complete parts of a squirrel-cage induction motor are shown in Fig. 2.7.

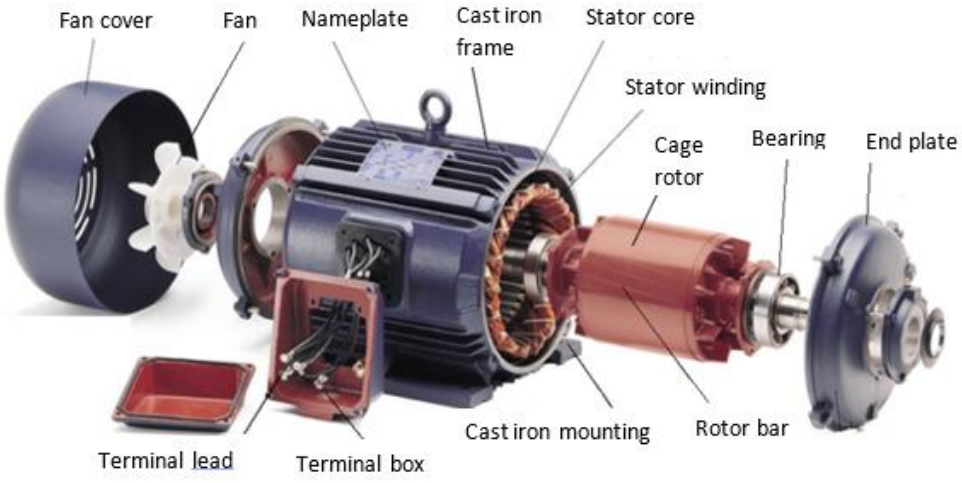

Fig. 2.7: Squirrel-cage induction motor [38]

2.3.2.2 Wound Rotor

Motors that make use of this type of rotor are known as ‘phase-wound’ motors, ‘wound’ rotors, or as ‘slip-ring’ motors. This rotor type has the same form as the stator winding, but its terminals are connected to three slip rings on the motor shaft. At a time when there are no suitable static power converters capable of converting the electrical energy of line-frequency voltages and currents into the energy of variable frequency voltages and currents, an induction motor with wound rotor type was used to alter the rotor speed of line-frequency-supplied induction motors [40]. Fig. 2.8 represents a wound rotor winding.

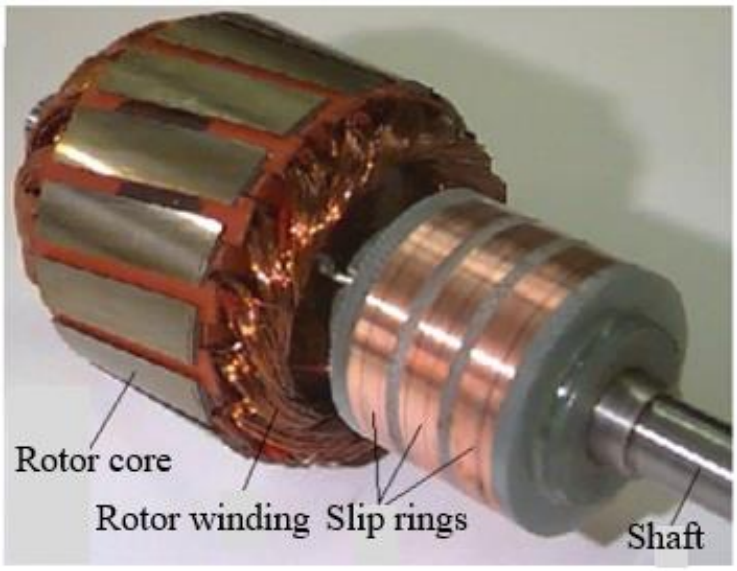

Fig. 2.8: Construction of rotor [38]

2.4 Principles of Rotating Magnetic Field Generation

In a three-phase winding of an induction motor, each phase winding is displaced 120 electrical degrees in space from each other, about stator inner circumference. AC supplied to the stator winding (primary winding) from the electric power supply essentially produces a rotating magnetic field in the air gap whose amplitude and direction depend on the instantaneous value of the current flowing through the winding. When slip (which signifies the difference between the synchronous speed determined by the line frequency and the rotor speed) is present, an electromotive force develops, and an opposing current is induced in the secondary (rotor) winding when it is short-circuited or closed through an external impedance.

The Lorentz force, i.e., the force between the current and the revolving magnetic field, generates the motor’s torque. When the electrical torque is greater than the torque of the load braking the rotor, the motor starts to rotate. However, an induction motor can never reach

synchronous speed; if this occurs, the rotor will appear to be stationary with respect to the rotating stator field since the rotation speed would be the same. No currents would be induced within the rotor, therefore no magnetic field and torque production.

Let the rotor speed be n_r, then the rotor speed deviates from the synchronous speed, n_s by $(n_s - n_r)$. This speed deviation is referred to as the slip speed, which is why an induction motor is called an asynchronous motor [41]. The slip, *s* of an induction motor is usually defined as a fraction of n_s:

$$s = \frac{n_s - n_r}{n_s} \tag{2.1}$$

Thus, the rotor speed is obtained as:

$$n_r = n_s(1 - s) \tag{2.2}$$

The relative motion between the stator and the rotor fields induce voltages in the rotor at a frequency called slip frequency related to the relative speed of the two fields resulting in two intriguing phenomena [34]:

- The rotor fields travel relative to the rotor at the slip speed sn_s
- The rotor itself is mechanically travelling at the speed $(1 - s)n_s$ relative to a stationary observer

So that the net effect is that the rotor field travels at synchronous speed, i.e.,

$$sn_s + (1 - s)n_s = n_s \tag{2.3}$$

What differentiates the induction motor from other electric motors is that the secondary currents are produced solely by induction, as in a transformer, instead of being excited by a DC or other external power source, as in synchronous or DC motor [42].

2.5 Induction Motor Faults

The induction motor may experience several types of faults during operation. Faults could be catastrophic if they are not detected at inception, as they might halt production processes. Understanding the faults associated with the induction motor and its causes can be a great step to preventing their occurrence. The following explains the various type of faults experienced by an induction motor.

2.5.1 Stator Winding Faults

The stator winding insulation system in induction motors is considered one of the most critical components and one of the main sources of stator winding faults. This is because of the combination of various stresses that act on the motor during operation, thereby causing gradual deterioration of the stator winding insulation system and leading to its breakdown at the end of the process [43]. The causes of insulation breakdown that lead to stator winding faults are:

2.5.1.1 Thermal Stresses

Thermal stress occurs due to thermal aging and thermal overloading. As a rule of thumb, for every 10 ºC increase in temperature, the insulation life gets halved due to thermal aging [44]. The typical effect of thermal aging is to render the insulation system vulnerable to other factors that cause failure. Once the insulation system has lost its physical integrity, it will no longer resist the standard dielectric, environmental and mechanical stresses.

Thermal overloading may occur due to variation in the applied voltage, unbalanced phase voltage, obstructed ventilation, cycling, higher ambient temperature, and overloading. As a thumb rule, for every 3.5% voltage unbalance per phase, the winding temperature increases by 25% in the phase with the highest current [44].

2.5.1.2 Electrical Stresses

The electrical stresses that lead to stator insulation failure, which in turn causes stator winding faults, can be classified into the dielectric, tracking, corona, and transient voltage conditions. Dielectric stresses in the insulation winding are divided into three groups, which leads to the significant classification of faults developed in the stator winding of an induction motor: turn-to-turn, turn-to-ground, and phase-to-phase.

The stator winding insulation deterioration process is caused by various stresses acting on the stator where inter-turn or turn-to-turn fault starts an insulation failure between two windings in the stator winding phase.

It is widely believed that stator inter-turn or turn-to-turn faults represent the incipient stage of most winding failures, and its detection has drawn much attention since the early 1980's [45]. This fault produces high currents in the shorted turns, in the order of twice the locked-rotor current and causes severe localized hot-spots. This fault propagates to larger sections if not detected, resulting in severe coil-to-coil faults, phase-to-phase faults, phase-to-ground faults, or open circuit faults, as shown in Fig. 2.9. Failure of insulation between winding and ground can cause a large ground current, resulting in irreversible damage to the induction motor's core.

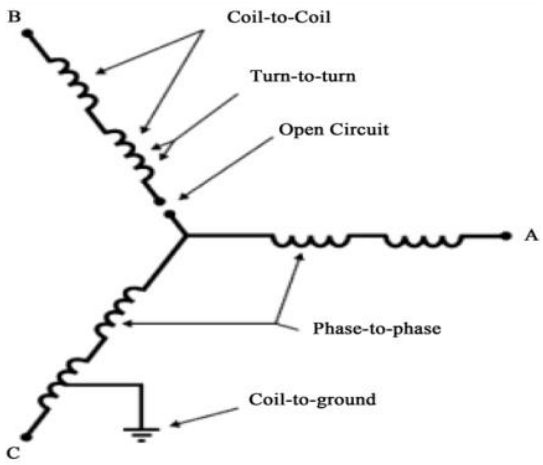

Fig. 2.9: Schematic representation of stator possible failure mode [46]

2.5.1.3 Mechanical Stresses

These stresses could be produced from coil movement or rotor striking the stator. The force on the coils due to the stator winding current is maximum during the starting cycle, causing coils to vibrate twice the line frequency with movement both in the radial and tangential directions. This coil movement could cause damage to the coil insulation, loosen the top sticks, and result in inter-turn or turn-to-turn faults. The rotor could strike the stator winding due to bearing failure, shaft deflection, and rotor-to-stator misalignment.

2.5.1.4 Environmental Stresses

Contamination is the penetration of water, oil, or dust (coal, brush gear sediment) into the stator winding insulation. It degrades the insulation in two ways. First, it causes a reduction in the mechanical or electrical strength of the insulation. Some types of winding insulation are more susceptible than others. For example, insulation made from organic compounds suffers more from water ingress than insulation made from inorganic compounds. Secondly, contamination provides a medium for surface tracking, primarily in the end winding. Surface contamination creates a path for small capacitive currents driven by potential differences within a phase or between phases. These currents lead to surface discharge in the air adjacent to the surface and carbon tracking formation. The low impedance paths formed by these tracks can lead to a fault [47].

2.5.2 Bearing Faults

Most of the induction motors use ball rolling element bearings, consisting of two rings: one inner and the other outer. Under normal conditions with balanced load and good alignment, fatigue may set in. These may lead to increased vibration and noise levels. Other than the usual

internal operating stresses caused by vibration, the bearing can be spoiled by many other external causes such as [48]:

- Improper installation of bearing: by forcing the bearing onto the shaft or in the housing improperly, indentations are formed in the railways (brinelling).
- Improper lubrication, which includes both over and under lubrication causing heating and abrasion.
- Contamination and corrosion are caused by the pitting and sanding action of hard and abrasive minute particles or corrosive water or acid.

2.5.3 Rotor Faults

Rotor faults such as broken rotor bar/end-ring account for about 7-10% of the total faults in induction motors [5], [15], [16]. There are several reasons for which faults in the rotor may occur; these include:

- Thermal stress is produced by thermal overloading and overheating of the rotor, thus causing the cage's thermal expansion.
- Magnetic stresses due to electromagnetic forces and pull due to magnetic imbalance and mechanical stresses are caused by loose laminations.
- Dynamic stresses because of torques in the shaft.
- Environmental stresses because of contamination of the rotor material.

2.5.3.1 Broken Rotor Bar

A broken bar fault produces a relatively significant localized disturbance of the air gap's magnetic flux [49]. They rarely cause immediate failures but reduce the motor's starting and running torque, increasing the motor's run-up time, which increases the rotor and stator temperature, leading to winding insulation damage. If there are enough broken rotor bars, the motor may not start as it may not develop enough accelerating torque.

Broken rotor bars in squirrel cage induction motors (SCIM) could produce axial vibrations on the motor frame at specific frequencies. When this fault occurs, two scenarios exist. Firstly, based on the assumption that no current will flow in the rotor bar, the bar approaches open-circuit conditions, and a magnetic disturbance exists around the bar [8]. This disturbance travels with the rotor and occurs in the localized portion of the air gap. The magnetic disturbance produced by the broken rotor bar links with the stator coils, resulting in an induced current in the stator winding [20]. Secondly, based on the assumption that the current still flows in the

bar through inter-bar currents. The currents enter the bars at the healthy end and flow through the bar's length, leave the bar from the core, and flows to the adjacent healthy bars [20]. This situation often results in the lamination burning due to high contact resistance or localized heat at the bar's contact point and the lamination. This condition could result in a loose bar which could lift and damage the stator core and windings.

Causes of broken rotor bars

The following are some of the conditions that lead to the occurrence of broken rotor bars in induction motors [44]:

- Bars in the region between the core and end-ring are exposed to significant acceleration and deceleration of forces. These forces stress the bar and lead to the occurrence of fracture.
- Skin effect occurs when the motor is started due to migration of currents to the bar's top. This effect creates a temperature gradient over the bar's depth because the top heats faster than the bar's bottom. This uneven expansion stresses the bar and joints, causing failure.
- The unbalanced voltage supply system and harmonics can cause the rotor's excessive heating due to the negative phase sequence and high-frequency currents.

Effects of broken rotor bars

Induction motors with broken rotor bar faults could lead to the following if not detected [50].

- It can cause sparking, which is a critical concern in a hazardous area.
- The healthy rotor bars are caused to carry additional current, leading to rotor core damage.
- It causes torque and speed oscillations in the rotor causing premature wear and tear of bearings and other driven components.
- Broken rotor bars could lift out of the slot due to centrifugal force and strike against the stator winding when rotating at high speed. The sizeable striking force could course the stator lamination to puncture the coil insulation, and a catastrophic winding fault may occur, leading to costly repair and production revenue loss due to unplanned downtime.

2.5.4 Air gap Eccentricity Faults

The non-uniform distance between the rotor and stator in the air gap results in an air gap eccentricity fault. This fault may be generated by bearing defects or manufacturing failure. This

condition creates an unbalanced magnetic flux within the air gap and leads to fault harmonics in the line current, primarily identified in the current spectrum.

Fig. 2.10 shows the summary of the prime sources of induction motor faults due to internal, external, and environmental factors. The internal failures can be distinguished with respect to their sources, i.e., mechanical, and electrical.

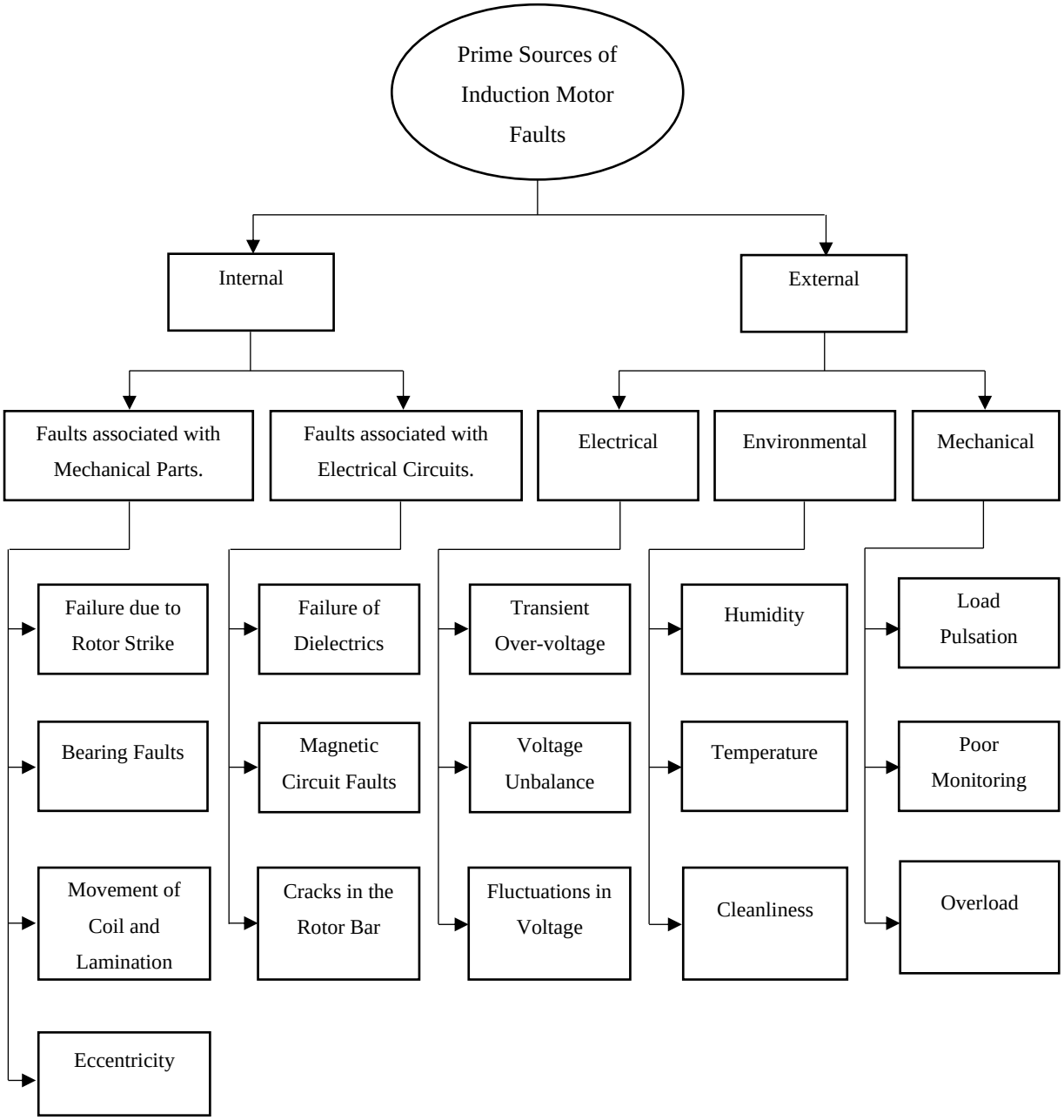

Fig. 2.10: Prime sources of induction motor failures [51]

2.6 Inter-Turn Stator Winding Fault Diagnostic Techniques

It is apparent from the previous sections that insulation failure starts with inter-turn short-circuits within a coil. This fault induces hugely high current flow due to high voltage potential differences between adjacent coils. The high current flowing in the short-circuit produces additional heat and destroys the adjacent coil or windings' insulation. It was reported that this process takes about 20-60sec for small low-voltage motors [52]. In medium voltage motors, this may become faster due to the high voltages between adjacent turns. One of the significant objectives of early diagnosis of stator winding faults is to prevent insulation failure between the winding and ground, which would result in ground currents leading to irreversible damage to the stator core. Hence, detecting the stator winding inter-turn fault at their incipient stage increases the practicability of repairing the motor by rewinding it or, in large motors, displacing short-circuited coils. There are different techniques used for detecting or diagnosing stator winding of induction motor proposed and developed by past researchers. These are now reviewed in detail, with a view of stator inter-turn fault detection as part of this research's focus.

2.6.1 Axial Leakage flux

Axial leakage flux is presented by existing asymmetries in the induction motor, which includes inter-turn faults. Monitoring the frequency components of the flux can be used for detecting inter-turn faults. In this type of approach, the axial leakage flux is sampled by a series of search coils placed axisymmetric to the motor drive shaft and monitored by a spectrum analyser [53], [54]. The harmonics of the axial leakage flux are used as a signature for stator winding inter-turn short-circuit fault detection of induction motor. The assembly of searching coils could be challenging in this technique.

2.6.2 Negative Sequence Components

Fundamentally, symmetrical motors supplied with symmetrical three-phase voltage sources will produce a positive sequence current. When a turn fault occurs, there will be a disturbance in the symmetry, and a negative sequence current will be generated. Experimental and analytical results presented in [55] show the effect of inter-turn short-circuits in the negative sequence current. However, inherent motor asymmetries, mismatched gains, and unbalanced supply voltages may produce a similar effect. Hence, a negative sequence current is not a good indicator for stator winding inter-turn fault detection. A solution to the above challenge was proposed in [56] using apparent negative-sequence impedance as an inter-turn fault indicator.

The negative component impedance behaviour between the current negative component and the positive voltage component was exploited in [57]. Both methods' fault signature is a function of slip, which requires a lookup table with large data memory and complex interpolation for compensation [58].

2.6.3 Motor Current Signature Analysis (MCSA)

This technique has been used by many researchers for condition assessment of induction machines based on voltage or current signal measurements using potential transformers (PT) and current transformers (CT) respectively. These signals are characterized under different load and abnormal conditions like supply voltage imbalance [59], stator faults (opening or shorting of one coil or more of a stator phase winding), broken rotor bar/cracked rotor end, bearing, and gear failure [9], [17], [60]. In MCSA, spectral analysis is performed on the stator current of the motor to extract more information from the measured signals for locating characteristics fault frequencies. The detection of a stator winding fault using MCSA is to detect the frequency components since the axial flux induces corresponding frequencies spectrums in the stator winding [61]. Fast Fourier Transform (FFT) [62], Discrete Wavelet Transform (DWT) [63], Continuous Wavelet Transform (CWT) [64], [65], Cross Wavelet Transform (CWT) [66], Short Time Fourier Transform (STFT) [67], [68], MUSIC Transform [67] and Parks's Vector [66] approach are some of the signal processing techniques found in the literature for fault identification by examining the spectral content. Since MCSA utilizes results from the advanced signal processing of the induction motor's stator current to detect its operating condition, it requires accurate spectrum analysis.

2.6.4 Vibration Analysis

The link between the electrical behaviour and mechanical vibration of induction motors makes detecting internal fault current possible by vibration measurement. Vibration signals are acquired using piezoelectric accelerometers. They are the most widely used instrument for vibration analysis. Piezoelectric accelerometers are installed on the motor casing, which is considered the output of the system. This device converts the vibration signal (electromagnetic vibration of the motor sensed radially) of the induction motor, considered the system's input, into an electrical signal. Further signal processing is carried out on the output signal to detect different motor faults. The major downside is that they are AC coupled and cannot measure the gravity vector or sustained accelerations. The motor condition indicator in this analysis is the vibration amplitude change. The amplitude is formed as a vector sum of individual components, and its change can describe the mechanical or electrical state of the motor [69].

Although results show that some faults are detected, the approach seems less sensitive than those based on the electrical magnitude and complex signal processing that requires high computation [21].

2.6.5 Temperature Monitoring

This approach is based on measuring the induction motor's local temperature and has been used to detect the inter-turn fault in induction motors. In the case of stator winding shorted turns, the stator current will be extremely high, thus generate excessive heat. For motors with a variable speed drive control, there may be additional temperature stress due to the higher harmonic content of the supply, leading to higher losses. This technique gives a meaningful sign of overheating the motor, but this approach has limited fault analysis potential.

2.6.6 Noise/Acoustic Noise

Rapid changes in the air pressure generate noise emanating from induction motors. The spectrum of noise in induction motors is predominant by electromagnetic, acoustic, and ventilation due to air pressure. The electromagnetic noise is generated due to the influence of Maxwell's stresses acting on surfaces of the iron of the motor parts in the existence of the magnetic field [51]. The magnetic force produces vibrations in the structure of the stator, which leads to radiated noise. In [70] and [71], acoustic signals were used to detect the mechanical and electrical faults of commutator motors and three-phase induction motor. The challenge with this mode of diagnosis is the use of a set of microphones. Moreover, acoustic signals are mixed by other signals (reflected waves). The literature review shows that the noise technique for fault diagnosis is less effective than other approaches.

2.6.7 Partial Discharge

Partial discharge occurs either in the slot portion of the coil or at the coil ends close to an induction motor's stator core where the electrical stresses to the ground are high. This condition is due to delimitations within the insulation of the ground wall, resulting from excessive heating. If air-pockets exist in the ground wall due to poor manufacturing, the high electric stress may cause the air's electrical breakdown, resulting in a spark. The electrons and ions in the spark will degrade the insulation and, if not corrected, repeated discharges may eventually erode a hole through the ground wall [11]. The presence of partial discharge activities leads to the stator motor insulating system's degradation phenomena and possible failure in short times [72]. Partial discharge influences the motor, which is a cause of long-term degradation and failure of stator motor insulation. Partial discharge signal amplitude and the number of

pulses/seconds are used to evaluate the induction motor's stator winding's health condition and require complex pattern analysis.

2.6.8 DC Hipot Test

Hipot is a short form for high potential. The DC Hipot test is an over-potential test that is applied to the stator windings of induction motors. In this test, a DC voltage that is substantially higher than that of the peak AC voltage that occurs in regular operation is applied to the winding. The basic idea is, if the winding does not fail because of the high voltage, the winding is not likely to fail soon due to insulation aging when it is placed or returned to service. This testing approach's main problem is that it may cause failure that would not occur for a long time in service, resulting in rewinding or significant repairs before they are needed [11].

2.6.9 Frequency Response Analysis

Frequency response analysis (FRA) is a comparison-based method for electrical apparatus condition assessment, which was first investigated for transformers in depth by Dick and Erven at Ontario Hydro in Canada in the 1970's [12]. It is currently known as one of the most reliable fault detection techniques, and organizations such as IEC, IEEE, and CIGRE standardized it as a routine test for transformers [73], [74]. Since electrical machines are similar to transformers in structure, frequency response analysis has been recently used as a fault detection method for electrical machines.

In [75], it was shown that FRA could be used as a quality control method in the manufacturing industry. Diagnosing the state of the stator windings in electrical motors and transformer windings using the conventional methods has very low sensitivity in detecting winding deformation. Due to short-circuit forces, there could be winding movement and changes to the winding inductance or capacitance in the transformer or induction motor stator winding. Such changes cannot be detected through conventional condition monitoring techniques.

Moreover, the analysis provides information about where winding resonance frequencies are located. The location of these frequencies is linked to the windings' geometrical, which aids in determining internal mechanical changes in the winding. FRA is the primary technique applied in this research for winding diagnosis. Specifically, a voltage is applied to the stator winding of an induction motor, and the corresponding response is measured to determine the impedance spectrum for inter-turn fault detection.

2.7 Broken Rotor Bar Fault Diagnostic Techniques

Various methods of induction motor broken rotor bar fault diagnosis methods have been proposed [76], [77]. The most used techniques are motor current signature analysis (MCSA) [78], [79], vibration analysis [22], leakage flux [25] or artificial intelligence [29]. When the motor operates at a very low slip, MCSA is likely to fail if the rotor fault induced current spectral components are close to the fundamental [77]. Hence, the equivalent circuit of the induction motor will be considered to ascertain rotor condition.

Induction motor (IM) equivalent circuit constitutes a primary, yet sufficiently general mathematical description derived from a corresponding transformer equivalent circuit. The rotor side quantities, which include rotor current, leakage reactance, and resistance, are referred to as the stator. An IM is usually supplied with symmetrical three-phase voltages that contain only the first harmonic. Such measurement only gives precise machine parameters only for symmetric machines [80]. Asymmetry occurs in induction motor due to fault occurrence such as stator winding fault, broken rotor bar fault, e.tc. The effect of broken rotor bars on the stator winding parameters will be considered in this review.

2.7.1 Induction Motor with Broken Rotor Bar Parameter Identification

An induction motor with a broken rotor bar loses connectivity in the affected bar, preventing current flow; hence a magnetic disturbance exists around the bar. This condition distorts the internal symmetry, and consequently, magnetic asymmetry arises, i.e., the rotor MMF distributed along the air gap significantly differs from the ideal sinusoidal function of the first harmonic [19]. This asymmetry leads to a change in rotor resistance and inductance as a function of rotor position. The standard locked-rotor test is designed for a symmetrical rotor. However, this does not consider rotor saliency and must be replaced with an experimental procedure capable of establishing the proper relationship between rotor angle and parameters. Therefore, the only way to extract the asymmetrical motor parameters is with a locked-rotor and a pulsating (non-rotational) magnetic field [81]. The induction motor stator winding is supplied with single-phase voltage while short-circuiting two phases to determine the rotor bar effect on the stator winding, as shown in Fig. 2.11. By changing the rotor's alignment with respect to the stator magnetic axis, a dependence of the motor substitute parameters on rotor angle can be obtained.

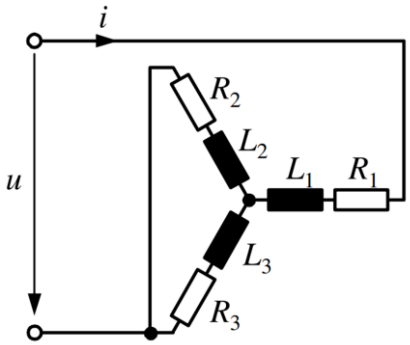

Fig. 2.11: Single-phase measurement of SCIM parameters with broken rotor bar [82]

When the rotor is locked (in short-circuit state), the slip equals one, and most of the current flows through the rotor branch, thus replacing stator and rotor leakage inductances as shown in Fig. 2.12. Hence, the substitute inductance is represented as (2.4):

$$L = \sigma_s L_s + \sigma_r L_r \tag{2.4}$$

And the substitute resistance as (*2.5*):

$$R = R_s + R_r \tag{2.5}$$

Therefore, the substitute impedance magnitude is represented as:

$$|Z| = \sqrt{R^2 + (\omega L)^2} \tag{2.6}$$

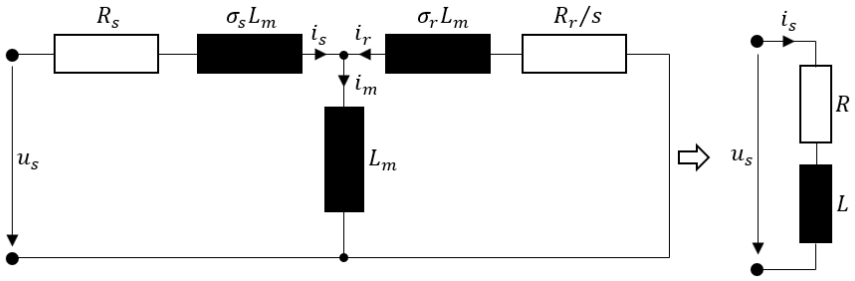

Fig. 2.12: Single-phase equivalent circuit of induction motor [83]

2.8 Conclusions

This chapter presented a theoretical background to induction machine stator components, common failure modes and causes, and some techniques used to determine stator inter-turn and broken rotor bar faults in the induction motor. Little has been done in applying the frequency response analysis (FRA) technique and a locked-rotor test for inter-turn and broken rotor bar fault detection in induction motors using the impedance information measured from the stator side. Hence, both techniques will be used in this study as a diagnostic tool for determining the state of the stator winding and rotor bars in an induction motor.

Chapter 3

FRA and Signal Processing Technique of SCIM due to Mechanical Winding Deformation

3.1 Introduction

The reliability of an induction motor's operation highly depends on the stator winding's electrical and mechanical integrity. These are essential aspects that should be evaluated when examining the motor's overall condition. A motor with minor winding damage could remain in operation; however, it may cause a catastrophic outcome when it later leads to a total failure resulting in forced outages of the unit and a revenue loss.

It was reported in [84] that most rotating machine stator winding failures occur due to loss of mechanical integrity of either overhang conductors or core looseness. Loose coils can occur within the stator slot because of conductor insulation shrinkage or poor construction. Due to this condition, the resistance value is increased, and the damaged area is possibly heated up to critical temperatures [85]. Hence, magnetic forces at twice the line frequency cause the winding to vibrate, which can cause the insulation to wear or separate from the stator core.

At the end winding, excessive vibration may occur due to inadequate bracing. Transient voltage due to opening and closing of a breaker or out of synchronisation produces high transient torque that may cause bracing loosening. A high electromagnetic force (EMF) from a large current that travels into the winding due to the above events could also lead to mechanical damage in the induction motor's stator winding. These conditions produce very large EMFs quickly that can create instability in the stator winding geometrical structure.

3.2 Mechanical Winding Deformation

Induction motor mechanical winding deformation occurs due to the mechanical movement of the physical geometry and constructional parts (coils, winding, core, leads) with respect to each other or the ground in such a manner as to change the internal inductances and capacitances [31]. This movement may be caused by seismic or shipping forces or by in-service conditions

such as load currents, mechanical breakdown of components, or a lightning strike to the power system that causes a short-rise time, high-voltage "spike".

The previous section highlighted that electromagnetic forces could potentially cause damage to the stator winding. When a current-carrying conductor is located within a magnetic field, a force is created and applied to the conductor. The magnitude of this force is given in (3.1).

$$\boldsymbol{F} = L\boldsymbol{I} \times \boldsymbol{B} \tag{3.1}$$

where,

$\boldsymbol{B}$, is the flux density vector in Tesla (T)

$\boldsymbol{I}$, is the current intensity vector in ampere (A)

L, is the conductor length in meters (m).

The equation shows that the winding's electromagnetic forces are proportional to the winding current and the flux density. However, $\boldsymbol{B}$ itself is directly proportional to the current $\left(B = \frac{\mu_0 I}{2\pi r}\right)$. Thus, the electromagnetic force is proportional to the square of the winding current. This shows that during short-circuit, the magnitude of the electromagnetic fields on the winding is significantly higher than those at the nominal current, and such forces may cause damage to the winding [86].

3.3 Frequency Response Analysis

The method of system characterization by analysing its frequency behaviour is called frequency response analysis (FRA). This describes how the amplitude and phase shift of the output relative to the input changes with frequency. It is an accurate, fast, economical, and non-destructive method in detecting winding defects [87].

FRA is a non-intrusive comparison-based monitoring technique for the on-site diagnosis of power transformer winding faults that cannot be easily identified with other traditional techniques, such as partial discharge measurements, MCSA, etc. It gives comprehensive information on the winding mechanical structure and the core and clamping structure [88]. The transformer's and three-phase squirrel-cage induction motor's (SCIM) basic topology and electrical equivalent circuit are nearly identical. Hence, frequency response analysis may be implemented on the induction motor.

3.3.1 FRA Operating Principle

The frequency response characteristics of a system can be found analytically from its transfer function. Therefore, the FRA technique is based on evaluating the equivalent impedance of the windings in the frequency domain. Any phase of the stator winding of an induction motor can be represented as an equivalent circuit, composed of the following parameters: resistance (*R*), inductance (*L*), and capacitance (*C*), in series or parallel connection [89]. Hence, the physical geometry and construction of the induction motor (IM) are integral to its equivalent RLC network. Each stator winding has a unique signature of its transfer function, sensitive to change in this network. Any geometrical (mechanical) change within the IM due to internal faults can cause a change in the capacitive or inductive behaviour of the stator winding, thereby altering the transfer function of the stator winding, causing a variation of its frequency response [90].

The technique is based on applying an input low voltage signal of variable frequency to any terminal of the winding, and the output voltage signal is measured from the other end of the terminal. The voltage measured at the input terminal is called the reference signal, while the voltage measured at the other (output) terminal is called the response signal. FRA's amplitude is determined by the scalar ratio of the response signal to the reference signal as a function of frequency. Fig. 3.1 shows the flowchart of frequency response of impedance ratio.

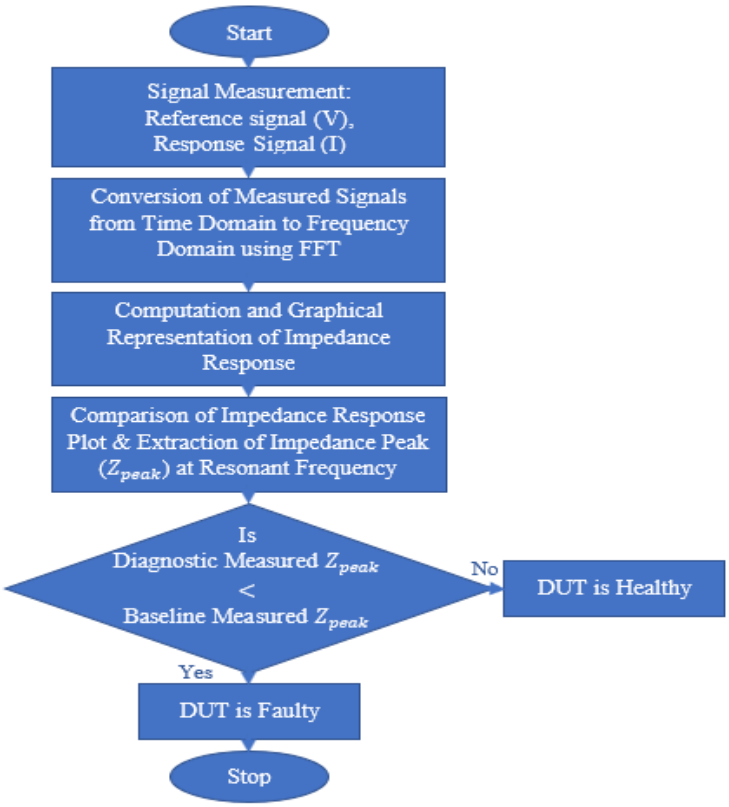

Fig. 3.1: Flowchart of measurement principle of the frequency response of impedance ratio.

The frequency response can be calculated using (3.2) and (3.3):

$$H(jw) = \frac{U_{out}(f)}{U_{in}(f)} \tag{3.2}$$

Because $H(jw)$ is a complex number, frequency response characteristics cannot be graphically displayed as a single curve plotted with respect to frequency. Instead, the magnitude and angle of $H(jw)$ can be separately plotted as functions of frequency [91] called Bode plots.

It is often advantageous to represent the frequency response curves in other scales other than linearly scaled Cartesian coordinates. Bode plots use a logarithmic scale for frequency and a decibel measure for magnitude. Bode plot has the advantage of clearly identifying system features even if they occur over wide ranges of frequency. In Nyquist plots, H(jw) is displayed in Argand (polar) diagram form on the complex number plane, Re[H(jw)] is on the horizontal axis, and Im[H(jw)] on the vertical axis where the frequency is a parameter of such curves [91]. The Bode diagram plots the magnitude and phase as follows:

$$H_{dB} = 20\, log_{10}\, |H(jw)| \tag{3.3}$$

$$\varphi = \varphi_o(U_{out}(f)) - \varphi_o(U_{in}(f)) \tag{3.4}$$

where,

$U_{in}(f)$, is the excitation voltage to the stator winding

$U_{out}(f)$, is the response voltage of the stator winding

$\varphi_o(U_{in}(f))$, is the phase angle of the excitation signal

$\varphi_o(U_{out}(f))$, is the phase angle of the response signal

φ_o, is the phase-frequency characteristic signature

f, is the signal frequency

H_{dB}, is the magnitude characteristics signature in decibel.

3.3.2 Methods of FRA Measurements

According to the input signal, there are two methods associated with frequency response measurements: sweep frequency response analysis (SFRA) and impulse frequency response analysis (IFRA). Both are described in detail below.

3.3.2.1 Sweep Frequency Response Analysis (SFRA) Method

SFRA is a non-intrusive electrical graphical technique that indicates failure in the stator winding and the induction motor's core. The measurement principle is that a low sinusoidal voltage signal feeds the winding terminal via coaxial cable at different frequencies. The other terminal is used to measure the output voltage signal (response signal), also connected via a shielded coaxial cable. The response measurement is done with an impedance of 50 Ω. It is good practice to have each coaxial cable connected between the device's terminal under test (stator winding) and apparatus for adequate impedance measurement. This will result in accurate ratio measurement since the technical parameters of the reference channel and response channel of the measuring instrument are identical to the test leads [92].

The characteristic impedance of the coaxial cable is selected to match the measuring channel's input impedance and minimize signal reflection. This reduces the coaxial cable's effect to the point that it has a little or practically no effect on the defined frequency range measurements.

This FRA method is efficient, simple and indicates failure or changes in the induction motor's winding and core. SFRA has the following advantages [93]:

- Its signal-to-noise ratio is very high.
- An extensive bandwidth can be scanned.
- A more satisfactory frequency resolution at low frequencies could be used. Alternatively, the frequency resolution can be adapted to the frequency band being measured.
- Only one piece of measuring equipment is required.

Sweep frequency response analysis has the following disadvantages [93]:

- Simultaneous determination of more than one transfer function is not possible. This implies that only one measurement can be performed at a time.
- The time taken for each measurement is typically several minutes.

This method is performed by injecting a swept sinusoidal waveform within a predetermined frequency band, as represented in (3.5).

$$\begin{cases} v(t) = Vsin(2\pi f_{sweep} t) \\ f_{min} < f_{sweep} < f_{max} \end{cases} \tag{3.5}$$

where,

V, is the signal voltage amplitude

f_{sweep}, is the variable frequency [Hz].

3.3.2.2 Impulse Frequency Response Analysis (IFRA) Method

The IFRA method uses a single non-periodic signal as excitation or input, injected into the stator winding terminals. The maximum value of input impulse may be in hundreds of volts which causes induced voltages in the remaining end of the stator winding. In comparison with SFRA, IFRA uses less time during the test and can measure several transfer functions simultaneously. Impulse frequency response analysis advantages and disadvantages are also highlighted in [93].

The test configurations used for making FRA measurements, methods to assess the measured traces of either SFRA or IFRA, and the two categories for applying FRA measurements are explained in Appendix A.

3.3.3 Transfer Function

The transfer function is the mathematical representation of a system which is defined as the ratio of output to the input of a linear time-invariant system with zero initial conditions. The transfer function also depicts the rudimental characteristics of a network and is a valuable tool in modelling such a system. A system block diagram of a transfer function is shown in Fig. 3.2, where *U(s)* is the input signal, *Y(s)* is the output signal, and *H(s)* is the transfer function of the system.

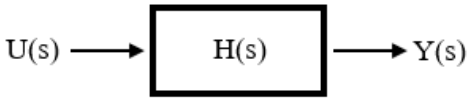

Fig. 3.2: System representation of a transfer function [94].

A linear input/output system is described by the differential equation in (3.6) [95]:

$$\frac{d^n y}{dt^n} + a_{n-1}\frac{d^{n-1} y}{dt^{n-1}} + \cdots + a_0 y = b_{n-1}\frac{d^{n-1} u}{dt^{n-1}} + \cdots + b_0 u \tag{3.6}$$

Two polynomials completely describe the differential equation:

$$U(s) = s^n + a_{n-1}s^{n-1} + \cdots + a_1 s + a_0 \tag{3.7}$$

$$Y(s) = b_n s^n + b_{n-1}s^{n-1} + \cdots + b_1 s + b_0 \tag{3.8}$$

The frequency response can be expressed by a transfer function of the form (3.9):

$$H(s) = \frac{Y(s)}{U(s)} = \frac{b_n s^n + b_{n-1} s^{n-1} + \cdots + b_0}{a s^n + a_{n-1} s^{n-1} + \cdots + a_0} \tag{3.9}$$

The transfer function is represented in the frequency domain by $s = j\omega$ and denoted by the Fourier variable $H(j\omega)$, where $(j\omega)$ denotes the presence of a frequency dependent function, and $\omega = 2\pi f$. The Fourier relationship for the input and output transfer function is given by:

$$H(j\omega) = \frac{Y(j\omega)}{U(j\omega)} \tag{3.10}$$

When a transfer function is reduced to its simplest form, it generates a ratio of two polynomials. The transfer function's physical interpretation depends on the system parameters regardless of the input and output signal. The main characteristics, such as half-power and resonance, occur at the roots of the polynomials. The numerator roots are referred to as 'zeros' which produces an increase in gain, while the denominator's roots are 'poles', which causes attenuation. Transfer functions also represent the variation of both the magnitude and phase angle with respect to the frequency [96]. Conventionally, there are two types of transfer functions used in applying FRA analysis for fault detection or assessing the integrity of an induction motor's stator winding. These are [93], [97], [98]:

- Voltage ratio transfer function, which is represented as (3.11):

$$H(j\omega) = \frac{V_{out}(j\omega)}{V_{in}(j\omega)} \tag{3.11}$$

- Impedance and admittance transfer function, which is represented as (3.12) and (3.13):

$$H(j\omega) = \frac{V_{out}(j\omega)}{I_{in}(j\omega)} \tag{3.12}$$

$$H(j\omega) = \frac{I_{in}(j\omega)}{V_{out}(j\omega)} \tag{3.13}$$

The sensitivity of each transfer function to detect changes in the induction motor assemblies is very different. Therefore, the most sensitive method must be applied to diagnose stator winding faults in the induction motor properly. In this study, the impedance transfer function method is adopted to enable experimental and stator winding model impedance validation. The physical geometry of induction motor stator winding could be represented as an equivalent circuit composed of resistance, inductance, and capacitance.

3.3.4 Application of FRA Measurement

There are two distinct categories for the application of FRA measurements: baseline measurement and diagnostic measurement. The procedure and precautions to produce a good measurement are both the same. However, there is a difference in the motivation for the tests in each category [73] which is explained (in Appendix A).

3.3.5 Statistical Analysis for Comparing Frequency Responses

The comparison of FRA results is usually made by plotting a graph of the magnitude against frequency for both sets of measurement where an experienced observer then examines the curves for any significant differences [99]. Three methods may analyse the results. They are:

- Monitoring changes of the curves.
- Creation of new resonant frequencies or the elimination of existing resonant frequencies.
- Monitoring significant shifts in the existing resonant frequencies.

The main challenge with this comparison method is that the expert's opinion may lack objectivity and transparency. One way to address both problems is to note down all the resonant frequencies. This gives objective and transparent information on the number of resonances that have been created or eliminated and how far any resonance may have been shifted.

An alternative way is to calculate statistical indicators of the agreement between the two sets of measurements. This amounts to a more objective and transparent way of performing a comparison between two measurements as it extracts information from the results across the whole of the repeatable range [99]. This approach measures the difference between two frequency responses rather than only comparing visually from the plot. This method provides a single value on the extent of variation between them.

FRA traces are expressed as a magnitude and phase vector with discrete elements where each element corresponds to one frequency sample. These indicators are calculated directly from the FRA traces, which may be in original form or dB scale without additional computations, making it easier to implement [100].

Some of the statistical indicators used for FRA are correlation coefficient (CC), standard deviation (SD), the absolute average difference (DABS), and the absolute sum of logarithmic error (ASLE). They are defined as follows [100], [101]:

$$CC = \frac{\sum_{i=1}^{N} \boldsymbol{X}(i)\boldsymbol{Y}(i)}{\sqrt{\sum_{i=1}^{N}[\boldsymbol{X}(i)]^2 \sum_{i=1}^{N}[\boldsymbol{Y}(i)]^2}} \tag{3.14}$$

$$SD = \sqrt{\frac{\sum_{i-1}^{N}\left(\boldsymbol{Y}(i) - \boldsymbol{X}(i)\right)^2}{N-1}} \tag{3.15}$$

$$DABS = \frac{\sum_{i}^{N} |\boldsymbol{X}(i) - \boldsymbol{Y}(i)|}{N} \tag{3.16}$$

$$ASLE = \frac{\sum_{i=1}^{N} |20\, log_{10}\, \boldsymbol{Y}(i) - 20\, log_{10}\, \boldsymbol{X}(i)|}{N} \tag{3.17}$$

where,

Y and ***X***, are the magnitude vectors of the new and the fingerprint traces respectively

Y(*i*) and ***X***(*i*), are the i^{th} elements of these vectors

N, is the number of samples in a vector.

The most employed among these statistical indicators is the correlation coefficient (CC), also known as the cross-correlation factor or coefficient in some literature. If CC is unity, both traces are the same; otherwise, one is deviated from healthy.

3.3.6 The Fourier Transform and FFT Algorithm

Fourier analysis forms the basis for much of digital signal processing. The Fourier transform has long been applied for linear systems characterization and identification of the different frequency sinusoids (and their respective amplitudes) or components combined to form a continuous waveform [102]. The Fourier transform allows a signal in the time domain to be converted into its equivalent representation in the frequency domain. Conversely, the inverse Fourier transform enables the corresponding time domain signal to be determined if the frequency response of a signal is known. Mathematically, the Fourier transform pair for continuous signals can be written as (3.18):

$$X(f) = \int_{-\infty}^{\infty} x(t) e^{-j2\pi ft} dt \tag{3.18}$$

The inverse transform is represented as (3.19):

$$x(t) = \int_{-\infty}^{\infty} X(f) e^{j2\pi ft} df \tag{3.19}$$

where,

$x(t)$, is the waveform to be decomposed into a sum of sinusoids

$X(f)$, is the Fourier transform of $x(t)$ for $-\infty < f < \infty$ and $j = \sqrt{-1}$.

Many applications involving the continuous Fourier transform rely on a digital computer for implementation, which leads to the use of the discrete Fourier transform (DFT) and can be defined for a finite duration discrete signal X[n] as [103]:

$$X[n] = \sum_{k=0}^{N-1} x[k] e^{-j2\pi nk/N} \tag{3.20}$$

$$n = 0, 1, \quad . \; . \; . \quad , N-1$$

The discrete inverse Fourier transform is given by (3.21):

$$x[k] = \frac{1}{N} \sum_{n=0}^{N-1} X[n] e^{j2\pi nk/N} \tag{3.21}$$

$$k = 0, 1, \quad . \; . \; . \quad , N-1$$

A published work on the Fast Fourier Transform (FFT) algorithm to calculate DFT in [104] was a turning point in digital signal processing and some areas of numerical analysis. They presented that the DFT, which was previously thought to be N^2 arithmetic operations, could be determined by the new FFT algorithm using only $NlogN$ operations [103] where N is the problem size. For instance, an 8192 points DFT, which takes about 30 minutes of computer time when conventional integration programming is used, can be computed less than 5 seconds with the algorithm [105]. Hence, FFT is a fast algorithm, i.e., of low complexity, for the computation of the discrete Fourier transform (DFT).

3.4 Conclusion

This chapter presented a detailed study of the frequency response analysis technique. The various measurement methods required for valid impedance measurement were presented. The advantages and disadvantages of those methods were also noted. Specifically, SFRA was discussed in detail as it forms the basis for this research. Besides visual comparison for FRA results, the use of statistical indicators to enhance result assessment was presented. Finally, FFT as the major tool for signal processing in this research was presented.

Chapter 4

Frequency Response Model of a Silicon Steel Laminated Core Inductor

4.1 Introduction

Silicon steel magnetic properties are the key factors in the design and performance optimization of electrical apparatus [106]. This is employed in alternators that generate electric power and transformers, which step up or down voltage during electric power transmission. The winding of a rotating machine is made up of several coils connected in series or parallel. An inductor (coil) is formed when a conductor is wound around a laminated core. Studying this device's behaviour (inductor) will aid the modelling of the stator winding of the squirrel-cage induction motor and interpret the experimental results for fault detection. A laminated core is mostly used in electrical devices due to the following reasons: low hysteresis loss, high saturation, high permeability, high electrical resistivity, virtually eliminating ageing, and moderate loss at audio frequency.

An induction motor's stator frame consists of laminations of silicon steel magnetic material, usually with a thickness of about 0.5mm. The purpose of this magnetic core is to reduce the reluctance, increase inductance as well as the magnetic flux, obtain a well-defined path length (MPL), link the energy stored in the air gap to the winding by a low reluctance flux path, contain the magnetic flux in the core, reduce leakage inductance and electromagnetic interference (EMI) level.

Knowing the geometry and material used in the construction of a laminated core inductor can enable us to determine its behaviour and parameters of its equivalent circuit [107]. This motivated the behavioural study of an inductor with a round conductor winding around a silicon steel laminated core considered at different frequencies [108]. Dowell's equation for round conductor winding will be adopted in this study.

4.2 Inductor Model

Inductors are devices that allow direct current (DC) signals to pass through without minimal impediments but, will block the passage of high-frequency signals. It has very low resistance for low-frequency signals while displaying very high resistance for high-frequency signals. An ideal inductor has the following properties:

- The impedance is purely reactive and proportional to the inductance only.
- The phase of the signal across an ideal inductor would always be +90° out of phase with the applied voltage.

A non-ideal inductor exhibits both resonance and non-linear characteristics. A silicon steel laminated core inductor will exhibit these characteristics since it is a non-ideal inductor. The requisite for accurate physical modelling is identifying the relevant parasitic parameters of the device and their effects. An inductor's main objective is to store magnetic energy, but the inevitable resistance of the wire and its self-capacitance due to skin effect at high frequencies alters its behaviour and is considered parasitics [109].

The parasitic resistance dissipates energy through ohmic losses, while the parasitic capacitances store unwanted electric energy. Eddy currents cause the alternating current energy dissipated through ohmic losses. Eddy currents distort the main current movement through the inductor and consists of two effects: the skin and proximity effect. Hence, an inductor could be modelled using a lumped parameter circuit consisting of passive elements such as resistance, inductance, and capacitance connected in parallel.

Fig. 4.1 (a), shows a detailed inductor equivalent circuit that comprises of passive elements such as, resistance, inductance, and capacitance; its equivalent series circuit comprises of an equivalent series resistance and reactance.

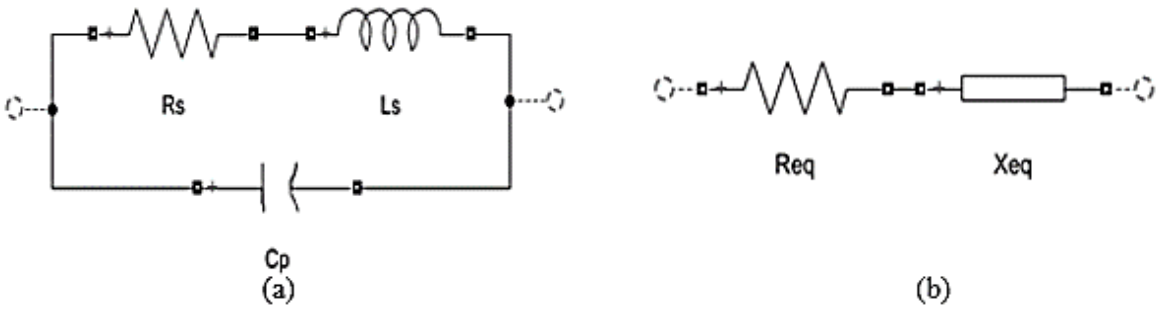

Fig. 4.1: Inductor: (a) lumped equivalent parameter circuit, (b) equivalent series circuit.

To simulate an inductor's impedance behaviour, a silicon steel EI laminated core inductor was built in the laboratory composed of 350 turns of 0.686mm copper wire. The inductor's geometrical parameters (winding and EI lamination core) were extracted from the datasheet and presented in Table 4.1, to model its impedance response using the equivalent circuit accurately. The circuit parameters in Fig. 4.1 were determined using the geometrical parameters and plotted as a function of frequency to better analyse and understand the laminated core inductor's impedance behaviour.

Table 4.1: Silicon steel laminated core inductor parameters

Symbol	Quantity	value
d_i	Bare wire diameter (mm)	0.644
d_o	Outer wire diameter (mm)	0.686
N_l	Number of layers	3
N	Number of turns	350
A_c	Core cross sectional area (mm^2)	765
l_c	Length of the laminated core (mm)	76.2
l_g	Length of the air gap (mm)	0.6
R_{wdc}	DC winding resistance (Ω)	3.8612
C_p	Total parasitic capacitance (pF)	19.338
s	Lamination thickness (mm)	0.35
μ_{rc}	Relative permeability of the FeSi	400
l_T	Mean length per turn (mm)	208.44
ϵ_r	Relative permittivity of the insulating coating	6.2

4.3 Eddy Current Effect - Skin and Proximity Effect

According to Faraday's law, if a conductor is subjected to a time-varying magnetic field, a voltage is induced in a conductor loop. This voltage forces eddy currents to circulate in the conductor in a closed path. An isolated round and straight conductor carrying a time-varying current generate a time-varying circular magnetic field inside and outside the conductor. This depends on the instantaneous current, the time rate of change of the current, and the radial distance from the conductor's centre. The field inside the conductor induces opposing eddy currents within the conductor, which flows in the opposite direction to the applied current in the centre of the wire and in the same direction near the surface. The net instantaneous current in the conductor is unchanged by the eddy currents; instead, it is the radial distribution of the current over the conductor's cross-section that changes [110].

As a result, there is a cancellation of current flow at the conductor's centre, and most of the current flow is concentrated near the surface or outer skin of the conductor. The most significant current density is at the conductor's surface and decays with distance towards the interior. Thus, the current distribution in the conductor becomes non-uniform.

The intensity of the induced eddy currents is directly proportional to the rate of change of the main current; therefore, the current's non-uniform distribution is more pronounced for higher frequency excitations [110]. This change in conductor current density is referred to as the skin effect, and its depth is called the skin depth. Due to this effect, the conductor's AC resistance increases and becomes higher than the DC resistance. It is important to note that the redistribution of the current due to skin effect depends solely on the magnetic field induced by the alternating current in the conductor itself, as shown in Fig. 4.2. At very high frequencies, the current flows in a thin skin surface, and the inner region of the conductor plays no role in the current conduction.

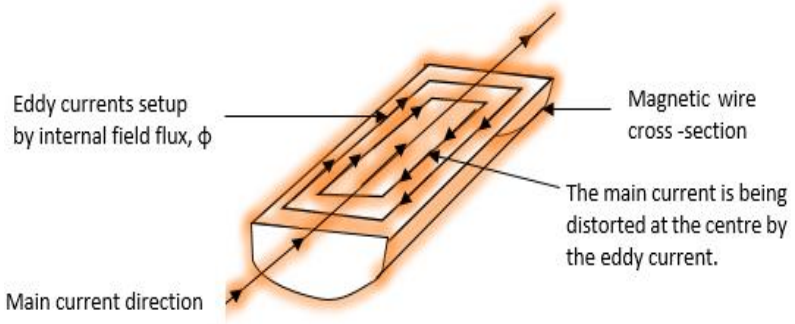

Fig. 4.2: Eddy current in a conductor carrying current [111]

Another type of frequency-dependent eddy current phenomenon occurs in any conductor placed in a region of space containing an externally generated time-varying magnetic field with a normal component to conductor's axis. Whenever this occurs, there are eddy currents induced in the conductor, which oppose the external magnetic field penetration. Since this external field can be caused by alternating current in some other nearby conductor, this eddy current phenomenon is often referred to as the proximity effect [110].

The two eddy current effects discussed, skin and proximity effects, occur simultaneously in a conductor that carries alternating current and is positioned in an external alternating field. This situation exists for the conductors in a laminated core inductor or induction motor's stator winding. The essence of the combination of these effects is that the current in each conductor produces a skin effect and a proximity effect in other conductors that are close to it. The

circulating eddy currents due to these effects increase the power dissipation in the laminated core inductor or stator winding with increasing frequency. The skin depth is easily calculated from (4.1) and plotted as shown in Fig. 4.3:

$$\delta_w = \sqrt{\frac{\rho_w}{\pi \mu_o \mu_{rw} f}} \tag{4.1}$$

where,

$\mu_o = 4\pi \times 10^{-7} H/m$, is the permeability of free space

μ_{rw}, is the conductor relative magnetic permeability, which is 1 for copper wire

$\rho_w = 17.24 \times 10^{-7} \Omega m$, is the resistivity for a copper wire at a temperature 20℃

f, is the frequency in Hertz.

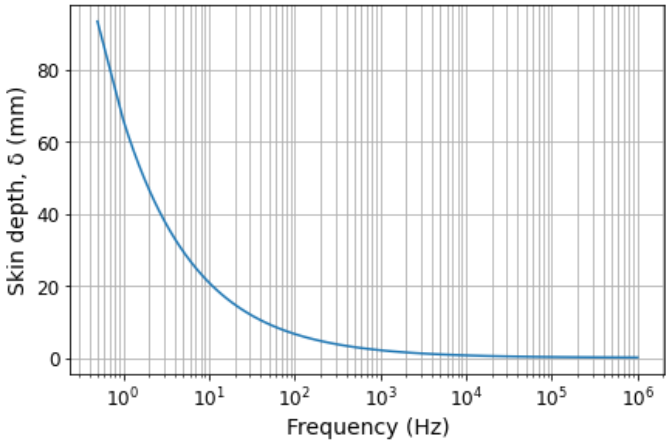

Fig. 4.3: Conductor skin depth as a function of frequency

4.4 Winding Series Resistance

The winding series resistance depends on the operating frequency (high or low), which comprises the winding AC resistance, $R_{w(ac)}$ and core resistance, R_c. The winding series resistance can mathematically be represented as in (4.2) [112]:

$$R_s = R_{w(ac)} + R_c \tag{4.2}$$

4.4.1 Winding DC Resistance

The winding direct current resistance specification of an inductor is the amount of resistance it has to signals with frequencies of or near 0Hz. The direct current resistance of an inductor is measured using a direct current (DC) source. The direct current is fed into the inductor, and the

resistance is calculated using ohm's law (4.3) by measuring the voltage (*V*) across the inductor and current (*I*) flowing through the inductor.

$$R_{w(dc)} = \frac{V}{I} \tag{4.3}$$

Since, for low-frequency operation, the conductor winding resistance of an inductor is approximately equivalent to the DC winding resistance, $R_{w(dc)}$, this can also be calculated using the geometry of the inductor and conductor properties. The DC winding resistance of an inductor with mean length per turn, l_T, number of turns, and winding resistance per unit length, r_L, can be calculated as in (4.4):

$$R_{w(dc)} = r_L N l_T \tag{4.4}$$

The winding resistance per unit length is determined using (4.5):

$$r_L = 4\rho_w/\pi d^2 \tag{4.5}$$

where,

$\rho_w = 17.24 \times 10^{-7} \Omega m$, is the resistivity for a copper wire at a temperature 20℃

d, is the copper diameter of a round wire.

4.4.2 Winding AC Resistance

Skin effect increases the series resistance at high frequencies by restricting the wire's conducting area to a thin skin on its surface. As a result, the total current carrying area is less than the entire wire area; therefore, AC resistance is higher than the DC resistance. As the frequency increases, the skin depth decreases, which leads to non-uniformity of the current density in the conductor. At high frequencies, the AC resistance becomes higher than the DC resistance. There are many methods being proposed and utilized for the resistance calculation [113], [114], [115], [116]. Among these, Dowell's approach is one of the most referenced. The expression for the winding AC resistance, $R_{w(ac)}$ of a round cross-sectional area conductor wound around a laminated core inductor, is given in [117] as (4.6):

$$R_{w(ac)} = F_R R_{w(dc)} \tag{4.6}$$

F_R is the ac-to-dc winding resistance ratio which can be expressed as (4.7):

$$F_R = A\left[F_{RS} + 2\frac{N_l^2 - 1}{3}F_{RP}\right] \tag{4.7}$$

where,

N_l, is the number of layers in the winding

F_{RS} and F_{RP} represent the winding AC resistance due to skin and proximity, which are expressed as (4.8) and (4.9) respectively:

$$F_{RS} = \frac{e^{2A} - e^{-2A} + 2Sin(2A)}{e^{2A} + e^{-2A} - 2Cos(2A)} \tag{4.8}$$

$$F_{RP} = \frac{e^{A} - e^{-A} - 2Sin(A)}{e^{A} + e^{-A} + 2Cos(A)} \tag{4.9}$$

Therefore, equation (4.6) becomes (4.10):

$$R_{w(ac)} = F_R R_{w(dc)} = R_{w(dc)} A \left[F_{RS} + 2\frac{N_l^2 - 1}{3} F_{RP} \right] \tag{4.10}$$

Substituting (4.8) and (4.9) into (4.10), we have (4.11):

$$R_{w(ac)} = R_{w(dc)} A \left[\frac{e^{2A} - e^{-2A} + 2Sin(2A)}{e^{2A} + e^{-2A} - 2Cos(2A)} + 2\frac{N_l^2 - 1}{3} \cdot \frac{e^{A} - e^{-A} - 2Sin(A)}{e^{A} + e^{-A} + 2Cos(A)} \right] \tag{4.11}$$

where,

A, is a dimensionless quantity which depends on the conductor winding geometry and for round wire the quantity *A* is expressed in [118] as (4.12):

$$A = \left(\frac{\pi}{4}\right)^{3/4} \frac{d_o}{\delta_w} \sqrt{\eta} \tag{4.12}$$

d_o, is the copper outer diameter of a round wire

$\eta = d_o/t$, is the porosity factor for a round wire

t, is the distance between the centres of two adjacent conductors or the winding pitch

δ_w, is the skin depth of the conductor.

4.4.3 Magnetic Core Resistance

The core resistance of a laminated core inductor depends on the core inductance at DC or low frequencies, the skin depth at high frequencies, and the lamination sheet's thickness. A thin laminated sheet is considered in this study because of the advantages of not affecting the inductor's magnetic performance at low frequencies and reduced eddy current losses. The

expression for the core equivalent series resistance, related to the power loss due to eddy currents flowing in the core, is derived in [112] as (4.13):

$$R_C = \omega L_{m(dc)} \frac{\delta_c}{s} \frac{Sinh\left(\frac{s}{\delta_c}\right) - Sin\left(\frac{s}{\delta_c}\right)}{Cosh\left(\frac{s}{\delta_c}\right) + Cos\left(\frac{s}{\delta_c}\right)} \tag{4.13}$$

The core skin depth, δ_c is given as (4.14):

$$\delta_c = \sqrt{\frac{\rho_c}{\pi \mu_e f}} \tag{4.14}$$

and the DC (low frequency) inductance is expressed as (4.15):

$$L_{m(dc)} = \frac{\mu_e N^2 A_c}{l_c} \tag{4.15}$$

The equivalent magnetic permeability, μ_e is expressed in (4.16) as:

$$\mu_e = \mu_{rc} \frac{l_c}{l_c + \mu_{rc} l_g} \tag{4.16}$$

where,

s, is the thickness of the laminated silicon steel

ρ_c, is the resistivity of the laminated silicon steel core

N, is the number of turns

A_c, is the effective cross-sectional area of the central limb

l_c, is the axial length of the laminated silicon sheet

μ_{rc}, is the relative permeability of the laminated silicon steel

l_g, is the length of the air gap.

Fig. 4.4 shows the plot of winding series, core, and winding resistance. The eddy current effect on the windings increases the resistance values at different frequencies.

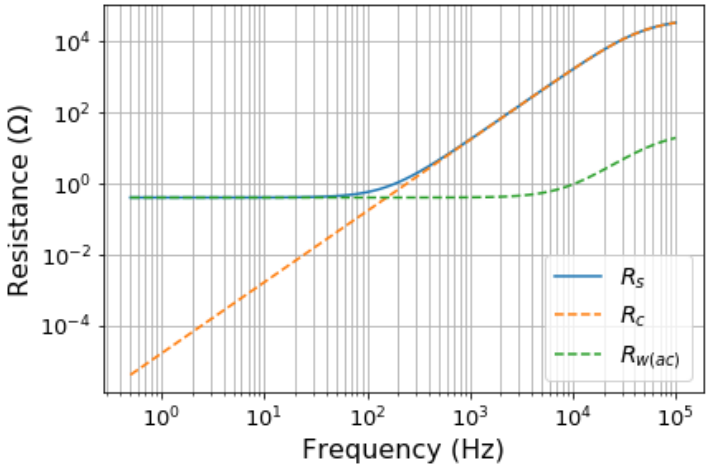

Fig. 4.4: Winding series resistance, core, and winding resistance as a function of frequency

4.5 Winding Series Inductance

The winding series inductance of an inductor depends on the winding, bobbin, core geometry (for instance, silicon steel laminated core), the permeability of the core material, and the operating frequency. The inductance is frequency-dependent because the permeability of the magnetic core depends on frequency. Conductor inductance reduces due to skin effect at high frequencies because the non-uniform current density alters the internal magnetic flux linkage. The winding series inductance of a silicon steel laminated core inductor is the sum of the winding leakage inductance, L_{leak} and the core inductance, L_c as (4.17):

$$L_s = L_{leak} + L_c \tag{4.17}$$

4.5.1 Winding Leakage Inductance

The winding leakage inductance, L_{leak} due to the magnetic field, also depends on frequency; decreasing as frequency increases due to skin and proximity effects caused by the eddy currents in the laminated core. Thinner laminations of about 0.35mm and SiFe (silicon steel, 2.5% of Si) of $45 \times 10^{-6}\Omega m$ with resistivity, were used to reduce the effect of core eddy currents. The winding leakage inductance was derived in [117] and simplified in (4.18) as:

$$L_{leak} = F_L R_{w(dc)} \tag{4.18}$$

In (4.18), F_L is the ratio of the winding AC inductance to the winding DC resistance expressed in (4.19) as:

$$F_L = \frac{A}{\omega}\left[F_{LS} + 2\frac{N_l^2 - 1}{3}F_{LP}\right] \tag{4.19}$$

In (4.19), the winding AC inductance to winding DC resistance ratio comprises of two components. They are:

- Inductance ratio due to skin effect, F_{LS}.
- Inductance ratio due to proximity effect, F_{LP}.

These two components are expressed in (4.20) and (4.21) respectively as:

$$F_{LS} = \left[\frac{e^{2A} - e^{-2A} - 2Sin(2A)}{e^{2A} + e^{-2A} - 2Cos(2A)}\right] \tag{4.20}$$

$$F_{LP} = \left[\frac{e^{A} - e^{-A} + 2Sin(A)}{e^{A} + e^{-A} + 2Cos(A)}\right] \tag{4.21}$$

Substituting (4.20) and (4.21) into (4.19), we have (4.22);

$$F_{L} = \frac{A}{\omega}\left[\left[\frac{e^{2A} - e^{-2A} - 2Sin(2A)}{e^{2A} + e^{-2A} - 2Cos(2A)}\right] + 2\frac{N_l^2 - 1}{3}\left[\frac{e^{A} - e^{-A} + 2Sin(A)}{e^{A} + e^{-A} + 2Cos(A)}\right]\right] \tag{4.22}$$

Substituting (4.22) into (4.18), the leakage inductance of the laminated core inductor becomes (4.23).

$$L_{leak} = \frac{R_{w(dc)}A}{\omega}\left[\left[\frac{e^{2A} - e^{-2A} - 2Sin(2A)}{e^{2A} + e^{-2A} - 2Cos(2A)}\right] + 2\frac{N_l^2 - 1}{3}\left[\frac{e^{A} - e^{-A} + 2Sin(A)}{e^{A} + e^{-A} + 2Cos(A)}\right]\right] \tag{4.23}$$

where,

$\omega = 2\pi f$, is the angular frequency

f, is the frequency in Hertz.

From the plot in Fig. 4.5, at $A > 3$, the inductance ratio due to skin and proximity effect reduces approximately 1, i.e., $F_{LS} \approx 1$ and $F_{LP} \approx 1$. Hence, the winding ac resistance in (4.10) can be expressed as (4.24) and (4.25), respectively:

$$R_w = F_R\, R_{w(dc)} \approx R_{w(dc)}A\left[1 + 2\frac{N_l^2 - 1}{3}.1\right] \approx R_{w(dc)}A\left[2\frac{N_l^2 - 1}{3}\right] \tag{4.24}$$

$$R_w \approx R_{w(dc)}\left(\frac{\pi}{4}\right)^{3/4}\frac{d}{\delta_w}\sqrt{\eta}\left[2\frac{N_l^2 - 1}{3}\right] \tag{4.25}$$

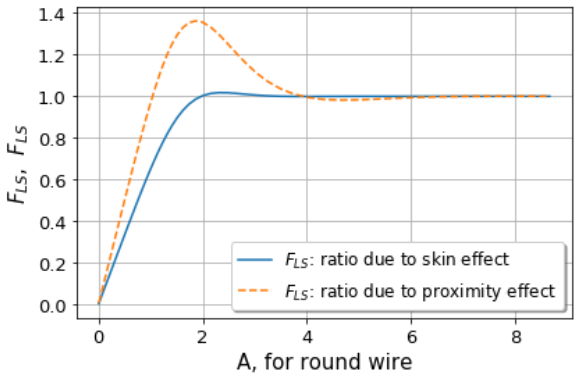

Fig. 4.5: F_{LS} and F_{LP} as a function of A

4.5.2 Magnetic Core Inductance

The magnetic core inductance, L_c related to the power loss due to magnetic field paths in an inductor core, was derived in [112] and is given as (4.26):

$$L_c = L_{m(dc)} \frac{\delta_c}{s} \frac{Sinh\left(\frac{s}{\delta_c}\right) + Sin\left(\frac{s}{\delta_c}\right)}{Cosh\left(\frac{s}{\delta_c}\right) + Cos\left(\frac{s}{\delta_c}\right)} \tag{4.26}$$

The plot of winding series inductance, core inductance, and winding leakage inductance as a function of frequency is shown in Fig. 4.6. It is observed that the inductance of the laminated core inductor decreases at higher frequencies, mainly due to skin and proximity effects which reduces the magnetic field inside the core.

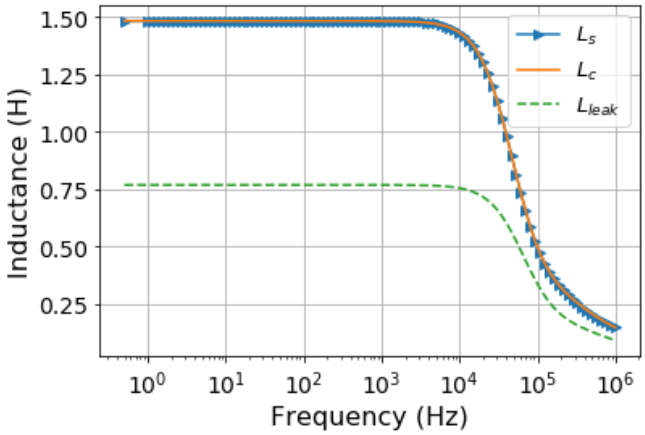

Fig. 4.6: Core inductance, winding series, and leakage inductance as a function of frequency

4.6 Winding Parasitic Capacitance

The parasitic capacitance represents the stored electric energy within the inductor which is divided into core and space electric energy. The inductor's electric energy is dominated by the

electric energy stored in the space [119]. Space electric energy is caused by the turns of insulated wire or conductor layered on top of each other and around the core, where they act as conductive plates. The insulated conductors of turns form turn-to-turn capacitances, C_{tt} where an electric field exists between the turns with different potentials and stores energy, as represented in Fig. 4.7.

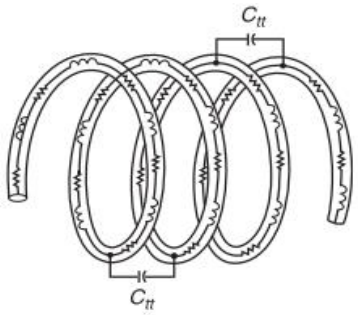

Fig. 4.7: Turn-to-turn capacitance of an inductor.

At high frequencies, the displacement current flows through the capacitors and bypasses the inductive reactance and resistive conductors. Hence, current leaks through the self-capacitance of an inductor at high frequencies. The total capacitance of inductors consists of the following components [120]:

- The turn-to-turn capacitances between turns of the same layer.
- The turn-to-turn capacitances between turns of adjacent layers.
- The turn-to-core and turn-to-shield capacitances.

Magnetic cores are made up of conducting materials, therefore, the turn-to-core capacitance depends on the core resistivity, ρ_c and the insulating material's relative permeability. Each turn's combined effect can be represented as a single capacitance known as the parasitic capacitance, which significantly affects an inductor's behaviour [121].

In [120]-[122], the inductor's parasitic capacitance was modelled and derived by considering the above components of the inductor. The turn-to-turn capacitance of multiple layer inductor with hexagonal winding pattern in [121] will be adopted and is expressed as (4.27):

$$C_{tt} = \frac{2\pi\epsilon_r\epsilon_o D_T}{\sqrt{\left(2\epsilon_r + ln\frac{d_o}{d_i}\right) ln\frac{d_o}{d_i}}} \times arctan\left[\frac{\sqrt{3}-1}{\sqrt{3}+1}\sqrt{\frac{2\epsilon_r + ln\frac{d_o}{d_i}}{ln\frac{d_o}{d_i}}}\right] \tag{4.27}$$

where,

D_T, is the diameter of the turn (m)

d_i, is the bare wire diameter (mm)

d_o, is the outer conductor diameter (mm)

ϵ_r, is the relative permittivity of the insulating coating.

The parasitic capacitance, C_p for a three-layer inductor with the conductive core is expressed in [120] as (4.28):

$$C_p = 0.5733 C_{tt}, for\ N \geq 10 \tag{4.28}$$

4.7 Equivalent Inductor Impedance

As shown in Fig. 4.1(b), the lumped parameter inductor model is represented by its equivalent series components, consisting of the total equivalent resistance, R_{eq} and the total equivalent reactance, X_{eq}. An inductor's impedance is simply the effective resistance to current flow, including the ac and dc components. Both components can be expressed as (4.29) and (4.30) respectively:

$$R_{eq} = \frac{R_s}{(1 - \omega^2 L_s C_p)^2 + (\omega R_s C_p)^2} \tag{4.29}$$

$$X_{eq} = \frac{\omega L_s \left(1 - \omega^2 L_s C_p - \left(\frac{{R_s}^2 C_p}{L_s}\right)\right)}{(1 - \omega^2 L_s C_p)^2 + (\omega R_s C_p)^2} \tag{4.30}$$

Therefore, the impedance of the equivalent circuit of Fig. 4.1(c) is given as (4.31):

$$Z = R_{eq} + jX_{eq} \tag{4.31}$$

Substituting (4.29) and (4.30) in (4.31), we have (4.32):

$$Z = \frac{R_s + j\omega L_s \left(1 - \omega^2 L_s C_p - \left(\frac{{R_s}^2 C_p}{L_s}\right)\right)}{(1 - \omega^2 L_s C_p)^2 + (\omega R_s C_p)^2} \tag{4.32}$$

The impedance magnitude of the laminated core inductor model is represented in (4.33) as:

$$|Z| = \sqrt{{R_{eq}}^2 + {X_{eq}}^2} \tag{4.33}$$

Moreover, the phase angle can be expressed in (4.34) as:

$$\varphi = arctan\left(\frac{X_{eq}}{R_{eq}}\right) \tag{4.34}$$

The extracted results from (4.2) - (4.28) were used with the circuit model to produce the results shown in Fig. 4.8 and Fig. 4.9. These show the equivalent resistance, equivalent reactance, impedance, and phase angle of laminated core inductor as a function of frequency. The results suggest that at a frequency where the phase angle equals zero, reactance is also zero because the inductive and capacitance reactance of the winding are equal; hence, the impedance magnitude is maximum at this frequency called resonant frequency. At frequencies beyond the resonant frequency, the impedance response becomes capacitive.

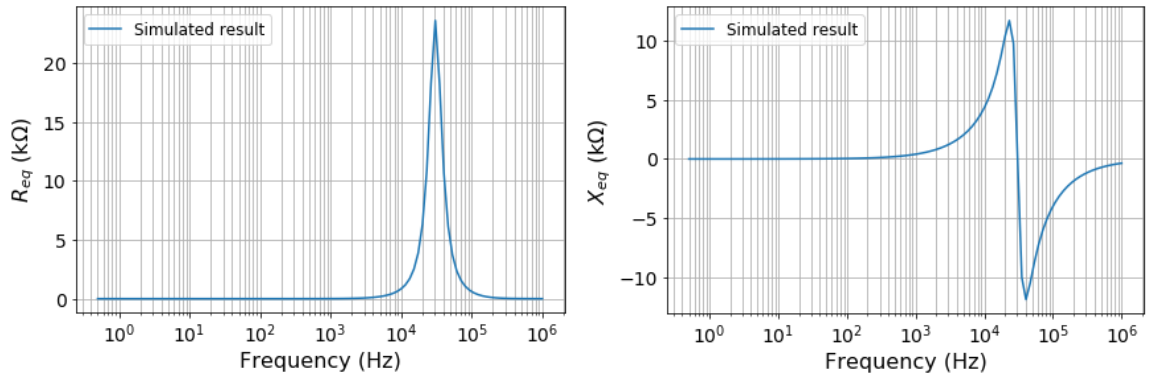

Fig. 4.8: Equivalent resistance and leakage reactance of laminated core inductor

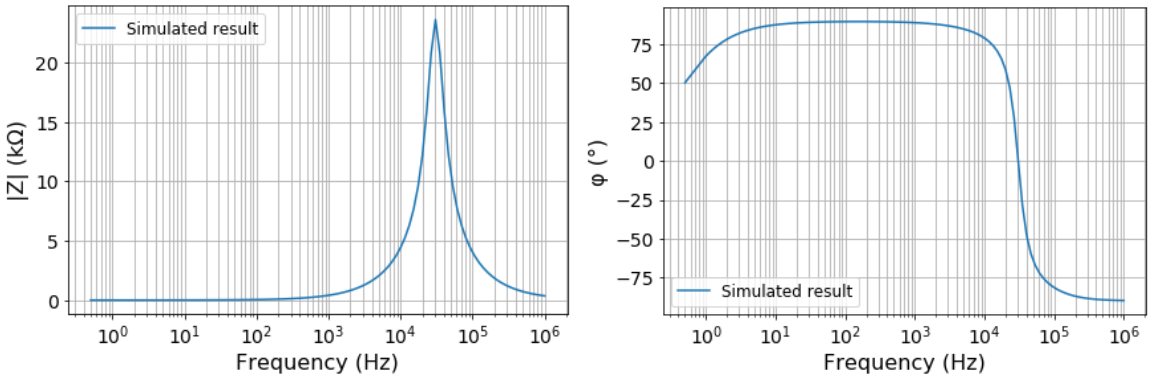

Fig. 4.9: Impedance magnitude and phase angle of laminated core inductor

For frequencies much lower than the first self-resonance frequency, the equivalent series reactance, X_{eq} has an inductive character and can be expressed as (4.35):

$$X_{eq} = \omega L_{eq} \tag{4.35}$$

Therefore, the inductor equivalent inductance (L_{eq}) at different frequencies can be determined as in (4.36):

$$L_{eq} = \frac{|X_{eq}|}{\omega} = \frac{|X_{eq}|}{2\pi f} \tag{4.36}$$

The inductor quality factor at a given frequency is given as (4.37):

$$Q = \frac{|X_{eq}|}{R_{eq}} = \frac{\omega L_s \left(1 - \omega^2 L_s C_p - \left(\frac{{R_s}^2 C_p}{L_s}\right)\right)}{R_s} \tag{4.37}$$

A self-resonant frequency, f_{res} of an inductor is defined as a frequency at which the winding inductance is equal to the winding capacitance. This condition makes the winding reactance zero. Hence, the capacitance at this condition could be determined by (4.38):

$$C_{f_{res}} = \frac{1}{(\omega f_{res})^2 L_{s(f_{res})} + \frac{R^2_{s(f_{res})}}{L_{s(f_{res})}}} \tag{4.38}$$

where,

f_{res}, is the resonant frequency

$L_{s(f_{res})}$, is the series inductance at the resonant frequency

$R_{s(f_{res})}$, is the series resistance at resonant frequency.

4.8 Conclusion

In this chapter, the use of an electrical equivalent circuit for modelling impedance data has been discussed. A silicon steel laminated core inductor has been examined, and analytical expressions have been presented to describe its lumped parameters' behaviour as a frequency function. Dowell's equation is adopted to determine the expression for the ratio of the winding AC to DC resistance and inductance in calculating the AC winding resistance and AC inductance values at high frequencies due to eddy current. The impedance expressions are presented using the equivalent circuit model. Finally, the simulated equivalent resistance and leakage reactance, impedance magnitude, and phase results of the laminated core inductor used for the case study are presented.

Chapter 5

Impedance Frequency Response Model and Parameter Extraction for SCIM Stator Winding

5.1 Introduction

An electromagnetic device's behaviour may be analysed using various techniques, including a numeric technique to solve the partial differential equations of the electromagnetic fields developed within the components using the finite element method (FEM), and an analytical technique. The analytical model of the device for electromagnetic analysis must represent the effects of electromagnetic fields and losses. Electromagnetic field effects are represented using a circuit approach whereby magnetic field effects are represented using inductors and the coupling between them. Capacitors represent electric field effects. Losses can be caused in windings, cores, or insulation of material and represented by resistors [123]. Hence, a rotating machine's quality and behaviour depend on parameters such as resistance, inductance, and capacitance. Among these parameters, the leakage inductance calculation constitutes an important stage in an electrical machine's design process. The RLC equivalent circuit representation of the stator winding would enable us to model the stator winding impedance behaviour under healthy and inter-turn fault conditions at different frequencies, which will be validated experimentally.

5.2 Induction Machine Stator Winding Model

This model aims to reduce the distributed parameters such as parasitic resistances, inductances, and capacitances inside the induction motor's stator winding for impedance response analysis. The experiments' findings explain the corresponding schematics of the lumped parameter model used in this research study.

5.2.1 Principle of Internal Models for Rotating Machines

When investigating high-frequency steady-state phenomena, all the conductors such as a transmission line, a machine winding, and a measuring wire show a distributed-parameter nature. A well-known lumped-parameter circuit approximates a distributed-parameter circuit.

The stator winding of a motor consists of a chain of series-connected coils that are distributed around the stator. Also, the reluctance of the flux paths changes as the flux penetrates the core. Due to the limited extent of flux penetration into the core, the flux linkage from one coil to a coil in a neighbouring slot is minimal, so the mutual coupling between coils is minimal.

The basic unit in the equivalent circuit for the winding is a coil. A stator coil occupies two distinct regions in the machine: the slot region in which the active coil sides are placed inside the slots in the magnetic core structure and the overhang region in which the end turns are positioned in the air. A scheme of a wound coil and its subdivision is shown in Fig. 5.1.

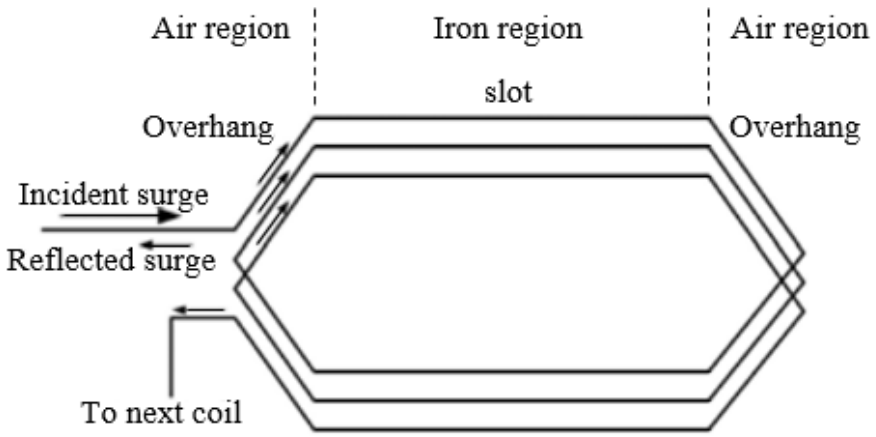

Fig. 5.1: Scheme of a form wound coil and its subdivision.

The following assumptions can be made when deriving the equivalent circuit of a machine winding [124]:

- The core iron's behaviour is like that of a ground sheath, and the slot iron boundary may be replaced by a grounded sheath, which is impenetrable to high-frequency waves.
- The series resistance and inductance of the coils are also frequency dependent due to the skin effect in the conductor and the eddy currents in the core.
- The two opposite overhang parts of the stator core are considered uncoupled because eddy-currents in the core provide effective shielding at high frequencies. Overhang and slot parts are also uncoupled because of the eddy currents in the core. The coil's two parts at the coil entry are uncoupled since they are nearly perpendicular to each other over most of their length and are further shielded from each other by eddy currents in adjacent coils. Insulation between the lamination permits magnetic coupling to the coils inside adjacent slots.

- The capacitive couplings between coils of one phase winding and between coils of different phase windings are very small and usually neglected. The capacitance between turns in a coil and between the coil and the core are important and should be considered.

Fig. 5.2 shows a cross-section of an induction motor winding. The induction motor's complete model consists of the winding phases' models, which can be either delta or star connected. Small induction motors, which have many turns or coils in the same stator slot, have high capacitances between turns and coils as well as high mutual inductances. Larger induction motors, which have fewer and longer turns per slot, have smaller capacitances between turns and smaller mutual inductances.

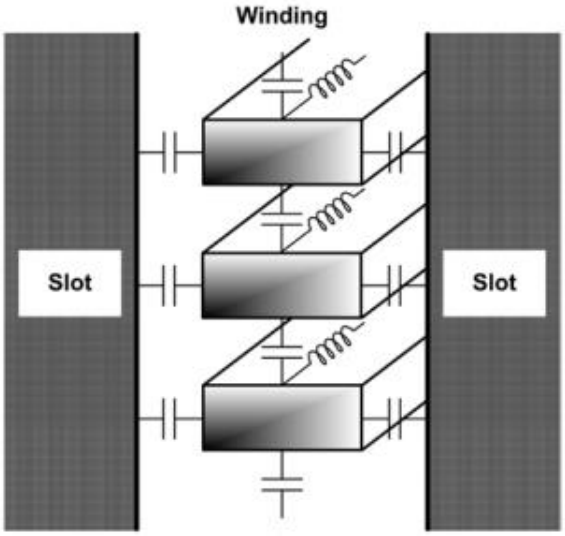

Fig. 5.2: Cross-section of machine winding

A distributed parameter winding model, as shown in Fig. 5.3 may be very time-consuming, and for many practical cases, the detailed representation of every winding turn is not required [124]. A much simpler network can be obtained by successive lumping of elements, and where there is geometric uniformity within a portion of a winding, accuracy does not suffer significantly because of this process. In Fig. 5.3, *R* and *L* are the series resistance and effective inductance respectively, while *M* is the mutual inductance between turns; C_1 and G_1 are turn-to-turn capacitance and conductance for all adjacent turns, whereas, C_2 and G_2 are turn-to-ground capacitance and conductance for all turns except the first and the last in the coil, for which additional capacitance and conductance, C_3 and G_3 are added to account for end conditions at both coil sides.

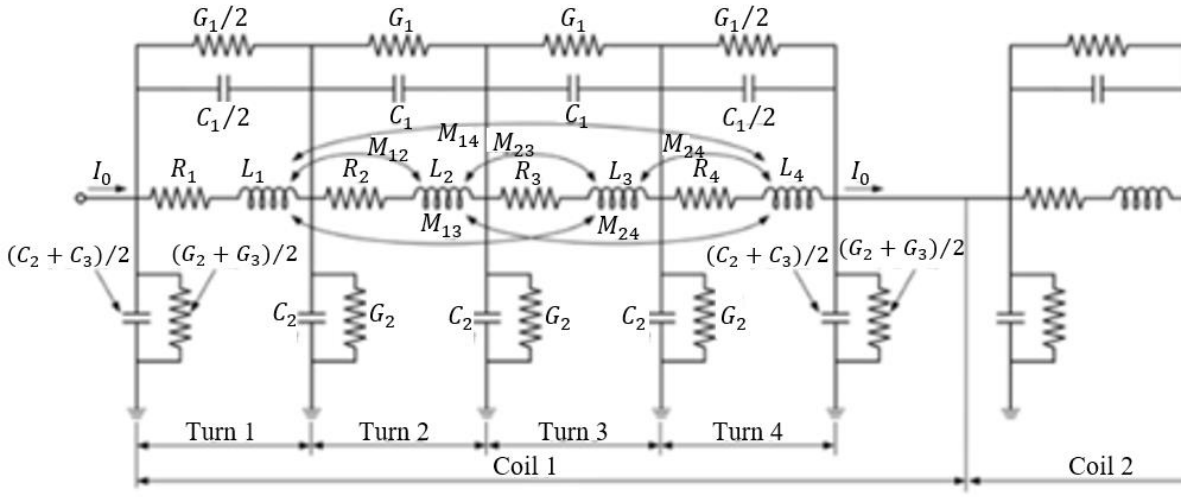

Fig. 5.3: Distributed-parameter circuit of rotating machine winding [125]

The distributed parameters in Fig. 5.3 are reduced to a simple model to determine the impedance behaviour of induction motor from low to high frequencies. The proposed circuit is shown in Fig. 5.4 where, R_s is the series resistance of the stator winding depends on the operating frequency; L_s is the series inductance which comprises the main inductance and leakage inductance, and C_p is the total winding capacitance of the stator winding.

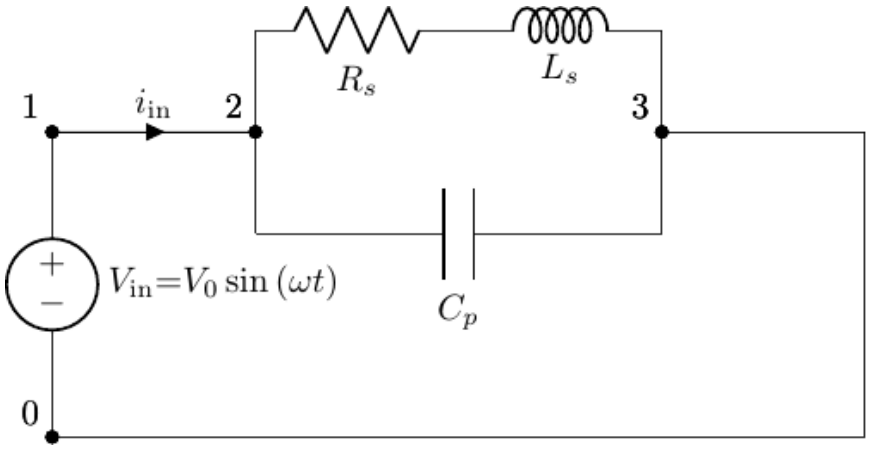

Fig. 5.4: Equivalent circuit for impedance analysis of stator winding

5.2.2 Analytical calculation of circuit parameters for impedance extraction

The procedure for calculating the stator phase winding parameters for the proposed model, is explained in this subsection. The analytical simulation was carried out using the geometrical stator winding parameters of a three-phase, 7.5 kW, silicon steel laminated stator core squirrel-cage induction motor (SCIM) in the lab, which is identified as SCIM2 in this dissertation. It is configured to simulate different percentages of inter-turn short-circuit faults (0%, 2%, 4%, 6% and 8%). The impedance frequency response of the SCIM2 stator winding at different winding

conditions is simulated, using the proposed equivalent circuit model considered in this study; its parameters presented in Table 5.1 were utilized.

Table 5.1: Table of SCIM2 stator winding and core parameters

Symbol	Value	Unit
l_{stack}	120.9	mm
N	240	-
b_c	4.4	mm
h_c	25.4	mm
D_o	0.686	mm
D_c	0.644	mm
b_1	3.34	mm
h_1	0.55	mm
b_4	5.5	mm
h_4	25.4	mm
ε_r	3.5	-
p	2	-
Q	48	-
m	3	-

5.2.2.1 Calculation of Resistance

The series resistance of the stator winding impedance model can be determined by first calculating the conductors' DC resistance in the stator slot. This resistance depends on the average length l_{ave} of the slot winding coil turn, the cross-sectional area of the conductor, $A_c = b_c h_c$ in the slot, and the conductor material's conductivity σ_c [126].

$$R_{dc} = \frac{N l_{ave}}{\sigma_c A_c} \tag{5.1}$$

where,

b_c, is the conductor width in the slot

h_c, is the conductor height in the slot.

The specific conductivity of pure copper at room temperature (+20℃) is, $\sigma_c = 58 \times 10^6 S/m$ and the conductivity of commercial copper wire is, $\sigma_c = 57 \times 10^6 S/m$. The average length,

l_{av} of a slot winding coil turn with enamelled wires for a low and high voltage machine are approximately (5.2) and (5.3) respectively [126].

$$l_{av} \approx 2l_{stack} + 2.4W + 0.1\,m \tag{5.2}$$

$$l_{av} \approx 2l_{stack} + 2.8W + 0.1\,m \tag{5.3}$$

where,

l_{stack}, is the length of the stator stack of the motor in *metres*

W, is the average coil span in *metres.*

The skin effect occurs in the slot area and to a lesser extent in the end windings. To determine the resistance of a rotating machine's stator winding, the influence of skin effect due to eddy current is considered. Eddy currents are produced by flux crossing the slot transversely from tooth to tooth through the body of the conductor and tend to flow on the surface of the conductor through the length of the stator core and return along the edge nearer the slot-root. The eddy currents will produce magnetic flux, which will react to the whole system of currents, and the net result in the conductor will be a current varying in density and phase at different depths [127]. This effect can be estimated by the ratio of the AC resistance and DC resistance of the conductor, referred to as resistance coefficient or resistance factor, K_R.

Considering the numerous parallel conductors in the slot, connected in series having the same current flowing through them, the average relative increase of the conductor's resistance with alternating current over the slot is given by [126]:

$$K_R = \frac{R_s}{R_{dc}} = \varphi(\xi) + \frac{N_n^2 - 1}{3}\psi(\xi) \tag{5.4}$$

$$\varphi(\xi) = \xi\frac{sinh(2\xi) + sin(2\xi)}{cosh(2\xi) - cos(2\xi)} \tag{5.5}$$

$$\psi(\xi) = 2\xi\frac{sinh(\xi) - sin(\xi)}{cosh(\xi) + cos(\xi)} \tag{5.6}$$

Considering the stator slot with multiple conductors as shown in Fig. 5.5, the parameter, ξ is a dimensionless quantity called reduced conductor height, which can be determined using the dimension of the conductors in the slot by (5.7) and graphically represented in Fig. 5.6:

$$\xi = \alpha h = h\sqrt{\frac{1}{2}\omega\mu_0\sigma\frac{nb}{b_s}} = h\sqrt{\pi\mu_0\frac{nb}{b_s}\frac{f}{\rho}} \tag{5.7}$$

where,

h, is the conductor's height in *metres* (or the number of parallel strands on top of each other; $N_n \times$ strand height)

α, the inverse of it is called the depth of penetration with unit m^{-1}

ρ, is the conductor's resistivity (for copper at operating temperature $\rho = 0.02 \times 10^{-6}\Omega m$)

μ_0, is the vacuum magnetic permeability ($\mu_0 = 4\pi 10^{-7} H/m$)

n, is the number of conductors in each layer

b_s, is the slot's width in *metres,* and b is the conductor's width in *metres.*

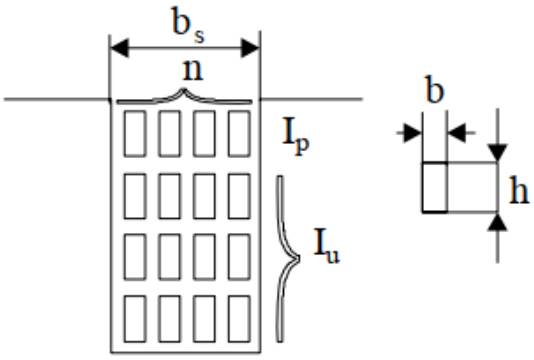

Fig. 5.5: Determination of the reduced conductor height with multiple conductors [128]

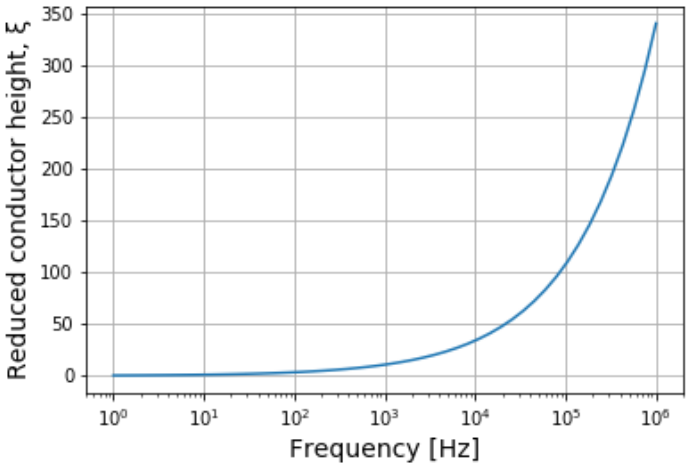

Fig. 5.6: Reduced conductor height as a function of frequency

The resistance factor value in (5.4) is only valid for rectangular conductors. The eddy current losses of round conductors are 0.59 times the losses of rectangular wires [129]. Hence, the

resistance factor for round conductors, K_{Rr} is approximately (5.8) and is represented graphically in Fig. 5.7:

$$K_{Rr} = 1 + 0.59\frac{N_n^2 - 0.2}{9}\xi^4 \tag{5.8}$$

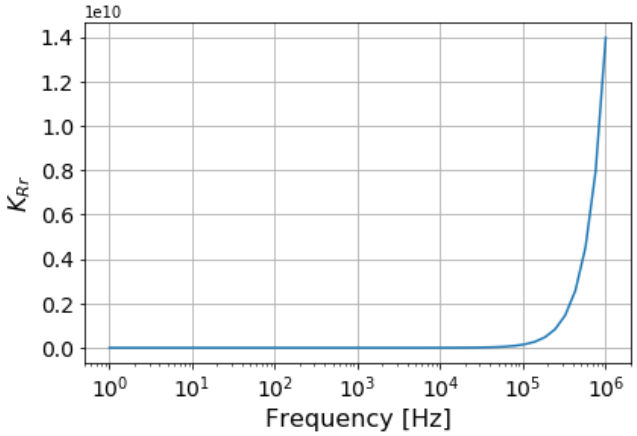

Fig. 5.7: Resistance factor as a function of frequency

The skin effect is observed, not only in the slot but, also in the couplings between them. Since the conductors in the overhang region are relatively far from those in the slot region, their influence is small and can be neglected. Therefore, we assume that the slot region's skin effect is the same as in the overhang region. Hence, the average increase of the conductors' resistance for one phase of the winding is smaller than the resistance factor calculated for the conductors' active part. The main average increase of the resistance, K_R' of the stator conductor is determined by [130]:

$$K_R' = \frac{K_{Rr} + \lambda}{1 + \lambda} \tag{5.9}$$

Therefore, the total series resistance, R_s of the equivalent circuit can be calculated as (5.10):

$$R_s = R_{Dc}K_R' \tag{5.10}$$

where,

$\lambda = \frac{l_s}{l_i}$, is the ratio of the winding's end length and the slot's length

K_{Rr}, is the increase of the resistance for all conductors in the slot.

5.2.2.2 Calculation of Inductance

In rotating electrical machines, the total flux consists of the main flux, $\emptyset_m$ and leakage flux, $\emptyset_\sigma$ components. The main flux (air gap flux) of the machines enables electromechanical energy

conversion, but a fraction of the total flux called the leakage flux does not participate in the energy conversion. The main flux crosses the air gap of the rotating machine, creates an air gap flux linkage in the winding, and consequently links both the stator and rotor windings. Flux leakage occurs in both stator and rotor winding and does not generally cross the air gap. They contribute to the total flux linkage of the winding by producing a leakage flux linkage ψ_σ. The corresponding leakage flux linkages are the stator flux leakage $\psi_{s\sigma}$ and the rotor flux leakage $\psi_{r\sigma}$ [126].

The air gap or main or magnetizing flux linkage, ψ_m corresponds to the magnetizing or main inductance, L_m, and the leakage flux linkage, ψ_σ corresponds to a leakage inductance, L_σ. The stator inductance of an induction machine is the sum of the magnetizing inductance, L_m and the stator leakage inductance, $L_{s\sigma}$ [126], which relate their respective flux linkage components to the current flowing through the stator windings.

$$L_s = L_m + L_{s\sigma} \tag{5.11}$$

The procedures on how to determine the values of these two components will be explained in detail.

Magnetizing inductance

The magnetizing inductance refers to the magnetizing current's magnetic field that crosses the air gap and links both the stator and the rotor windings. The magnetizing current is much smaller than the rated current in most induction motors. Magnetizing current corresponds to the transformer's no-load current, which is the current that circulates in the primary winding when the secondary winding does not have any current. When an induction motor is not coupled to a mechanical load, the rotor rotates with no external resistance, and the load torque is equal to zero. The magnetizing inductance, L_m of a single-phase winding in [126] will be adopted and is represented as (5.12);

$$L_m = \frac{2}{\pi}\frac{1}{2p}\frac{4}{\pi}\frac{\tau_p}{\delta_{ef}}\mu_o l'(k_{w1}N_s)^2 = \frac{4\tau_p}{\pi^2 p\delta_{ef}}\mu_o l'(k_{w1}N_s)^2 \tag{5.12}$$

where,

τ_p, is the pole pitch

N_s, is the number of stator turns in series

D_δ, is stator bore diameter

$k_{w1}N_s$, is the effective turns of the winding

l', is the length of the machine

p, is the number of pole pairs

δ_{ef}, is the effective air gap met by the current linkage of the stator winding

k_{w1}, is the winding factor.

The pole pitch, τ_p is the peripheral distance between identical points on two adjacent poles, which is always equal to 180^0 regardless of the number of poles in the motor and can be calculated by (5.13):

$$\tau_p = \frac{\pi D_{is}}{2p} \tag{5.13}$$

The winding factor, K_{w1} depends on winding distribution factor, k_{q1}, chording factor or pitch factor, k_{c1}, and skewing factor, k_{s1} and can be represented as:

$$k_{w1} = k_{q1}k_{c1}k_{s1} \tag{5.14}$$

$$k_{q1} = \frac{sin\ (\pi/6)}{q\ sin\ (\pi/6q)} \leq 1 \tag{5.15}$$

$$k_{c1} = sin\frac{\pi}{2}\frac{c}{\tau_u} \leq 1 \tag{5.16}$$

$$k_{s1} = \frac{sin(s\pi/2\tau_u)}{s\pi/2\tau_u} \tag{5.17}$$

$k_{s1} = 1$ when the stator slots are straight.

where,

s, is the skew length

c/τ_u, is the chorded coil span taking as $5/6$

$\tau_u = Q/2p$, is the pole pitch span in slot pitches

$Q = 2pmq$, is the number of slots, m is the number of the phase winding

D_{is}, is the stator core diameter, and p is the number of pole pairs.

The effective air gap can be determined using Carter's principle, which observed that the air gap seems to be longer than its physical measure; hence, the air gap length increases with the

Carter factor, k_{Cs} [126]. The Carter factor can be determined based on the dimension in Fig. 5.8. It shows the air gap flux density behaviour along a slot pitch revolving at an angle α around the periphery of the motor.

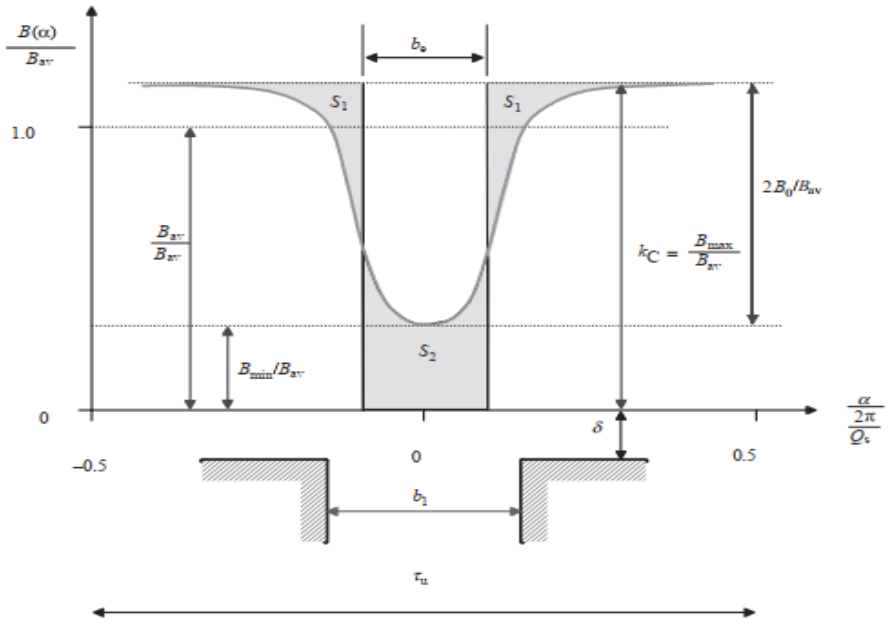

Fig. 5.8: The behaviour of the air gap flux density$B_\delta(\alpha)$ along a slot pitch, τ_u [126]

The shaded area S_1 and S_1 are equal to S_2. The equivalent slot opening b_e, in which the slot density is zero, is (5.18):

$$b_e = kb_1 \tag{5.18}$$

where,

b_1, is the slot opening width

k, can be approximately calculated as (5.19):

$$k \approx \frac{b_1/\delta}{5 + b_1/\delta} \tag{5.19}$$

δ, is the air gap. The carter factor can now be determined using (5.20):

$$K_{Cs} = \frac{\tau_u}{\tau_u - b_e} = \frac{\tau_u}{\tau_u - kb_1} \tag{5.20}$$

Therefore, the equivalent or effective air gap in the stator of the induction motor is approximately (5.21):

$$\delta_{ef} \approx K_{Cs}\delta \tag{5.21}$$

The motor's flux density remains constant over a core distance and decreases gradually to zero along the motor's shaft because of the edge field. This edge field is included in the main flux, thereby contributing to torque production. Hence, the equivalent core length is approximated as (5.22):

$$l' \approx l + 2\delta \tag{5.22}$$

where,

l, is the actual stator core length

δ , is the air gap.

Stator Leakage Inductance

The stator and rotor's leakage flux generates the winding's total flux linkage by producing a leakage flux linkage, ψ_σ component [126]. The corresponding leakage flux linkages are the flux leakage, $\psi_{s\sigma}$ of the stator and the rotor's flux leakage, $\psi_{r\sigma}$. Flux leakage may cause some extra losses in the frame of the motor. The slot leakage flux increases the conductors' skin effect in the slots, causing more copper losses in the stator. The spatial distribution of the windings causes an air gap (or harmonic) flux leakage. Hence, leakage flux comprises of:

- All the flux components that do not cross the air gap; and
- All flux components crossing the air gap that do not participate in the formation of the primary flux linkage.

Fluxes crossing the air gap are included in the air gap flux, and air gap fluxes do not completely link the motor's windings to each other. Due to short pitching, skewing, and the winding's spatial distribution (which causes air gap or harmonic flux leakage), the link between the stator and rotor windings is weakened and not regarded as leakage with pitch winding factor k_p and the skewing factor, k_{sq}.

The flux components that do not cross the air gap belong to the leakage flux. They are slot leakage flux (u), tooth-tip leakage flux (d), end winding leakage flux (w), and pole leakage flux (p), as shown in Fig. 5.9.

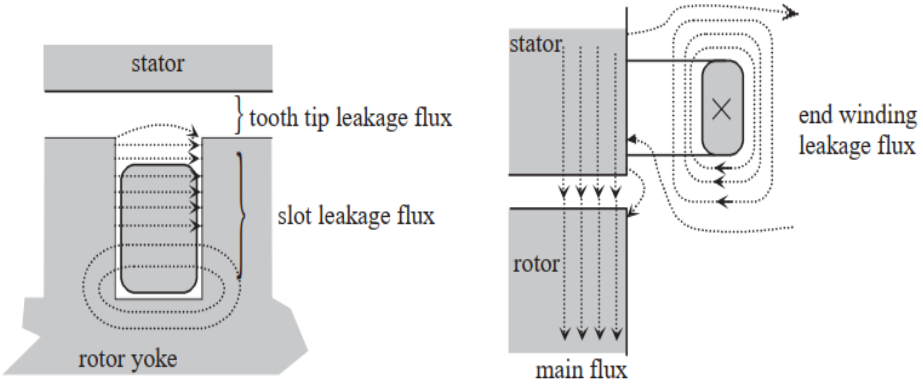

Fig. 5.9: Slots and end winding leakage flux of a coil winding [126].

Hence, the stator leakage inductance, $L_{s\sigma}$ is divided into the following partial leakage inductances: air gap leakage inductance, L_{δ}, slot leakage inductance, L_{u}, tooth-tip leakage inductance, L_{d}, end winding leakage inductance, L_{w}, skew leakage inductance, L_{sq} and can be calculated as the sum of these leakage inductances (5.23):

$$L_{s\sigma} = L_{\delta} + L_{u} + L_{d} + L_{w} + L_{sq} \tag{5.23}$$

The harmonic leakage inductance created in the air gap region is directly proportional to magnetizing inductance and the weight of magnetomotive force (MMF) harmonics. The amount of this inductance is more dominant in tooth-wound machines rather than integer slot configurations. This is also significant only in machines with a small air gap and is especially the case with asynchronous (induction) machines. In asynchronous machines with a caged rotor, the cage damps harmonics, and the air gap inductance becomes less significant.

The tooth-tip leakage inductance is determined by the magnitude of leakage flux in the air gap outside the flux opening. A potential difference results between the teeth on opposite sides of the slot opening due to the slot's current flux linkage, and some of it is used to produce the leakage flux in the tooth-tip. The tooth-tip leakage inductance is reduced with reduced air gap height and widened slot opening. Since the tooth tip leakage inductance depends significantly on the air gap, its influence becomes insignificance in an asynchronous machine (induction machine) and can be neglected.

The stator and rotor of a rotating machine, especially in squirrel-cage induction motors, are often assembled in a skew position to reduce the influence of permeance harmonics caused by slots. When a winding is assembled and skewed with respect to each other, the magnetic

connection between them is weakened. The flux produced by the stator winding passes through the air gap but does not penetrate a skewed rotor. This leakage flux can be defined by the skew inductance, which depends on the leakage factor, σ_{sq} caused by skewing and is represented as (5.24):

$$L_{sq} = \sigma_{sq} L_m \tag{5.24}$$

This factor is always minimal, and therefore, the skew leakage inductance can be neglected.

Slot leakage occurs due to flux which crosses a conductor circumferentially from tooth to tooth, closing its path around the iron beneath the slot and never crossing the air gap, and this corresponds to the leakage inductance. The slot leakage inductance without skin effect can be calculated by (5.25):

$$L_u = \frac{4m}{Q} \mu_o l' N^2 \lambda_u \tag{5.25}$$

where,

m, is the number of the phase winding

Q, is the number of slots in the stator

l', is the slot length

N, is the number of series-connected turns in a phase winding

$\lambda_u = \lambda_1 + \lambda_4$, is the permeance factor of the slot

$\lambda_4 = h_4/3b_4$, is the permeance factor of the wound part of the slot

$\lambda_1 = h_1/b_1$, is the permeance factor of the slot opening

h_4, is the slot conductor height and b_4 is the slot width

h_1, is the slot tooth height and b_1, is the slot opening distance.

The leakage flux in the conductor area crowds towards the slot opening, leading to a reduced leakage flux linkage, thus reducing slot leakage inductance**.** This occurs due to the skin effect, which tends to resist the conductor's flux penetration [126]. The slot leakage inductance accounting for the skin effect can be calculated by first determining the slot leakage inductance factor, K_l. This is the ratio of the AC leakage inductance to DC leakage inductance and is represented as:

$$K_l = \frac{L_{ac}}{L_{dc}} = \frac{1}{N_n^2}\varphi'(\xi) + \frac{N_n^2 - 1}{N_n^2}\psi'(\xi) \tag{5.26}$$

$$\varphi'(\xi) = \frac{3}{2\xi}\frac{sinh(2\xi) - sin(2\xi)}{cosh(2\xi) - cos(2\xi)} \tag{5.27}$$

$$\psi'(\xi) = \frac{1}{\xi}\frac{sinh(\xi) + sin(\xi)}{cosh(\xi) + cos(\xi)} \tag{5.28}$$

$$\xi = \alpha h_c = h_c\sqrt{\frac{1}{2}\omega\mu_0\sigma\frac{nb}{b_s}} = h_s\sqrt{\pi\mu_0\frac{nb}{b_s}\frac{f}{\rho}} \tag{5.29}$$

where,

L_{dc}, is the DC slot leakage inductance which is represented as [131]:

$$L_{dc} = \frac{\mu_0 n_s^2 l_{stack} h_s}{3b_s} \tag{5.30}$$

N_n, is the number of layers

n_s, is the number of conductors in the slot

l_{stack}, is the stack length in *meters*

h_s, is the slot height in *meters*

b_s, is the slot's width in *meters.*

The permeance factor of the slot under skin effect is $\lambda_u = \lambda_1 + k_l\lambda_4$ and represented in Fig. 5.10.

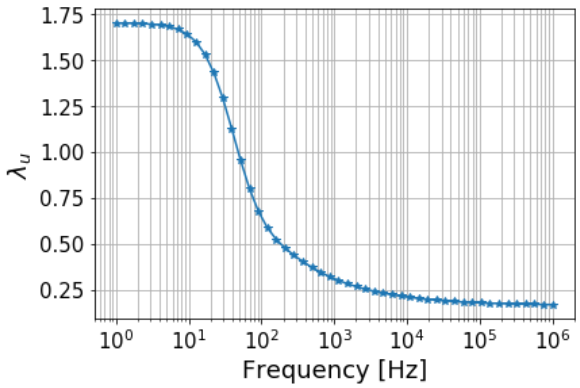

Fig. 5.10: Slot permeance factor under skin effect

Therefore, the slot leakage inductance considering the skin effect can be determined by (5.31) and represented in Fig. 5.11:

$$L_u = \frac{4m}{Q}\mu_o l' N^2(\lambda_1 + k_l\lambda_4) \tag{5.31}$$

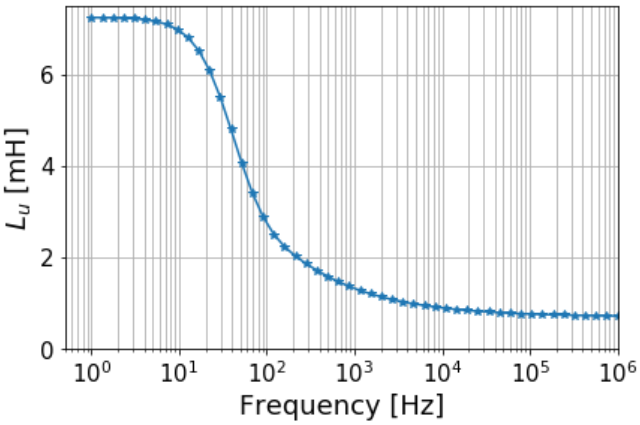

Fig. 5.11: Slot leakage inductance due to skin effect

The end winding produces a distinctly different leakage flux component whose magnetic circuit is almost entirely in the air. This flux results from all the currents flowing through the end windings because each coil side which forms the functional working portion of the coil must exit from the core body and be bent in a circumferential path in order to be directed back into a different slot for the return path [132]. The accurate determination of an end winding inductance is challenging due to the variable length of the flux path in both the motor's iron and air regions, which would require a three-dimensional numerical solution. Another reason is the flux part in the air region is longer than that in the iron region, and since the end winding is relatively far from the slot parts, as shown in Fig. 5.12, the end winding inductances are not very high [126].

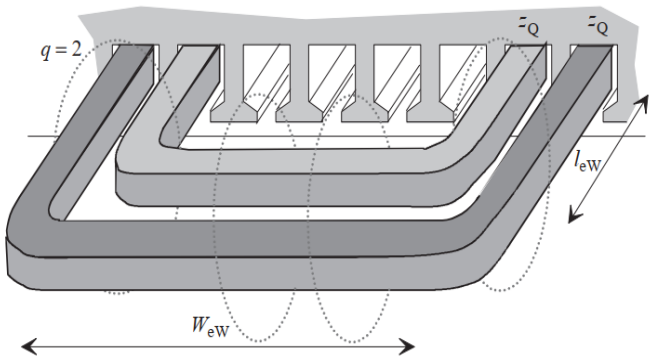

Fig. 5.12: Leakage flux and dimension of an end winding [129]

The end winding flux is due to the influence of all the coil turns belonging to a coil group. For practical purposes, the skin effect occurs only in that part of the conductor, which lies in the

slot part and is absent in the winding's end connections. Therefore, the equation for end winding leakage inductance can be written as:

$$L_w = \frac{4m}{Q} q {N_s}^2 \mu_0 l_w \lambda_w \tag{5.32}$$

The average length of the end winding and the product $l_w\lambda_w$ can be written in the form (5.33) and (5.34) respectively:

$$l_w = 2l_{ew} + W_{ew} \tag{5.33}$$

$$l_w\lambda_w = 2l_{ew}\lambda_{1ew} + W_{ew}\lambda_w \tag{5.34}$$

where,

l_w, is the axial length of the end winding measured from the end of the stack

$W_{ew} = \tau'_p - \tau'_u$, is the coil span (width of the end winding)

τ'_p and τ'_u, is the pole pitch and slot pitch at the average air gap diameter, which is the sum of the air gap diameter and the total length of the slot

λ_{1ew} and λ_w, are the corresponding permeance factors shown in Table 5.2 where the one highlighted in red colour is used in this model.

Table 5.2: End winding leakage permeance factors of SCIM for various stator and rotor combinations [133].

Type of stator winding	**Type of rotor winding**	λ_{1ew}	λ_w
3-phase, 3-plane	3-phase, 3-plane	0.40	0.30
3-phase, 3-plane	Cylindrical 3-phase diamond winding	0.34	0.34
3-phase, 3-plane	Cage winding	0.34	0.24
3-phase, 2-plane	3-phase, 2-plane	0.55	0.35
3-phase, 2-plane	Cylindrical 3-phase diamond winding	0.55	0.25
3-phase, 2-plane	Cage winding	0.50	0.20
Cylindrical 3-phase diamond winding	Cylindrical 3-phase diamond winding	0.26	0.36
Cylindrical 3-phase diamond winding	Cage winding	0.50	0.20
1-phase	Cage winding	0.23	0.13

The total leakage inductance, ($L_{s\sigma}$) and stator inductance, (L_s) considering the skin effect is simulated and represented in Fig. 5.13 and Fig. 5.14, respectively. It is apparent that both

inductances depend on the frequency and decrease at higher frequencies. The decrease in both inductances can be attributed mainly to eddy currents, which reduce the core magnetic field.

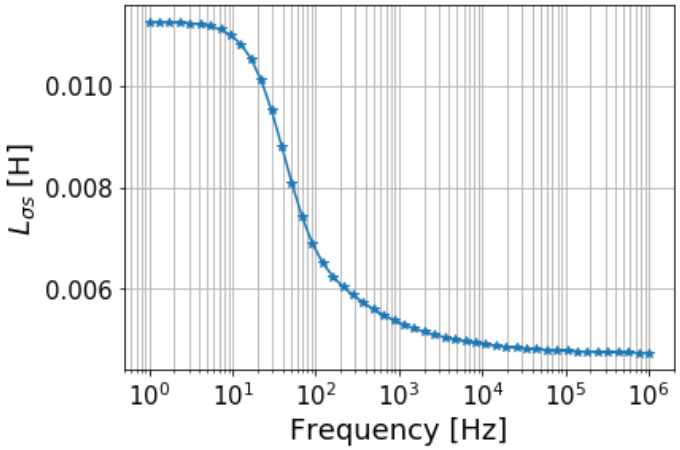

Fig. 5.13: Total leakage inductance under skin effect

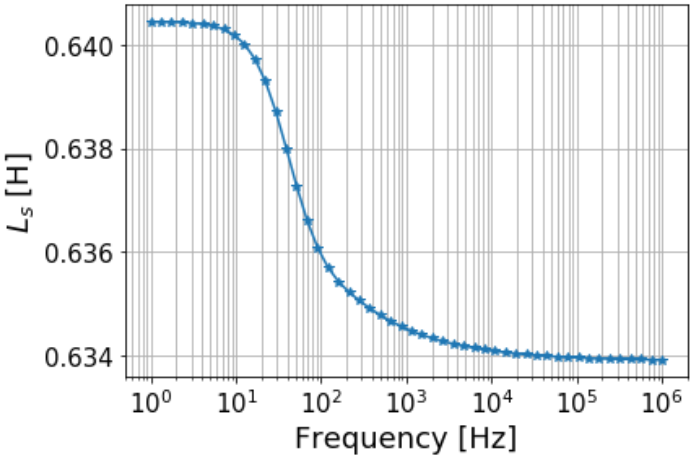

Fig. 5.14: Stator inductance under skin effect

5.2.2.3 Calculation of Capacitance

A charge is transferred to and stored in two conductors (equal magnitude on both conductors, but opposite polarity) if a DC voltage is applied across them, as shown in Fig. 5.15. This charge induces an electric field intensity, *E* between the two conductors directed from the conductor containing a positive charge to the one with a negative charge. Therefore, the structure's capacitance is the charge's ratio stored on the two conductors and the potential difference between them.

$$C = \frac{Q}{V} \tag{5.35}$$

The capacitance of a structure is its ability to store charge. Hence, the capacitance of a structure depends only on its dimensions, shape, and properties of the medium surrounding the conductors (e.g., free space, Teflon) [134].

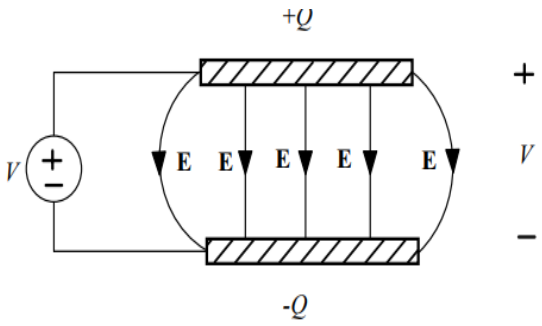

Fig. 5.15: Capacitance between two conductors

The basic types of parasitic capacitances present in an induction motor's stator windings are turn-to-turn and turn-to-core capacitance. The extension of these basic types is coil-to-coil, coil-to-ground, phase-to-phase, and phase-to-ground [135]. There are currently three methods in the literature for the calculation of capacitance between conductors of circular cross-section. The capacitance value is influenced by the insulation material and air space between the turns but differs in defining the path that the electric field lines form between the turns [136], [137].

A random wound stator of the induction motor consists of a multiturn coil. The hexagonal arrangement of conductors in a multiturn coil is represented in Fig. 5.16. This was studied in [122] by considering the two components of turn-to-turn capacitance to determine the total turn-to-turn and turn-to-core capacitance of a multiturn coil.

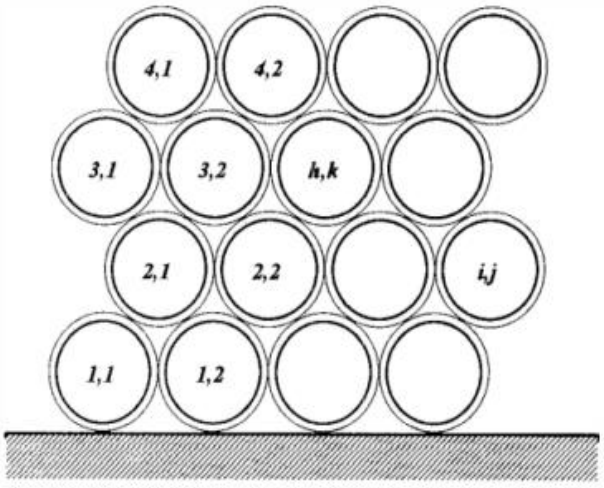

Fig. 5.16: Hexagonal arrangement of conductors in a multi-layer winding [122]

The following assumptions were made in determining the turn-to-turn capacitance of a multiturn coil and are adopted in calculating the parasitic capacitance for extracting the impedance of the stator winding of an induction motor:

- A turn can be divided into an elementary surface that faces an adjacent turn.
- The angle between two elementary cylindrical surfaces of adjacent turns covers $\pi/3$.
- The air gap path between two elementary cylindrical surfaces of adjacent turns is the length of a line of the electric field connecting the two opposite elementary cylindrical surfaces as given in Fig. 5.17.
- The insulation coating thickness, *s* is much lower than the conductor's outer diameter, including insulation, D_0.

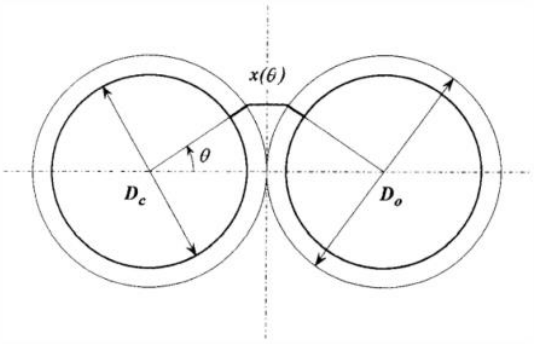

Fig. 5.17: The assumed path of an electric field line between two adjacent turns [122]

The total turn-to-turn capacitance of a multi-turn coil is represented by (5.36):

$$C_{tt} = \varepsilon_0 L \left[\frac{\varepsilon_r D_a \theta^*}{2t} + cot\left(\frac{\theta^*}{2}\right) - 3.732\right] \tag{5.36}$$

where, angle θ^* is expressed as:

$$\theta^* = cos^{-1}\left(1 - \frac{2t}{\varepsilon_r D_a}\right) \tag{5.37}$$

L, is the turn length same as the circumference of the conductor

$\varepsilon_0 = 8.86 \times 10^{-12}\, F/m$, is the permittivity of free space

$D_a = (D_0 + D_c)/2$, is the average diameter of the insulating coating shell

D_0, is the outer diameter of a conductor, including insulation

D_c, is the diameter of the conductor excluding insulation

t, is the thickness of the coating and ε_r is the relative permittivity of the material.

5.2.2.4 Simulated Stator Winding Impedance Response

The SCIM2 stator winding parameters presented in section 5.32, were used to simulate, and extract the proposed stator winding equivalent circuit parameters. The impedance of the circuit was calculated, and its magnitude was extracted and plotted at different frequencies. In this section, SCIM2 stator winding impedance response magnitude under healthy (baseline) and faulty conditions are simulated and compared to evaluate motor winding.

Simulated Baseline Results

The values obtained under this condition are plotted as a function of frequency and represented in Fig's 5.18 – 5.20. The effect of eddy currents on the series equivalent resistance of the stator winding could be observed in Fig. 5.18. This value increases as the operating frequency increases as expected because the conductor's AC resistance increases and becomes higher than the DC resistance due to the magnetic field induced by the alternating current in the conductor. At the resonant frequency where the inductive and capacitive reactance is equal but opposite, the equivalent resistance starts reducing as expected, which is due to the shunt capacitance in the equivalent circuit model.

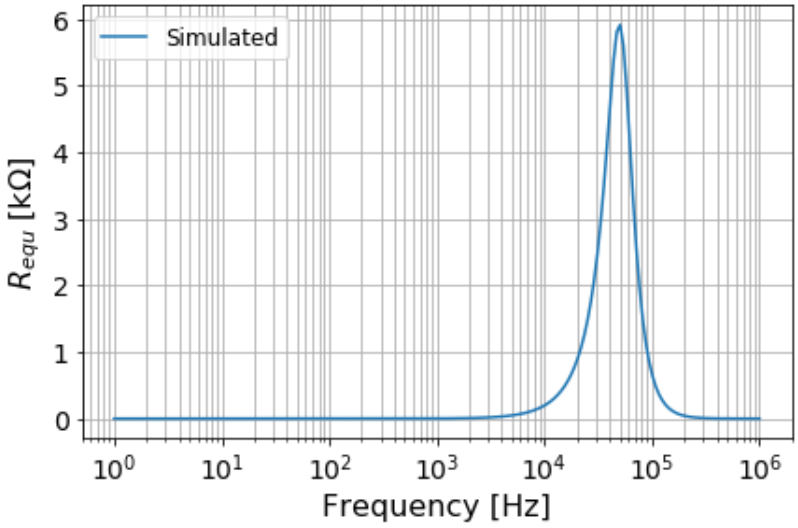

Fig. 5.18: Series equivalent resistance response of the stator winding

Fig. 5.19 reveals the series equivalent reactance's behaviour for the stator winding of a SCIM2. The effects due to the eddy currents in laminated stator core and turn-to-turn become significant at higher frequencies. At the frequency of about 30 kHz, the stator winding equivalent reactance starts reducing due to skin and proximity effect because of the non-uniform current density due to eddy current alters the internal magnetic flux linkage in a motor.

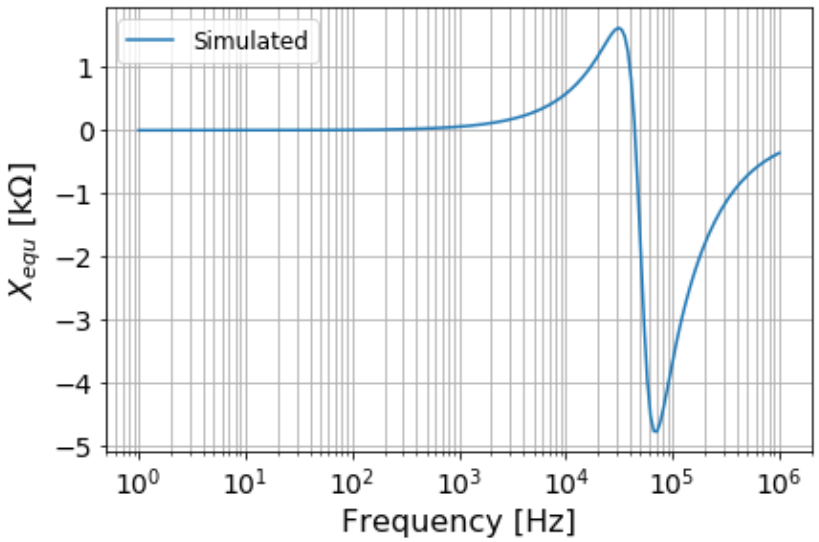

Fig. 5.19: Series equivalent reactance as a function of frequency

Fig. 5.20 shows the behaviour of the impedance response of the stator winding of an induction motor. Three essential impedance regions are observed from the plot: the resistive, inductive, and capacitive region. The impedance is close to zero at low frequencies (frequencies less than 1 kHz), which is more resistive. At frequencies between 1 kHz and about 45 kHz (which is the resonant frequency), the impedance starts increasing, representing the inductive region. The resonance is caused by the interaction of the stator windings' shunt capacitance with the magnetizing inductance. The capacitance becomes dominant at frequencies beyond the resonant frequency, affecting the impedance plot by reducing its magnitude.

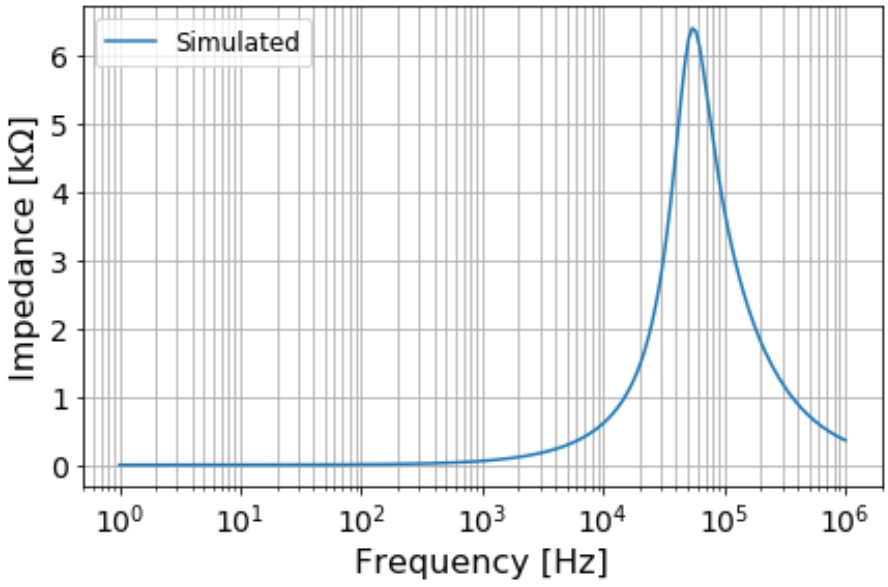

Fig. 5.20: Simulated impedance response of the SCIM2 stator winding

Simulated Inter-turn Fault Results

Faults such as inter-turn short-circuits fault must cause either the inductance or the capacitance of the winding's located part to change by a significant amount and, hence, the frequency response. Since the number of short-circuited turns reduces the conductor's length, the percentage number of severities is simulated by reducing the number of turns in the stator winding to emulate inter-turn fault. Therefore, about two, four, six, and eight percent of the total number of turns of SCIM2 stator phase winding will emulate different levels of severities of inter-turn short-circuit fault and could be validated experimentally. Fig. 5.21 shows the simulated SCIM2 impedance response for different stator winding conditions at different frequencies. It was observed that the impedance magnitude peak at different stator winding conditions reduces as the level of severities increases. Also, the resonant frequency at each emulated fault condition is relatively close to each other while deviating from the healthy one (causing the plot to shift to the right), as shown in Table 5.3. These values are plotted and presented in Fig. 5.22. Therefore, to assess the condition of squirrel-cage induction motors stator winding using impedance frequency response, the impedance peak magnitude and the frequency at a resonant point are selected as key indicators.

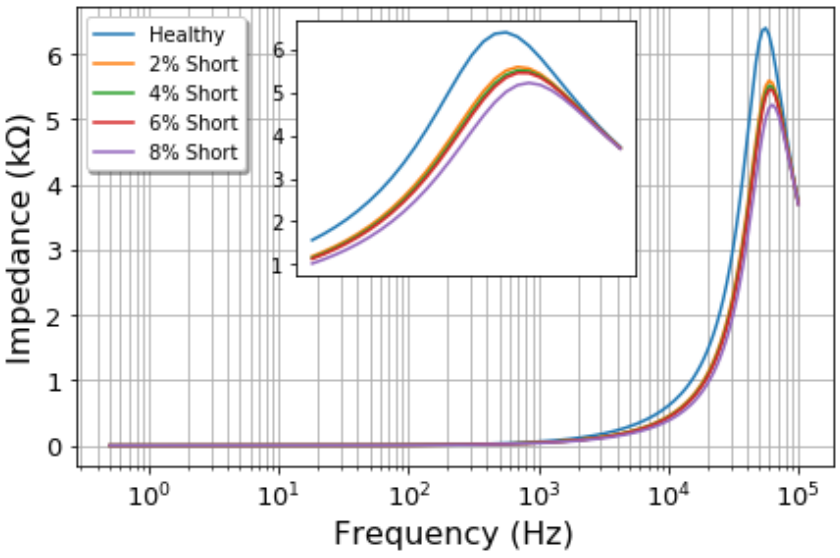

Fig. 5.21: Simulated SCIM2 impedance response for different stator winding conditions

The impedance magnitude peak and a resonant frequency of the simulated stator winding impedance response at different percentages of fault levels are shown in Table 5.3. It is observed that at different percentage levels of severity, the resonant frequencies are relatively close to each other. These frequencies are about 3300 Hz more than the SCIM2 resonant

frequency under healthy conditions. Winding inductances and capacitances are a function of material properties, geometry and any short-circuit in the stator winding will result in substantial changes in impedance magnitude at resonance. The results suggest that the impedance differences are caused by the winding inductance and capacitance which can be seen as the impedance peak at different fault conditions decreases substantially when compared with the healthy one. The difference in impedance with respect to the healthy one is 806.91 Ω, 888.19 Ω, 943.18 Ω, 1175.9 Ω for 2%, 4%, 6% and 8% inter-turn short-circuit fault, respectively. This shows that the deviation increases with respect to the percentage number of turns shorted.

We can deduce that data could be trended over time to observe any changes in its resonant impedance. Also, under inter-turn fault condition, the resonant frequency increases while the impedance peak magnitude decreases. Hence, these two indicators are very significant in diagnosing the state of the SCIM stator winding.

Table 5.3: Table of simulated SCIM2 resonant frequency and impedance magnitude peak under different stator winding conditions

SCIM2 Conditions	Resonant Frequency (Hz)	Impedance Peak (Ω)
Healthy	56,100	6398.25
2% inter-turn	59,410	5591.34
4% inter-turn	59,411	5510.06
6% inter-turn	59,412	5455.07
8% inter-turn	59,495	5222.35

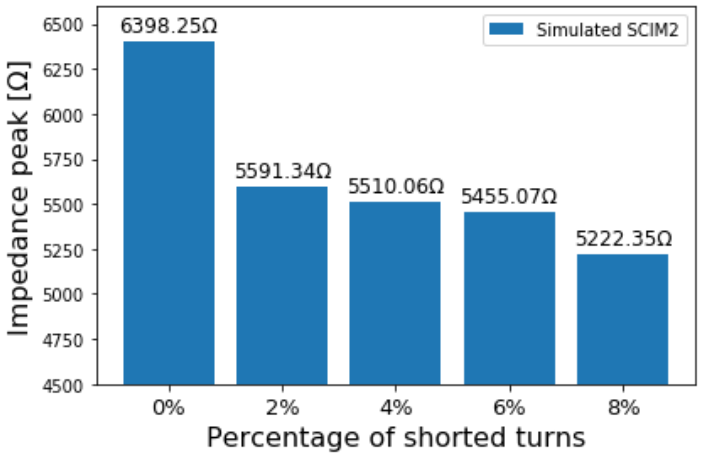

Fig. 5.22: Simulated impedance response peak of SCIM2 at different stator winding conditions

5.3 Conclusion

This chapter presented a lumped parameter model consisting of series resistance, series inductance, and parallel capacitance for SCIM stator winding. The equivalent circuit parameters such as series resistance and inductance considering the skin effect as a function of frequency were elaborated and extracted. The proposed model was implemented to simulate SCIM2 stator winding impedance response using the extracted parameters as a function of frequency. The inter-turn fault for SCIM2 was simulated by reducing the number of turns in the stator winding. The winding equivalent series resistance and reactance results and equivalent winding impedance response for SCIM2 considered in this study at different fault conditions were presented. Finally, the impedance magnitude peak value and resonance frequency are considered key indicators for assessing SCIM stator winding.

Chapter 6

Experimental Setup and Testing Methodology

6.1 Introduction

This chapter details the test equipment and methodology used to execute the experiments to test the study's proposed technique. A silicon steel laminated core inductor and two 3-phase squirrel-cage induction motors were considered, all capable of healthy and inter-turn fault conditions. The first motor is smaller in size than the second motor; however, the second motor can implement more severe inter-turn fault conditions. Another SCIM is also considered with the capability of changing out the rotor to implement a motor with a broken rotor bar. The details of the laminated core inductor, induction motors, data acquisition devices, experimental setup, and testing procedure for both inter-turn and broken rotor bar fault detection will be provided in this chapter.

6.2 Laminated Core Inductor for Emulating the Inter-Turn Fault

A silicon steel laminated core inductor (LACOIN) was built to investigate winding impedance's behaviour as a function of frequency under healthy and faulty conditions. It has about 60 EI laminations, and 350 turns with a copper wire diameter of 0.686mm. An inter-turn fault is implemented with the following percentage number of shorted turns (1%, 3%, and 6%) brought out from the winding, as shown in Fig. 6.1.

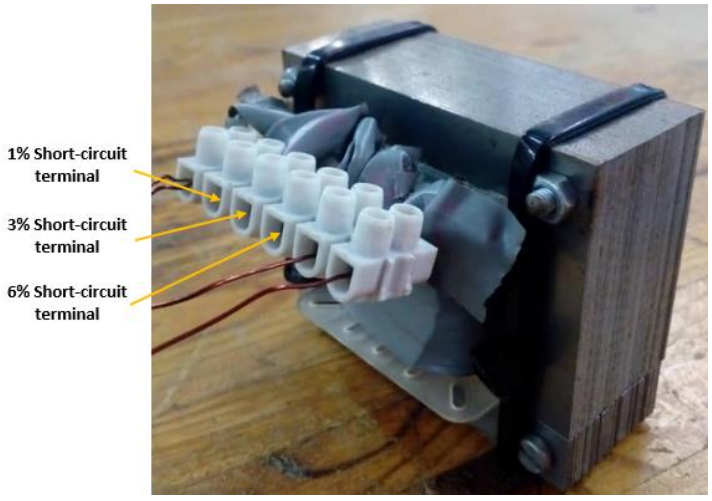

Fig. 6.1: LACOIN for implementing inter-turn faults

6.2.1 DC Resistance of Laminated Core Inductor

This measurement was carried out to confirm the percentage levels of severity since inter-turn short-circuit reduces the number of turns in the winding, reducing its resistance. The DC resistance is determined by supplying a DC voltage to the laminated core inductor up to the nominal current. The current and voltage values for the LACOIN are measured at different percentages of fault severity using the setup in Fig. 6.2. The resistances at different percentages of short-circuit fault conditions (1%, 3%, and 6% short-circuited turns) emulated in the LACOIN winding are calculated using (6.1). These values are shown in Table 6.1.

$$R = \frac{V}{I_{nominal}} \tag{6.1}$$

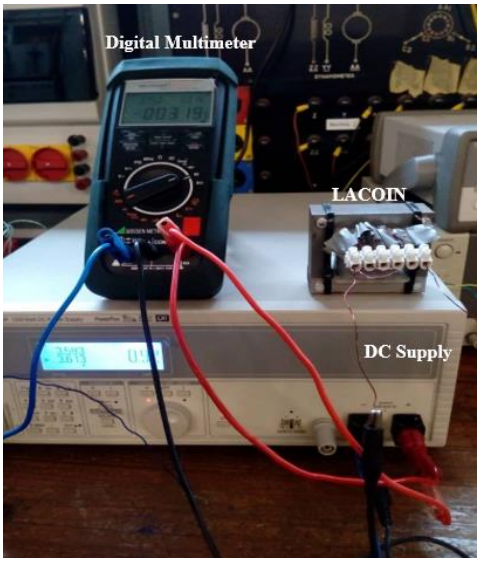

Fig. 6.2: DC measurement of LACOIN at different fault conditions

Table 6.1 shows the DC resistance of the LACOIN measured using the setup in Fig. 6.2 at different percentages of shorted turns conditions.

Table 6.1: DC resistance values for LACOIN in healthy and faulty conditions

State of LACOIN	Percentage of Shorted Turns	DC Resistance Values (Ω)
Faulty Conditions	6%	3.64
	3%	3.75
	1%	3.81
Healthy Condition	0%	3.87

6.3 SCIM for Emulating the Inter-Turn Stator Winding Fault

The SFRA fault detection technique has been experimentally evaluated with two squirrel-cage induction motors where inter-turn faults may be implemented at different levels of severity. This is possible due to tappings brought out from the windings, allowing for the implementation of shorted conditions. The specifications of the induction motor are presented in Table 6.2.

Table 6.2: Characteristics of SCIM used for inter-turn fault detection

Description	SCIM1	SCIM2
	Nominal Values	Nominal Values
Input Voltage	190V	380V
Current	1.85A	15.1A
Power	248.6W	7.5kW
Speed	2850rpm	1455rpm
Frequency	50 Hz	50 Hz
Number of Poles	2	4

SCIM1 is shown in Fig. 6.3. The stator winding of phase A has been tapped across the top and middle terminal to enable five percent of the total number of turns to be shorted. The tapping across the middle terminal and bottom terminal enables seven percent of the total number of turns in phase A to be shorted. Hence, 5% and 7% inter-turn faults are emulated in phase A of SCIM1, respectively.

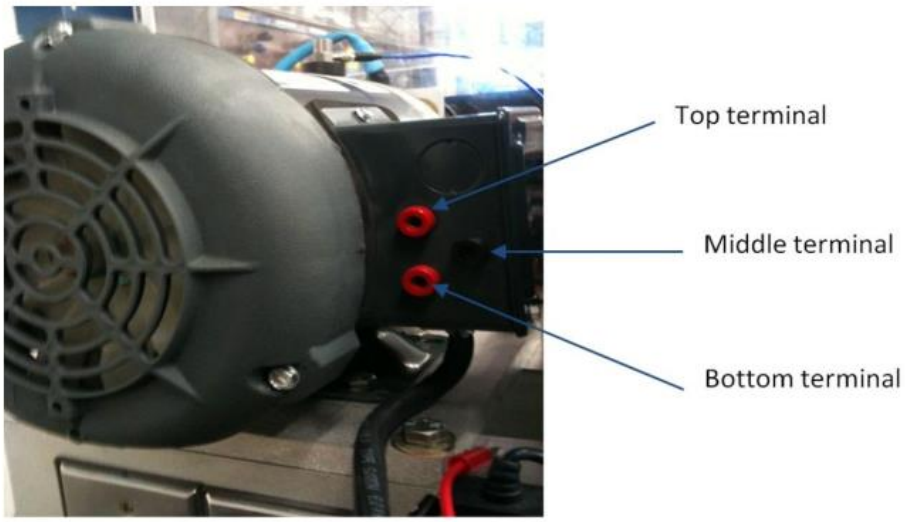

Fig. 6.3: Squirrel-cage induction motor for implementing inter-turn faults.

The SCIM2 winding layout terminals used for inter-turn fault emulation are shown in Fig. 6.4. S and F represent the start and finish of the stator winding per phase. The values of the number of turns for each tapping are described as follows:

- $8\% = 19.2\text{turns} \sim 19\text{turns}$: Tapping on the 11th turn of the 2nd to the last coil.
- $6\% = 14.4\text{turns} \sim 15\text{turns}$: Tapping at the beginning of the last coil.
- $4\% = 9.6\text{turns} \sim 10\text{turns}$: Tapping on the 5th turn of the last coil.
- $2\% = 4.8\text{turns} \sim 5\text{turns}$: Tapping on the 10th turn of the last coil.

Considering phase Y of the stator winding, a connection to terminal YF and YS emulates the healthy condition while YF to Y1, Y2, Y3, or Y4 emulates different percentages of inter-turn short-circuit fault conditions with values 8%, 6%, 4%, and 2% respectively.

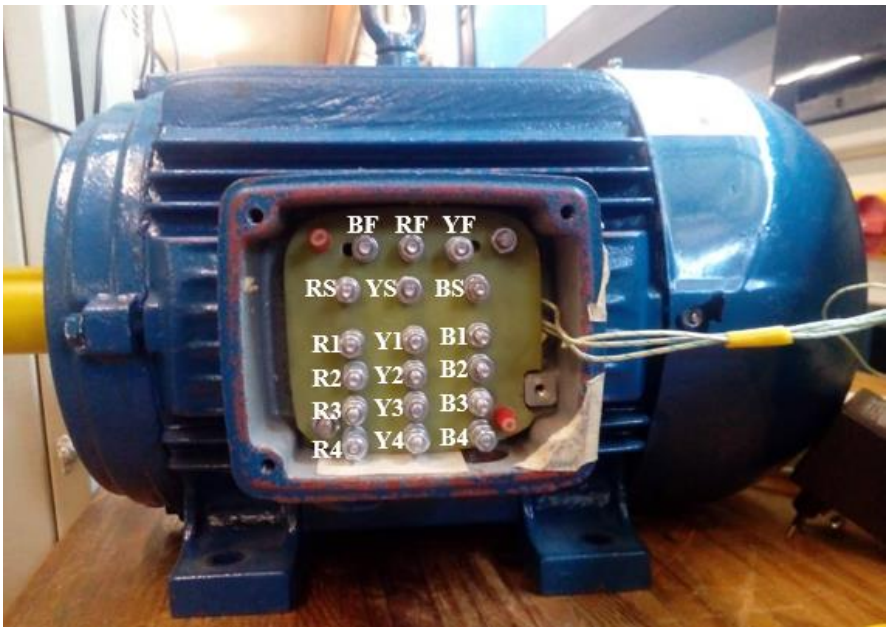

Fig. 6.4: External tappings of SCIM2 stator winding per phase.

6.3.1 DC Resistance of SCIM1

The measured DC resistance values are obtained using phase A and B stator winding terminals of SCIM1 since the windings are star-connected and do not have access to the neutral terminal. These were carried out using the setup in Fig. 6.5 in both healthy and faulty conditions to ascertain the level of severities' values, as shown in Table 6.3. From the measured value, it is observed that the stator winding resistance decreases as the level of severity increases. This decrease is expected because resistance is directly proportional to the conductor's length in the stator winding. Hence, different severity levels reduce the number of turns in the stator winding, affecting the winding resistance.

Fig. 6.5: Stator winding DC measurement for SCIM1

Table 6.3: Phase AB winding DC resistance for SCIM1 in healthy and faulty conditions

State of SCIM1	Percentage of Shorted Turns	DC Resistance Values (Ω)
Faulty Conditions	7%	7.72
	5%	7.92
Healthy Condition	0%	8.34

6.3.2 DC Resistance of SCIM2

The resistance values of SCIM2 stator winding using the setup in Fig. 6.6 are shown in Table 6.4. It is apparent from the measured values that the tappings ultimately represent the shorted turns' emulated percentage. The DC resistance decreases as the percentages of shorted turns increase. As expected, all these values are lower than the DC value resistance of SCIM2 in healthy state conditions.

Fig. 6.6: Stator winding DC measurement for SCIM2

Table 6.4: Phase Y stator winding DC resistance for SCIM2 in healthy and faulty conditions

State of SCIM2	Percentage of Shorted Turns	DC Resistance Values (Ω)
Faulty Conditions	8%	2.20
	6%	2.30
	4%	2.33
	2%	2.36
Healthy Condition	0%	2.40

6.4 Induction Motor for Emulating Broken Rotor Bar

As explained in section 2.7.1, the occurrence of broken rotor bar fault in a SCIM modifies rotor parameters such that the substitute resistance and inductance changes as a function of rotor position, which forms a sinusoidal shape [83]. Hence, measured from the stator side, these parameters will vary with the rotor angle. The specification of the SCIM3 used in this experiment is same as SCIM1, except that the rotor could be interchanged with one with three broken bars.

6.5 Data Acquisition Hardware Device and Interfacing Software

Data acquisition (DAQ) is the process of converting a real-life physical occurrence or phenomenon into computer-understandable data. National Instruments (NI) breaks down this process into the following segments: physical phenomenon, signal processing, DAQ board, drivers, and application software [138]. The NI USB-6366 is an 8-channel X Series multifunction signal acquisition device with a 16-bit resolution, as shown in Fig. 6.7. The analog input ranges are $\pm 1V, \pm 2V, \pm 5V$ and $\pm 10V$ which can capture signals up to 2.0 MS/s. Two out of the eight channels were used to acquire the voltage signal from the function generator and the voltage drop across the stator winding or silicon steel laminated core inductor using the BNC connectors. The signals were sampled at 20 times the input signal frequency to acquire the signals completely. This implies that this device's maximum sampling frequency could completely capture signals up to 100 kHz.

National instrument data acquisition (NI DAQ) devices use NI-DAQmx driver engine or DAQ Assistance to communicate with LabVIEW — an application software (Appendix B). In this

study, the DAQ Assistant in LabVIEW was used to communicate with the data acquisition device, an express virtual instrument (VI) that communicates with NI-DAQmx [139].

Fig. 6.7: NI USB-6366 multifunction signal acquisition device

6.6 Experimental Setup for Fault Diagnosis

The experimental setup for extracting the impedance characteristics for each of the DUT both in healthy and faulty conditions (inter-turn and broken rotor bar fault) is shown below.

6.6.1 Inter-Turn Fault Detection

SFRA is the primary technique applied in this study for winding inter-turn fault detection by extracting impedance response for each of the DUT. The setup for LACOIN, SCIM1, and SCIM2 with and without rotor are shown in fig's 6.8 – 6.11. Each setup consists of the function generator for sinusoidal signal generation, oscilloscope for signal monitoring, and DAQ device for data acquisition and signal processing for impedance extraction. The signal acquired is processed from the personal computer (PC) using LabVIEW software to extract or calculate the current response through the winding and convert the time domain data into the frequency domain.

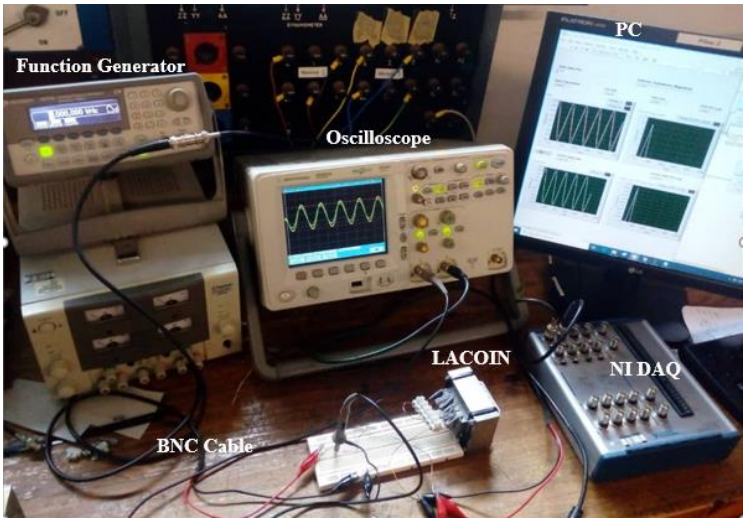

Fig. 6.8: Experimental setup for evaluating LACOIN impedance response

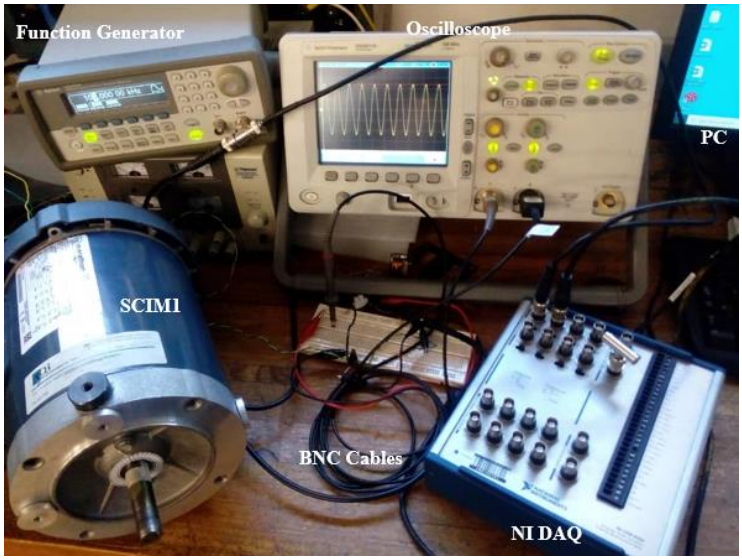

Fig. 6.9: Experimental setup for evaluating SCIM1 impedance response.

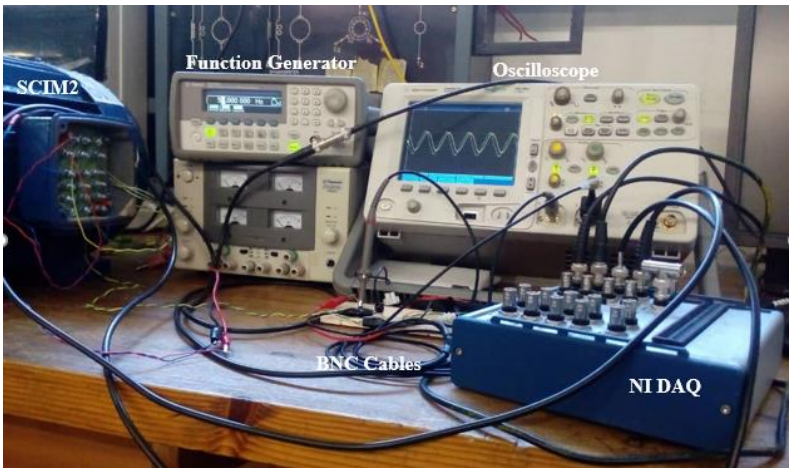

Fig. 6.10: Experimental setup for evaluating impedance response of SCIM2 with rotor

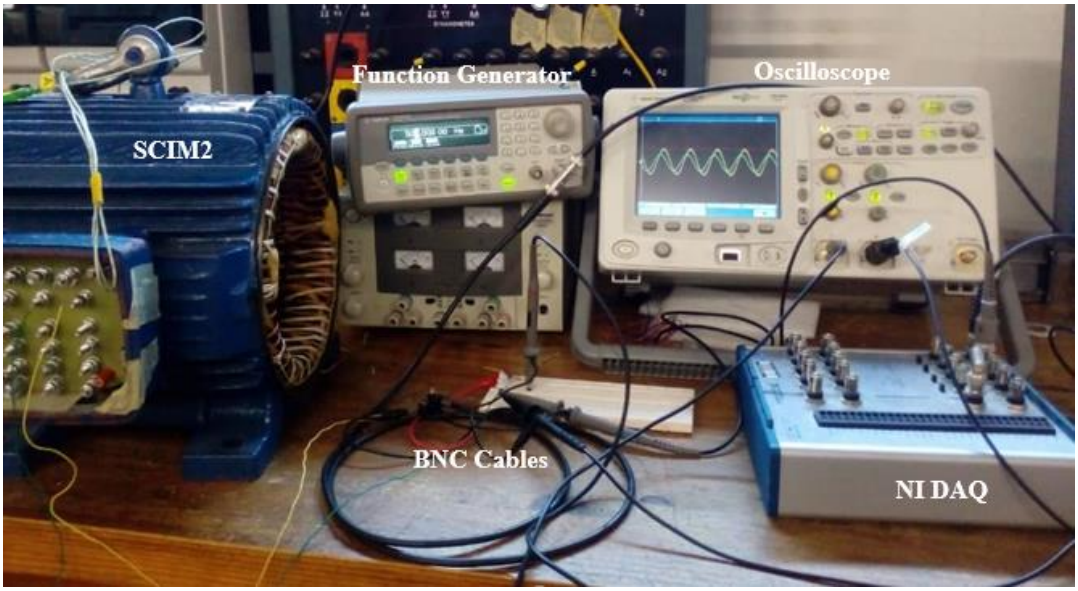

Fig. 6.11: Experimental setup for evaluating impedance response of SCIM2 without rotor

6.6.2 Broken Rotor Bar Fault Detection

Data measured from the test are the input voltage, voltage across the stator winding and acquired using a NI DAQ device through a BNC cable. The current was calculated in LabVIEW using the resistor with value 4.98Ω connected in series with the stator winding as shown in the experimental setup in Fig. 6.12. A digital multimeter was used to monitor the input current from the programmable power supply to the stator winding, where about 100%, 50%, and 25% of the rated current were applied to determine the effect of current on the substitute impedance for broken rotor bar detection.

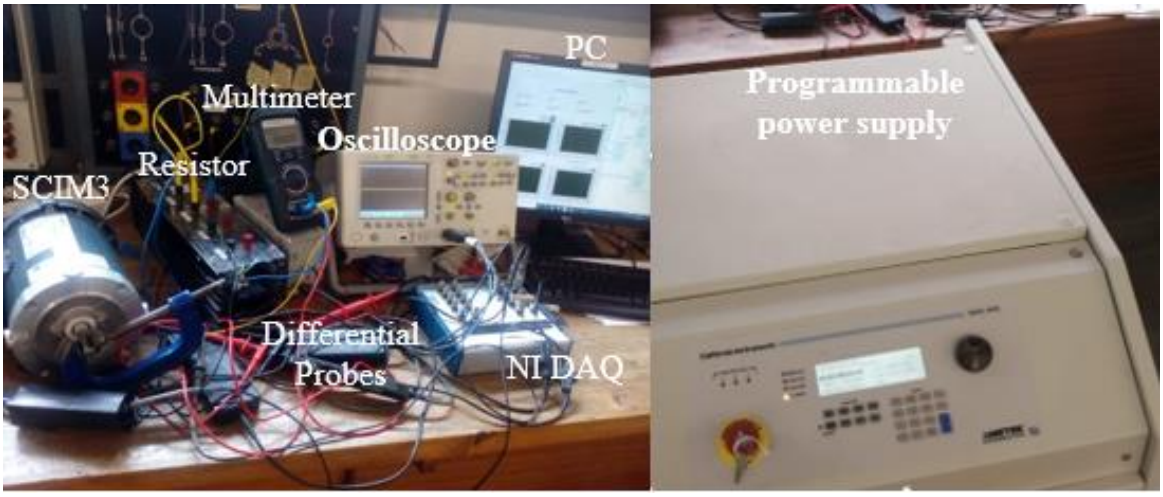

Fig. 6.12: Experimental setup for broken rotor bar fault detection using locked-rotor test

6.7 Testing Methodology

The following testing methodologies were adopted in this study to properly diagnose the state of a squirrel-cage induction motor under inter-turn and broken rotor bar fault conditions, by extracting the impedance magnitude as the significant indicator.

6.7.1 Stator Winding Inter-Turn Fault Diagnosis

The following methodology was applied in this study to determine the device's impedance response under test (LACOIN, SCIM1, and SCIM2) using sweep frequency response analysis (SFRA).

1. A 10V peak-to-peak amplitude sinusoidal signal was generated using a function generator.
2. A resistance of 47 Ω connected in series with the device's winding under test allows the calculation of current flow through the winding. The signal from the function generator was connected across the terminals of the series-connected resistor and winding combination.
3. The input voltage signal and the voltage across the DUT are measured and acquired through a BNC cable using the NI DAQ device.
4. The current response signal of the DUT is determined with the use of LabVIEW software (see Appendix B) and confirmed with Python programming software (see Appendix C) using (6.2).

$$I_{DUT} = \frac{V_{in} - V_{DUT}}{R_{ref}} \tag{6.2}$$

5. DFT was applied to the acquired data using the FFT algorithm in LabVIEW, which converts the data from the time domain to the frequency domain.
6. The impedance response was calculated by dividing the DUT winding's voltage by its current in the frequency domain as in (6.3):

$$Z_{DUT} = \frac{FFT[V_{DUT}]}{FFT[I_{DUT}]} \tag{6.3}$$

where,

V_{in}, is the measured input voltage signal from the function generator

V_{DUT}, is the measured voltage response signal across the DUT

I_{DUT}, is the calculated current response signal of the DUT

R_{ref}, is the reference resistor whose value is 47 Ω.

6.7.2 Broken Rotor Bar Fault Diagnosis

The test was carried out on squirrel-cage induction motor 3 (SCIM3) with a healthy and broken rotor bar to investigate the broken rotor bar's effect on the equivalent parameters shown in section 2.7.1, represented with substitute parameters of resistance and inductance. Since the rotor with a broken rotor bar exhibits electrical asymmetry, the substitute parameters were obtained using a stationary sinusoidal pulsating magnetic field at different rotor angle using the following procedures:

- Two phases of the induction motor stator winding were short-circuited and connected with the other phase to a single-phase supply.
- A single-phase supply using a programmable power supply of California instrument enables the induction motor excitation at frequencies below the nominal frequency, where 16.01Hz is the minimum frequency.
- The rotor was locked with a clamp, and the locked-rotor test repeated at different rotor angles.
- The input voltage and voltage across the stator winding are measured and acquired through a BNC cable using the NI DAQ device.
- The impedance parameter is calculated using the LabVIEW software from the acquired data.

6.8 Conclusion

This chapter discussed the experimental setup and testing methodology for performing SFRA and locked-rotor test measurements for inter-turn and broken rotor bar fault detection, respectively. The device under test (DUT) DC resistance was measured and presented to ascertain the level of severities in each of the DUT windings. The signal measuring instrumentation, data acquisition hardware, and LabVIEW software configurations were developed to measure and capture the signal input voltage and the voltage across the DUT at different frequencies.

The next chapter presents and discusses the impedance response for each of the DUT for inter-turn fault detection.

Chapter 7

Inter-Turn Fault Detection using the Sweep Frequency Response Analysis (SFRA)

7.1 Introduction

This chapter presents the results of the application of sweep frequency response analysis (SFRA) using the methodology in section 6.7 for baseline impedance response and inter-turn fault detection associated with each device under test (DUT), that is, the laminated core inductor, squirrel-cage induction motor 1 and 2. The impedance response plot of the emulated fault conditions in each of the DUT are compared against their baseline for fault diagnosis. The simulated stator winding impedance response of SCIM2 at different fault conditions is also compared with the experimental results to validate the proposed equivalent circuit model.

7.2 Baseline Impedance Response

The baseline impedance response for each of the DUT was performed using the methodology discussed in section 6.7.1 to provide a standard for assessing its condition in future diagnostics. The impedance response analytical results presented in section 4.7 have demonstrated that the resonant frequency is less than 100 kHz, and the impedance magnitude is at its maximum below this frequency, which is a good fault indicator using the SFRA. Therefore, the study's frequency range for fault diagnosis using the testing mentioned above procedures is 0.5 Hz – 100 kHz.

7.2.1 Laminated Core Inductor (LACOIN) Impedance Response Baseline

Sweep frequency response analysis (SFRA) is applied to the silicon steel laminated core inductor (LACOIN) considered in this study to extract its impedance response at different frequencies. The input voltage signal, voltage signal across the LACOIN winding, its current response, and their respective values in the frequency domain at 1Hz are acquired and plotted as shown in Fig. 7.1.

The plot of the LACOIN's impedance response, its real and imaginary parts and phase angle were calculated and are presented in Fig. 7.2, Fig. 7.3, and Fig. 7.4, respectively. From the

impedance response plot, its resonance frequency is observed to be 30120 Hz, which is close to the analytical result of value 31257 Hz with an error of about 3.77%. Moreover, the impedance magnitude at this resonant frequency is 23.3 kΩ which is also close to the analytical result of 23.5 kΩ with an error of 0.85% as illustrated in Fig. 7.5. The results demonstrate that the equivalent circuit model proposed in this study is in good agreement with the experimental results for the considered impedance frequency regions.

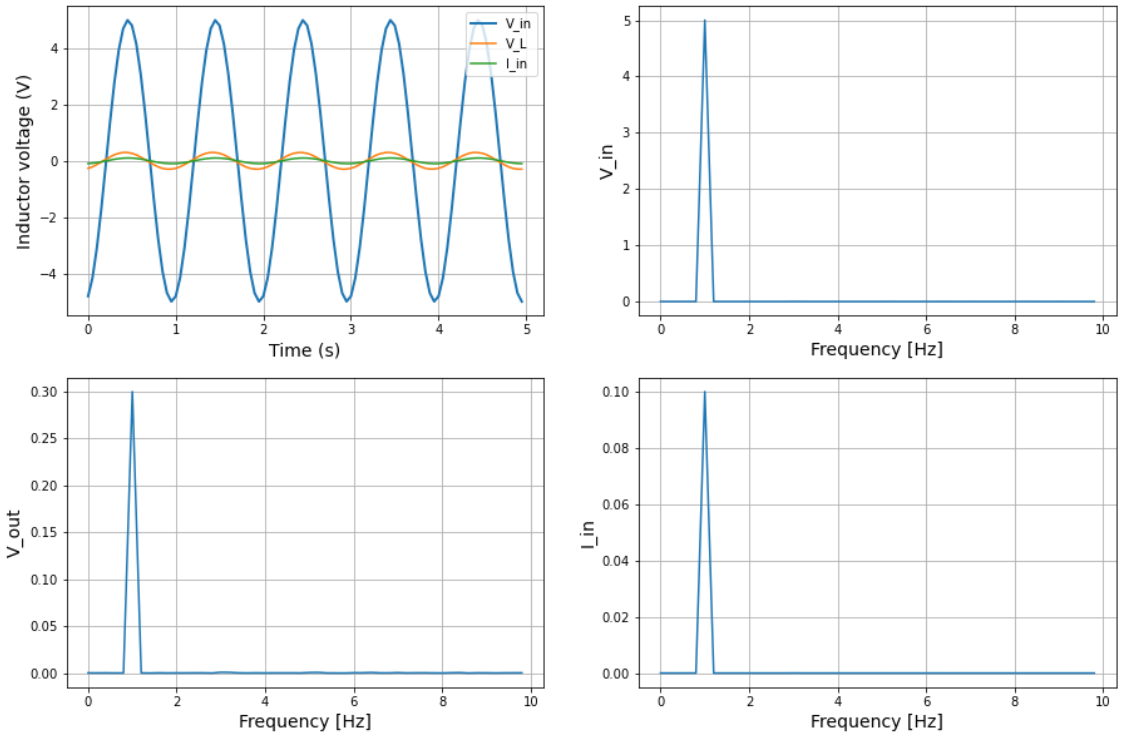

Fig. 7.1: Time and frequency domain of the acquired data for LACOIN at 1Hz

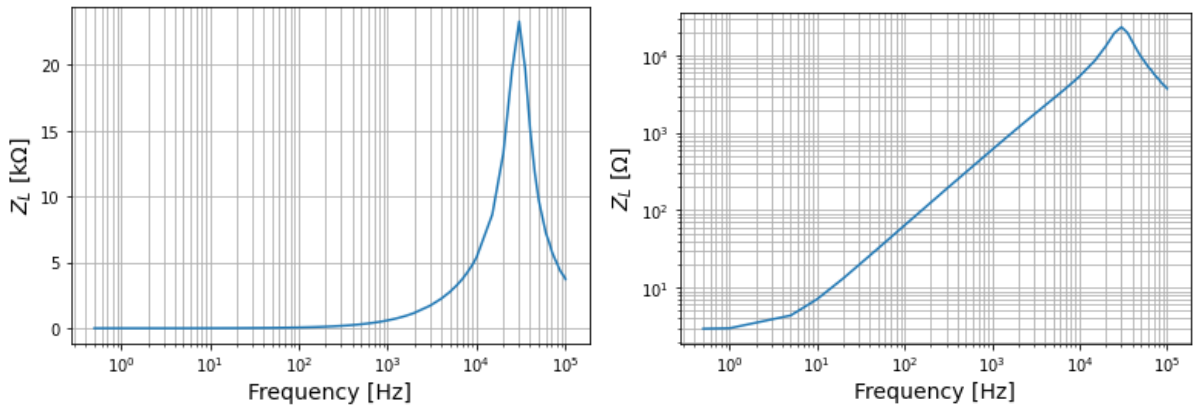

Fig. 7.2: LACOIN impedance response baseline

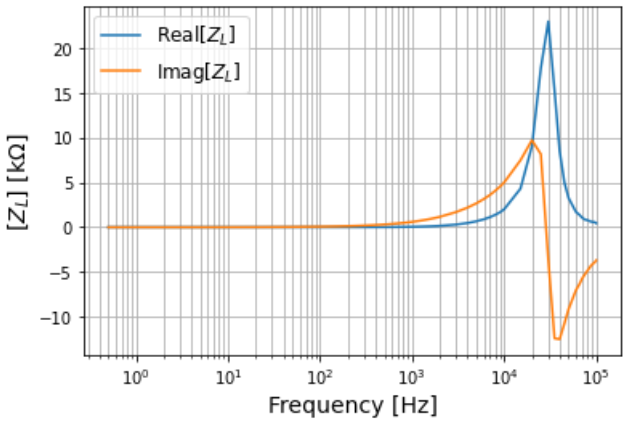

Fig. 7.3: LACOIN impedance response real and imaginary part

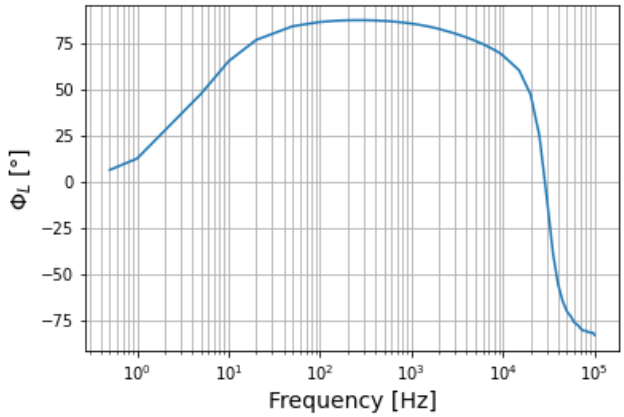

Fig. 7.4: LACOIN phase response baseline

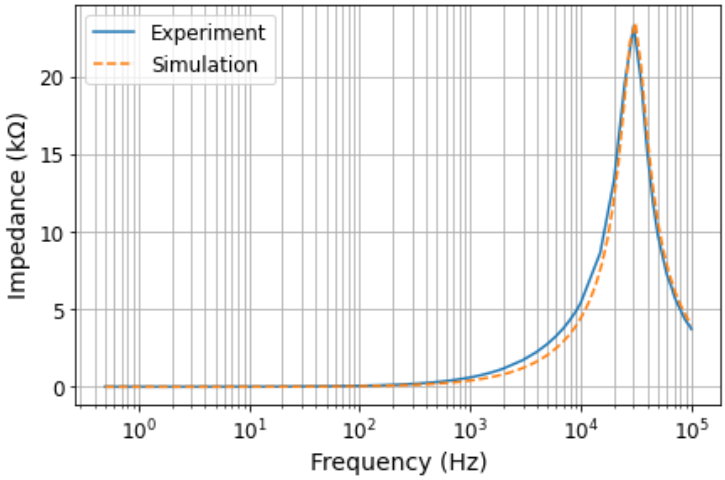

Fig. 7.5: Comparison between simulated model and experimental result for LACOIN

Fig. 7.6 illustrates the current response of the LACOIN at different frequencies when excited with a 10V peak to peak sinusoidal signal. As expected, the current decreases as the frequency

increase due to the skin and proximity effect in the winding, and it is at its maximum when the coil is purely resistive. In this experiment, the maximum current value of the LACOIN is about 100 mA (70 mA in rms) at 0.5 Hz.

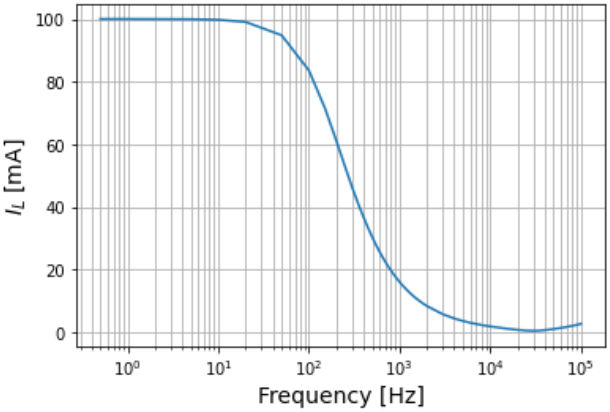

Fig. 7.6: Current response baseline for LACOIN

7.2.2 Squirrel-Cage Induction Motor 1 (SCIM1) Impedance Response Baseline

SFRA was carried out on the SCIM1 stator winding under the healthy condition to determine its impedance response baseline. The voltage signal generated from the function generator was injected through a resistor which is connected in series with two phases (phase AB) of the stator winding. Fig. 7.7 shows the acquired signal at 1 Hz frequency in time and frequency domain where, V_{sw} and I_{sw} represents the voltage across and current through the stator winding of a SCIM1, respectively. The impedance response baseline of this motor in a linear scale is shown in Fig. 7.8.

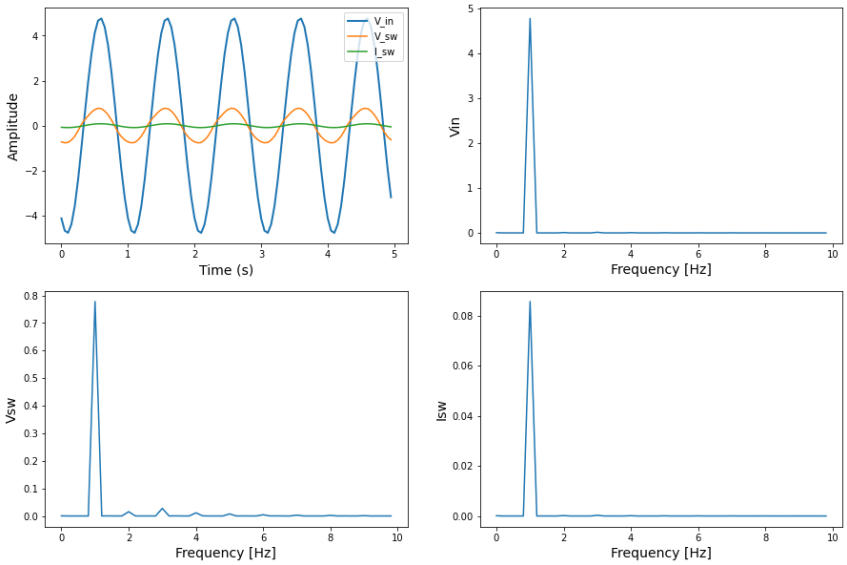

Fig. 7.7: Time and frequency domain of the acquired data

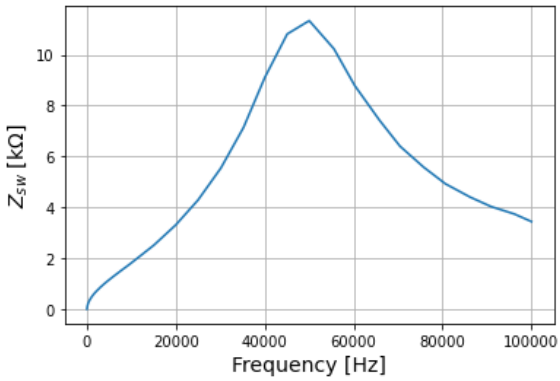

Fig. 7.8: Linear plot of SCIM1 impedance response baseline

Fig. 7.9 shows the baseline impedance response of the SCIM1 in a logarithmic (log) scale. This is often used when displaying spectra because it reveals curve's details that are not as obvious using a linear scale. As expected, the impedance response behaves differently at the three frequency regions. At frequencies below 300 Hz, the inductance is small compared to its resistance, hence, it is dominated by its resistive values. From 300 Hz to the resonant frequency, the plot of the impedance response magnitude of the stator winding shows that the inductance is more prominent. At frequencies above the resonant frequency, the capacitive reactance becomes dominant and reduces the impedance magnitude. The peak value of the stator winding impedance and the resonant frequency of the SCIM1 is about 5660 Ω and 50 kHz, respectively. These two parameters were used as an indicator to diagnose the health state of the squirrel-cage induction motor.

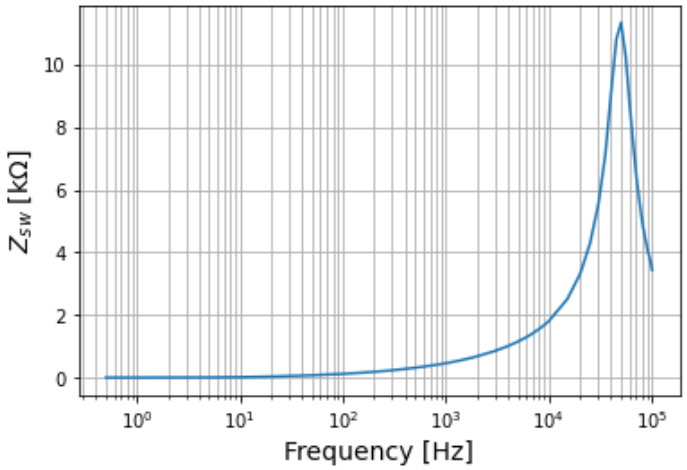

Fig. 7.9: Baseline impedance response for SCIM1

Fig. 7.10 shows the real and imaginary parts of the impedance response, (which is also referred to as equivalent reactance) of the stator winding impedance response under different excitation

frequencies. It is apparent that the real and imaginary parts of the impedance response tend to zero from 0.5 Hz to about 200 Hz. In this range, the impedance response is dominated by the winding resistance. Beyond this frequency range, the real part of the impedance response increases until the peak value which is about 10 kΩ at the resonant frequency of 50 kHz. In this range of frequencies, the stator winding is inductive in nature. The reactive part of the impedance response has a maximum value of about 4381 Ω at the frequencies below the resonant frequency and it has a minimum value of -6506 Ω at frequencies above the resonant frequency. Any deviation from these values could also signify that the stator winding is faulty.

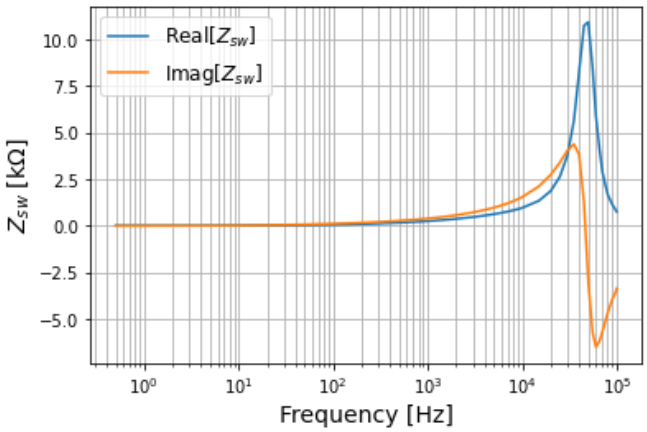

Fig. 7.10: Real and imaginary part of the impedance response of SCIM1

Fig. 7.11 shows the current magnitude that flows through the stator winding at different excitation frequencies. This value is maximum when the winding is purely resistive which is about 87 mA (61.5 mA in rms) at 0.5 Hz. The current decreases as the frequency increases as expected due to the skin effect which tends to resist flux penetration in the stator winding there by increasing the winding resistance. The skin effect is due to leakage flux in the motor's slot and the heterogeneous magnetic conductibility of the slots' surroundings.

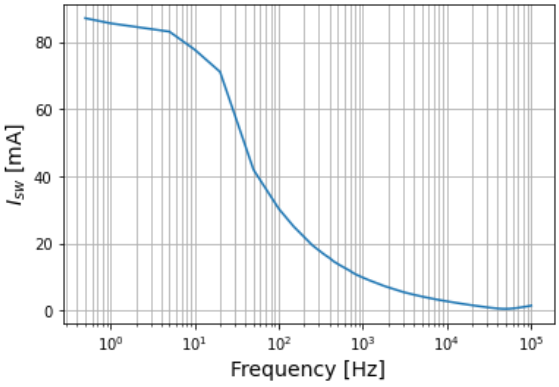

Fig. 7.11: Current response baseline of SCIM1

Fig. 7.12 shows the impedance phase response as a function of frequency. It is observed that, at frequencies less than or equal to 20 Hz, the phase angle increases linearly. This value remains relatively constant from 20 Hz to 20 kHz. However, at frequencies beyond 20 kHz, this value starts decreasing. This is due to the capacitive nature of the stator winding within this frequency range.

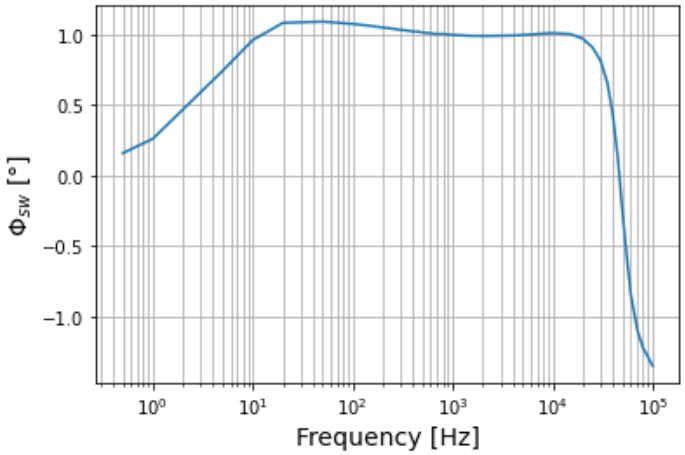

Fig. 7.12: SCIM1 phase response baseline

7.2.3 Squirrel-Cage Induction Motor 2 (SCIM2) Impedance Response Baseline

The methodology discussed in section 6.7.1 is applied to SCIM2 for the baseline impedance response measurement. The voltage input and response signal with their respective frequency domain representation for SCIM2 at 1 Hz are illustrated in Fig. 7.13.

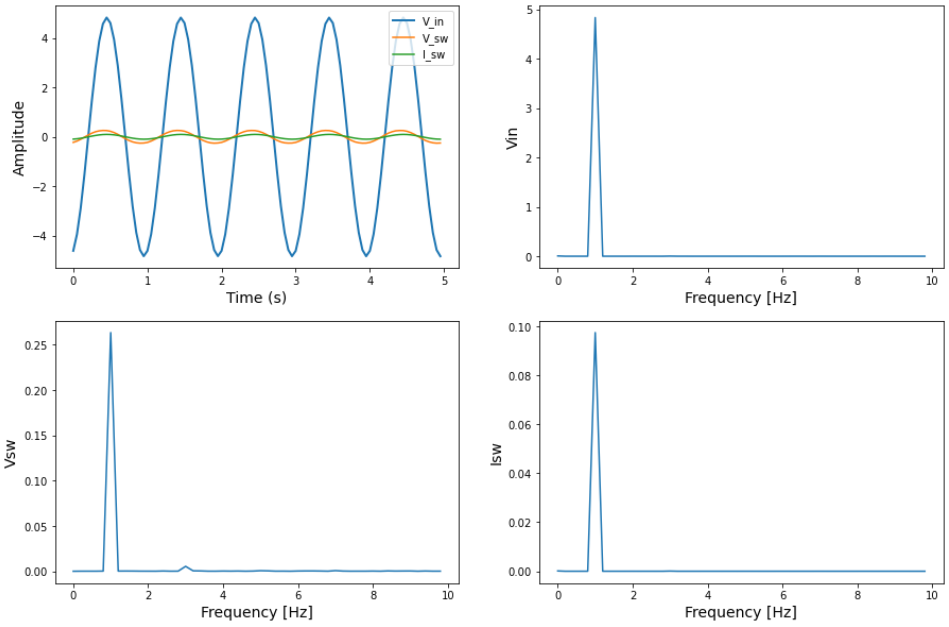

Fig. 7.13: SCIM2 time and frequency domain of the acquired data at 1Hz

Fig. 7.14 show the impedance response of the SCIM2 with an impedance peak of 6414.04 Ω at the resonance frequency of about 60240 Hz. It is observed that the resonant frequency of the simulated impedance response is 56071 Hz which is close to the experimental result with an error of about 6.92%. Furthermore, the simulated impedance response with a peak magnitude of 6398.25 Ω is close to the experimental impedance peak magnitude (6414.04 Ω) at the resonant frequency with an error of about 0.25% as shown in Fig. 7.15. These differences could be because of the coupling at the end-windings or dielectric insulation losses in the winding insulation, which are not implemented in the model. Hence, the results demonstrate that the model proposed in this study for stator winding impedance response resembles the experimental results in the resistive region and frequencies above 30 kHz.

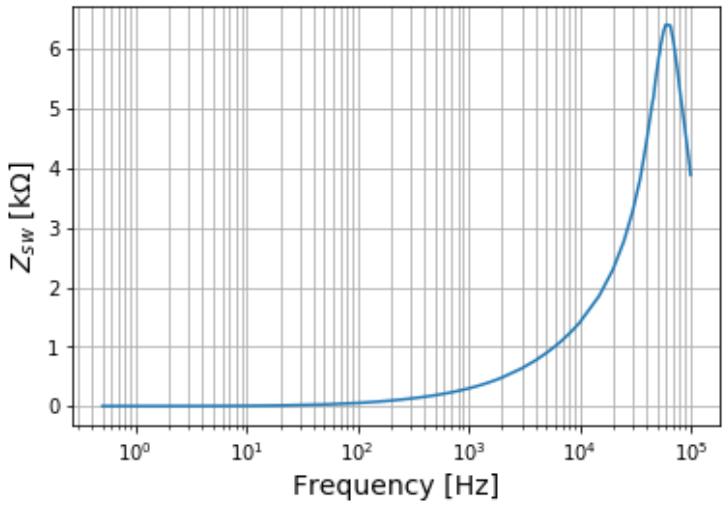

Fig. 7.14: SCIM2 impedance response baseline in logarithmic scale

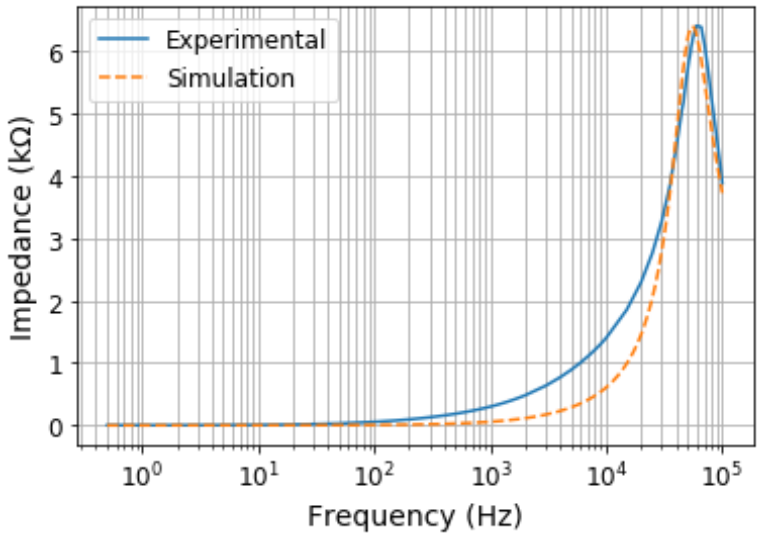

Fig. 7.15: SCIM2 simulated and experimental result

Fig. 7.16 shows the real and imaginary parts of the SCIM2's stator winding impedance response. This impedance response is used as a signature/baseline to determine the induction motor's state in this study. The phase response for the SCIM2 at different frequencies is shown in Fig. 7.17.

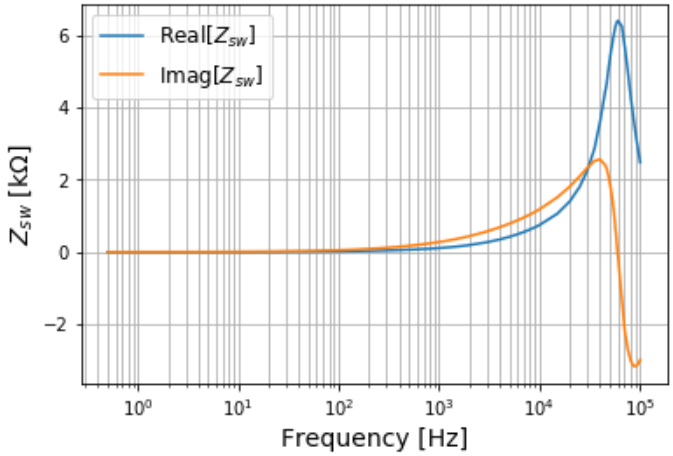

Fig. 7.16: Real and imaginary parts of the impedance response of SCIM2

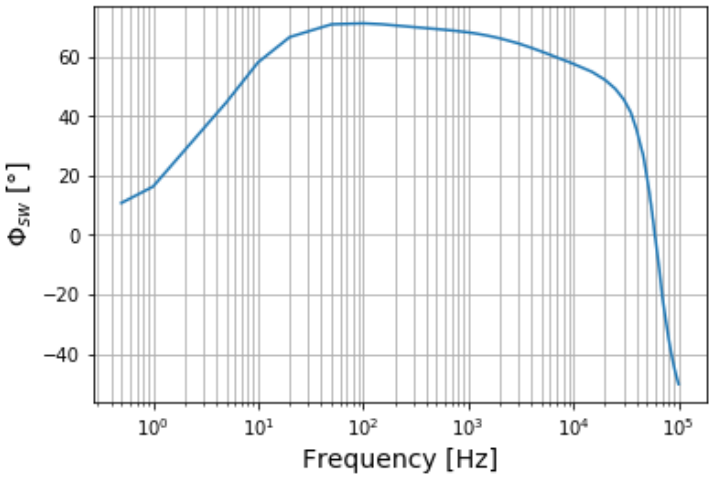

Fig. 7.17: Phase response of SCIM2

Fig. 7.18 illustrates the magnitude of the current response of the SCIM's stator winding at different excitation frequencies. It was observed that the stator current remains relatively constant at frequencies below 20 Hz. Whereas above this frequency, it is inversely proportional to the excitation frequency due to the skin effect on the stator winding. The maximum current through the stator winding is about 99.92 mA (70.7 mA in rms) at 0.5 Hz when the stator winding is close to its resistive nature.

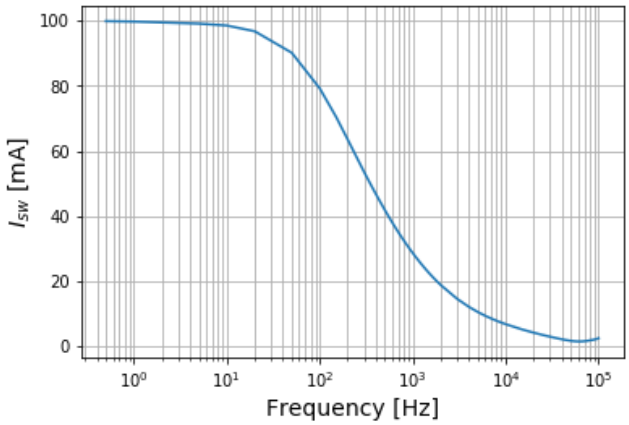

Fig. 7.18: SCIM2 current response

7.2.4 Squirrel-Cage Induction Motor 2 (SCIM2) Impedance Response Baseline without the Rotor

An experiment was conducted on the SCIM2 with the rotor removed to determine whether the rotor's presence has an influence on the behaviour of stator winding impedance response. The baseline impedance response of the SCIM2 without the rotor is presented in Fig. 7.19. The resonant frequency and impedance peak are about 60240 Hz and 10546.43 Ω, respectively.

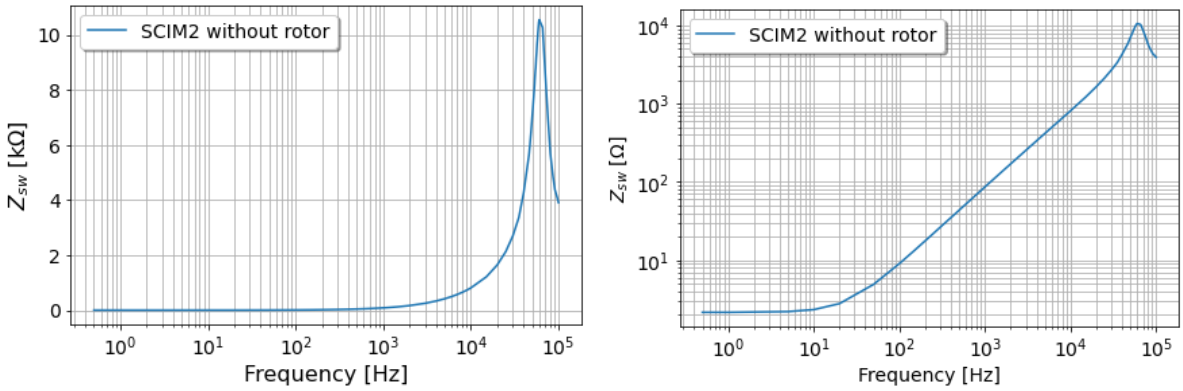

Fig. 7.19: Impedance response for SCIM2 without rotor

In comparison with SCIM2 (with rotor), the impedance responses were plotted and presented in Fig. 7.20. It is clearly observed that the plot patterns are different at each impedance response regions. The impedance response peak of SCIM2 without the rotor is higher than the one with the rotor in place by 4132.39 Ω. Furthermore, the resonant frequency of the SCIM2 without a rotor is the same as that with a rotor as shown in Table 7.1. Therefore, it can be concluded that the presence of the rotor influences the impedance behaviour of a squirrel-cage induction motor by only reducing the peak of the impedance at the resonant frequency.

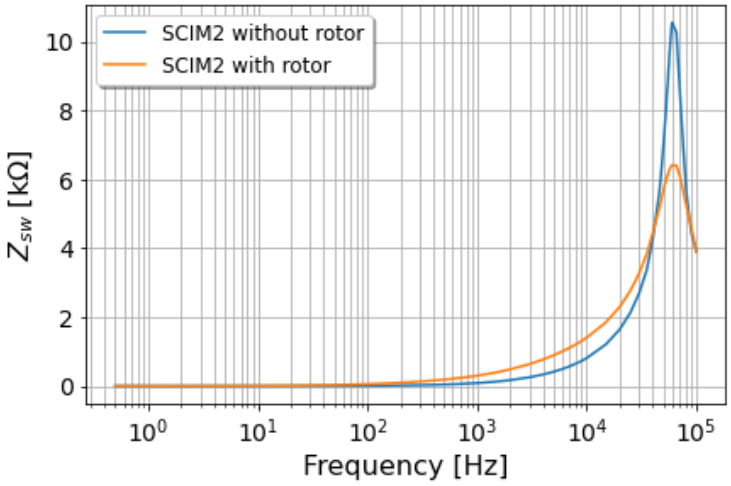

Fig. 7.20: SCIM2 stator winding impedance response with and without rotor

Table 7.1: Table of SCIM2 stator winding with and without rotor resonant frequency and impedance peak under healthy winding condition.

SCIM2 Conditions		Resonant Frequency (Hz)	Impedance Peak (Ω)
Healthy	*Without rotor*	60,240.96	10,546.43
	With rotor	60,240.96	6,414.04

The effect of a rotor on the stator winding impedance response could also be observed in its equivalent reactance as shown in Fig. 7.21. It is observed that the rotor reduces the maximum (positive peak) value of the reactance from about 5.5 kΩ to about 2.6 kΩ but increases its minimum (negative peak) value from about -4.4 kΩ to about -3.2 kΩ.

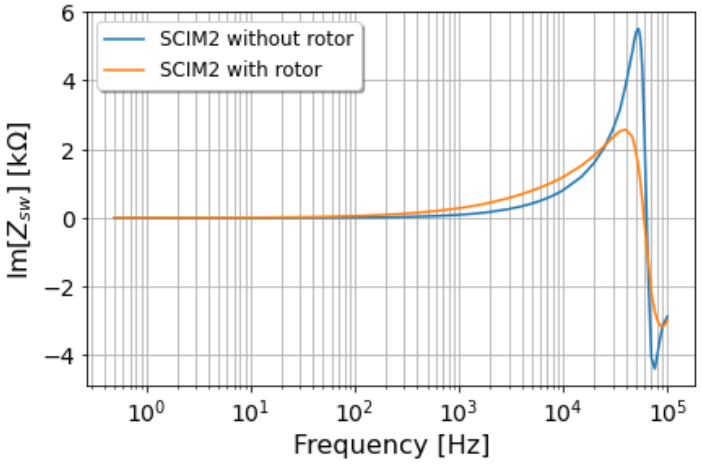

Fig. 7.21: SCIM2 stator winding equivalent reactance with and without rotor

The phase response of the SCIM2 with and without a rotor is presented in Fig. 7.22. The effect of the rotor on the stator winding impedance is observed. At lower frequencies below 80 Hz, the phase values of the SCIM2 with a rotor in place are greater than those without a rotor. Whereas at frequencies between 100 Hz and 600 kHz, the phase values of the SCIM2 with a rotor is lower than the one without a rotor. However, at frequencies beyond 600 kHz, the phase values of both decrease accordingly. The maximum phase value of the SCIM2 with a rotor is about 71.32° while the phase value of that without a rotor is 86.79°. The change in phase value to about 18% at frequencies below 60 kHz shows that the rotor has a significant effect on the stator winding impedance response.

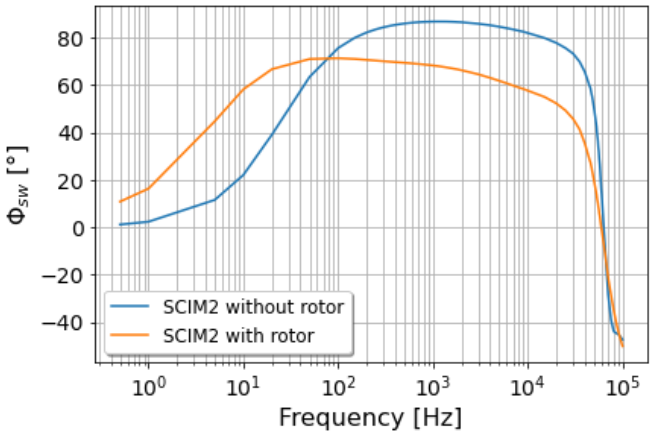

Fig. 7.22: SCIM2 phase response with and without rotor

7.3 Inter-Turn Fault Detection

As discussed in chapter 6, different percentages of inter-turn short-circuit severities were implemented in the DUT winding to emulate the inter-turn fault at different severity levels. Each of these fault conditions has been experimented using the methodology discussed in section 6.7. The resultant impedance response has been plotted and compared with the baseline impedance response. Any deviation in the impedance response plot, especially the peak of the impedance magnitude and the resonance frequency, indicates that the DUT is faulty.

7.3.1 Inter-Turn Fault Detection in a Laminated Core Inductor (LACOIN)

The plot of the measured impedance response and its real part of both the emulated 1% inter-turn short-circuit fault, and healthy LACOIN winding are shown in Fig. 7.23. The impedance response under this condition is the same as the healthy state at frequencies below 1 kHz from the plot. Whereas for frequencies above 1 kHz, some of the basic methods for comparing frequency response as explained in section 3.3.4 is significant and there is a large change in the

impedance response, thereby causing a large shift to the right in the existing resonant frequency to approximately 19880 Hz as shown in Table 7.2. The impedance magnitude also decreases drastically from 23300 Ω to 16360 Ω. This behaviour is also observed in the real part of the impedance response which represents the equivalent resistance in the model discussed in session 4.4. This result shows that this technique could easily detect small changes in the geometrical structure of a coil.

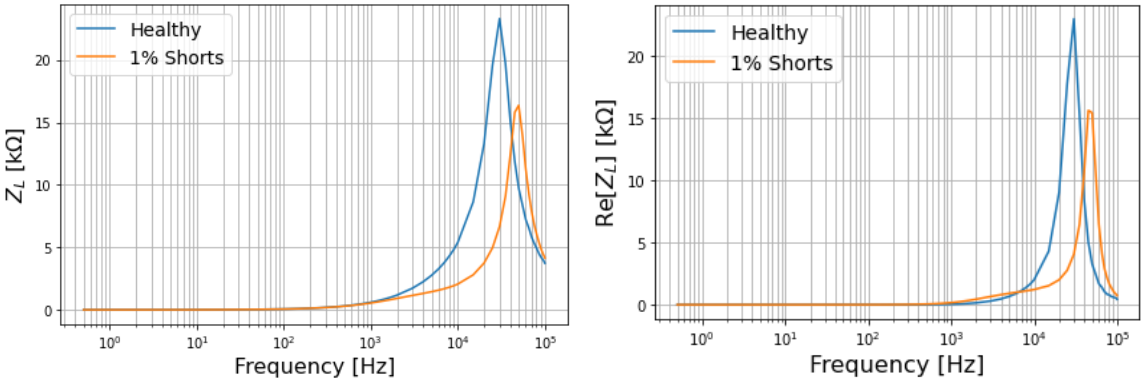

Fig. 7.23: LACOIN impedance response and its real part under 1% short-circuit.

The imaginary part of the impedance response representing the equivalent series reactance of the LACOIN model in section 4.7 and the Nyquist plot is represented in Fig. 7.24. This also shows the effect of 1% inter-turn short-circuit in the LACOIN at higher frequencies. The Nyquist (the relationship between the real and imaginary part of the impedance response) plot clearly shows the coil's state as it curves inward or away from the plot under the healthy condition.

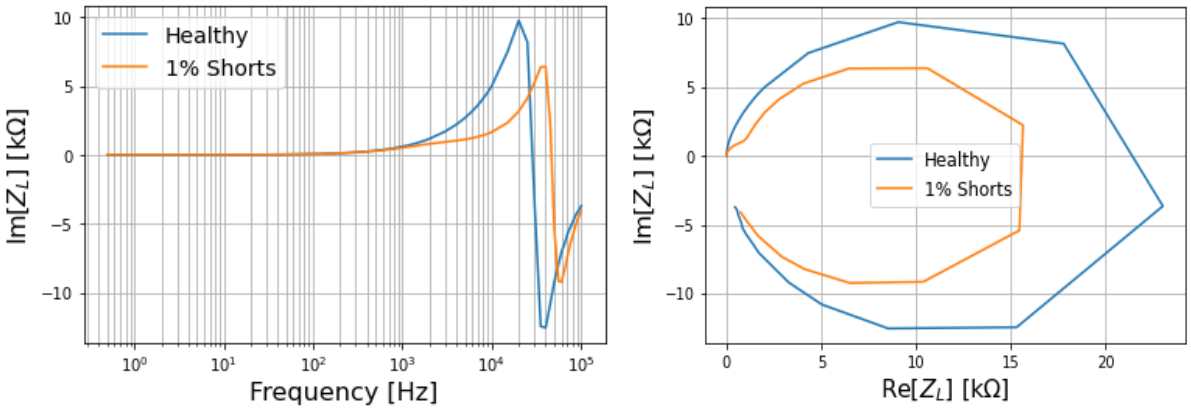

Fig. 7.24: Imaginary part of LACOIN impedance response and Nyquist plot

The LACOIN's baseline impedance response plot is compared with the measured impedance response at different fault levels, as shown in Fig. 7.25. The comparison of both their

impedance peak and resonant frequency are shown in Table 7.2. When a 3% inter-turn short-circuit fault was emulated in the winding, the impedance peak reduced by 9280 Ω from the healthy condition's impedance peak. Its resonant frequency moves further away from the existing resonant frequency by 45630 Hz due to the impedance response plot's shift to the right, which could also be observed from the Nyquist plot. When a 6% inter-turn short-circuit fault was emulated, the resonant frequency is 75800 Hz which is about 45680 Hz away from the baseline resonant frequency. The impedance response peak under this condition is 13360 Ω and is about 9670 Ω below the baseline impedance peak. These plots clearly show that the higher the winding fault severity, the further the impedance response deviates from the baseline measurement by reducing its impedance magnitude and increasing its resonant frequency.

From the previous plot, the LACOIN impedance response behaviour could be grouped into three frequency regions. The first frequency region is from 0.5 Hz to 0.5 kHz, which represents the low-frequency operation region. It is observed that at this range of frequencies, the LACOIN's impedance response is resistive in nature, and the conductor winding resistance is almost a DC resistance. The second frequency range is between 0.5 kHz to the resonant frequency. At this region, the LACOIN's impedance increases showing its inductive nature. Above the resonant frequency, the capacitive nature of the LACOIN is observed, and the impedance response falls from the peak value. In Appendix D, these faults were also detected using the four statistical indicators discussed in this study.

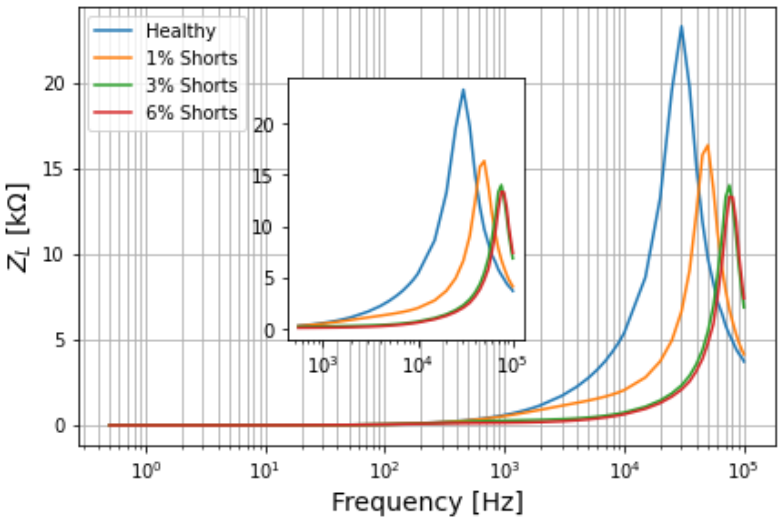

Fig. 7.25: LACOIN impedance response at different fault conditions

The resonant and impedance peak parameters at different states of the laminated core inductor (LACOIN) extracted from the measured impedance response are shown in Table 7.2.

Table 7.2: Table of LACOIN resonant frequency and impedance peak under different percentages of inter-turn short-circuit fault conditions.

Inductor Conditions	Resonant Frequency (Hz)	Impedance Peak (Ω)
Healthy	30,120	23,300
1% inter-turns	50,000	16,360
3% inter-turns	75,750	14,020
6% inter-turns	75,800	13,360

The imaginary part of the impedance frequency response for all percentages of the inter-turn short-circuits fault condition are shown in Fig. 7.26. Two impedance peaks are observed in both the positive and negative reactive axis in the plot. It can be seen that the plots under inter-turn fault conditions deviate from the baseline measurement. The higher the winding severity, the higher the deviation or shift of the reactance response to the right. The imaginary part of the impedance response's values becomes negative beyond the resonant frequency due to the skin and proximity effect caused by the eddy currents in both the windings and core of the LACOIN.

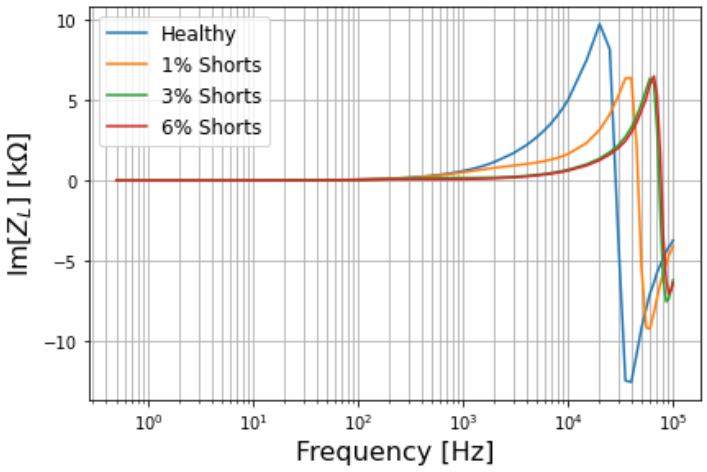

Fig. 7.26: Imaginary part of LACOIN impedance response at different fault conditions

The Nyquist plots of the LACOIN at different winding conditions are shown in different scales in Fig. 7.27 and Fig. 7.28, respectively. The plot patterns reduce and moves away from the healthy state of the LACOIN as the percentage level of the severities in the winding increases. This makes it easier to diagnose the winding by inspecting the plot patterns.

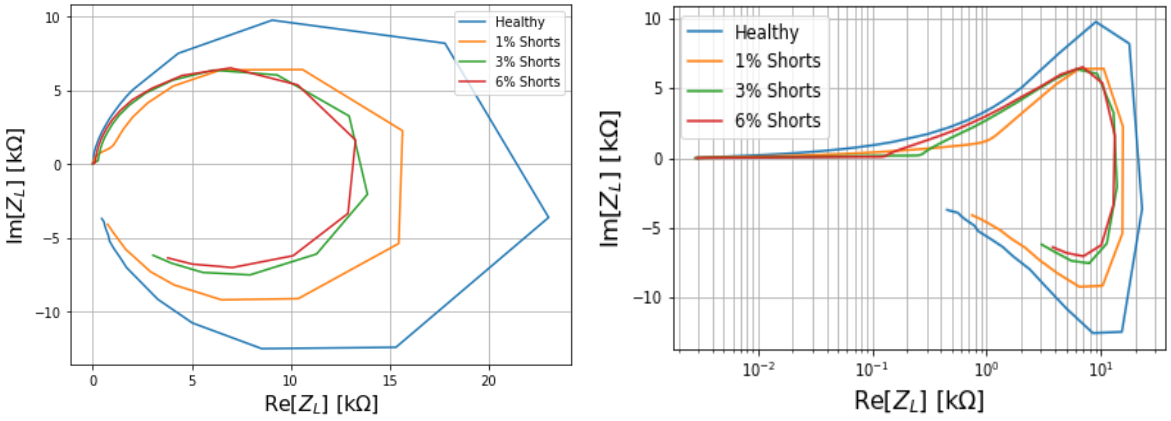

Fig. 7.27: Linear and logarithm representation of the LACOIN's Nyquist plot

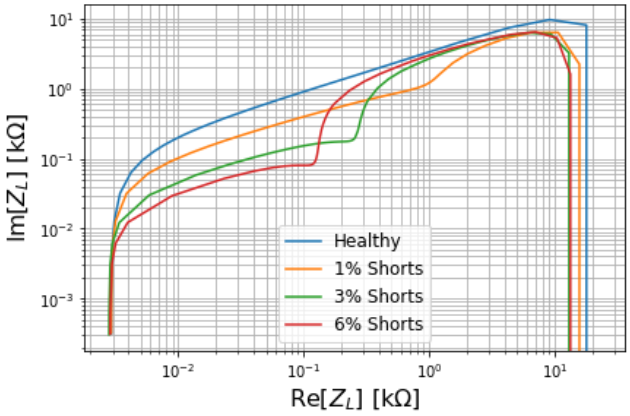

Fig. 7.28: LACOIN Nyquist plot at different winding conditions in Log-log scale

Fig. 7.29 shows the behaviour of current in the LACOIN winding at different frequencies. The current magnitude decreases as frequency increases due to the skin and proximity effect, causing an increase in winding resistance. Each effect alters the current density distribution in the conductor through which the current flows in the winding.

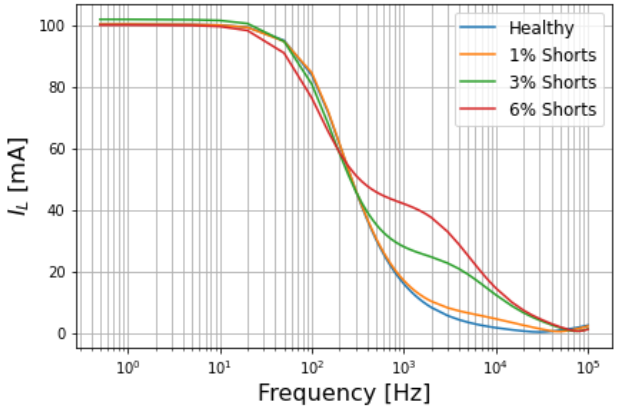

Fig. 7.29: Current plot as function of frequency of LACOIN

Fig. 7.30, gives a better view of the impedance peak and resonant frequency indicators for fault detection at different states of the LACOIN used in this study and gives a better understanding of a coil's behaviour using SFRA. From this plot, it is obvious that the higher the fault severity, the lower the impedance response peak at the resonant frequency.

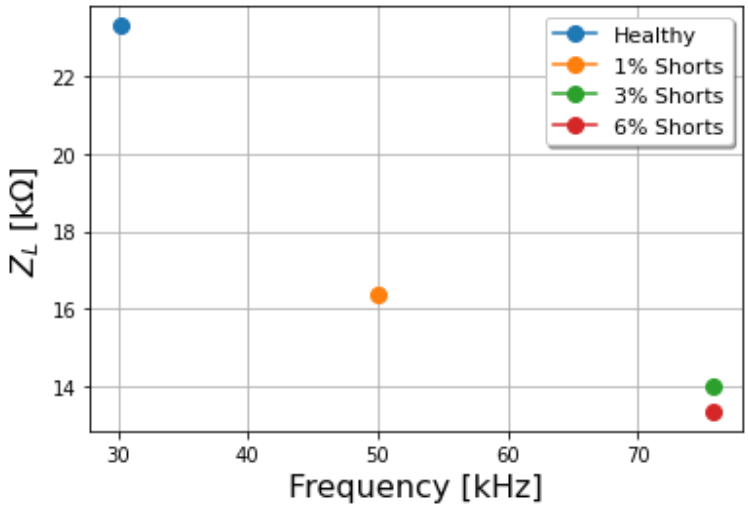

Fig. 7.30: LACOIN impedance peak at resonant frequency

7.3.2 Inter-Turn Fault Detection in Squirrel-Cage Induction Motor 1 (SCIM1)

The impedance response plots of all the stator winding conditions for SCIM1 are shown in Fig. 7.31. The plot pattern of SCIM1 when in good condition is different from the one in faulty conditions. It is important to note two visible indicators to properly diagnose the stator winding: the impedance magnitude peak and the resonance frequency. As seen from the plots, there are clear shifts to the right at resonance frequencies under different fault conditions. The impedance magnitude at healthy, 5% and 7% inter-turn short-circuit faults are about 11330 Ω, 8250 Ω and 7970 Ω, respectively. The impedance magnitude peak difference for each of the fault severity (5% and 7%) from the healthy state is much higher than the impedance response magnitude peak between them. This is because the number of shorted turns between them is smaller in comparison to the ones for each of the fault conditions from the healthy state. The impedance peak value at fault conditions reduces as expected due to the reduction in the number of turns in the stator winding because of the short-circuit. This effect could also be observed using the statistical indicator (see Appendix D). The higher the deviation from the baseline impedance responses, the higher the statistical indicator values (for SD, DABS and ASLE) but vice versa in the case of CC indicator. The resonant frequency for each of the conditions are 50000 Hz, 55555 Hz and 55555 Hz, respectively whereby at the fault conditions,

the resonant frequency remains the same. Both indicators used to diagnose the state of the SCIM1 support the methods used to carry out the SRFA technique. This fault detection method also reflects on the equivalent reactance of the stator winding, as shown in Fig. 7.32. The equivalent reactance of the stator winding extracted from the impedance response, which is measured using the SFRA, shows a clear distinction in the state of the winding when in healthy and faulty conditions (5% and 7% inter-turns short-circuit). The frequencies at the reactance peak values are the resonant frequency and the anti-resonant frequency. These frequencies increase as the level of severity increases as shown Fig. 7.32. The reactance peak at these frequencies could also be used as an indicator to determine the winding state. The stator reactance peak at the positive axis decreases and increases at the negative axis while the plot pattern shifts to the right when this fault occurs in the stator winding.

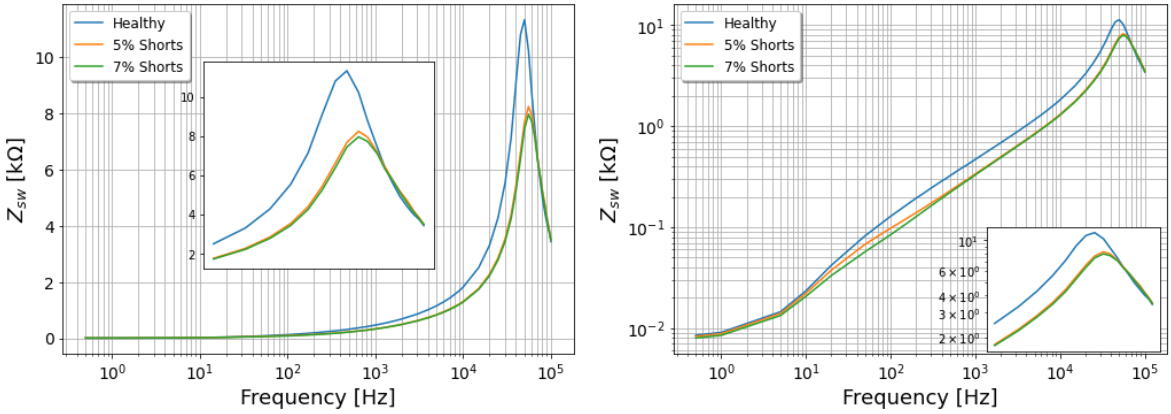

Fig. 7.31: SCIM1 impedance response at different stator winding conditions

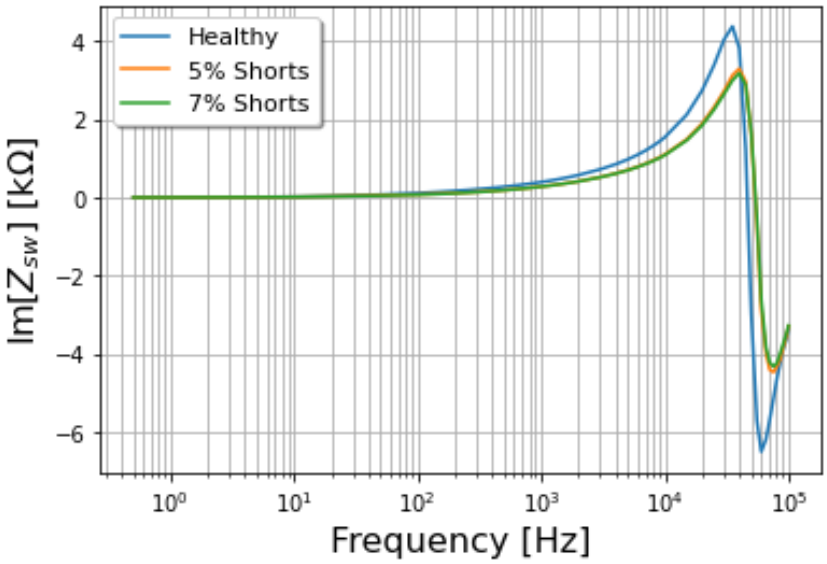

Fig. 7.32: Imaginary part of SCIM1 impedance response at different winding conditions

The Nyquist plot of all the conditions for the SCIM1 at different scales is shown in Fig. 7.33. This clearly shows that at the lower frequencies below 100 Hz, the impedance response reflects the stator winding's resistive behaviour, which is the same under both the healthy and fault conditions. At higher frequencies above 100 Hz which are beyond the motor's operating condition, there is a clear distinction in the Nyquist plot pattern of the healthy and faulty state. It is observed that the plot pattern under fault conditions deviates from the one in a healthy state and curves inward towards the origin.

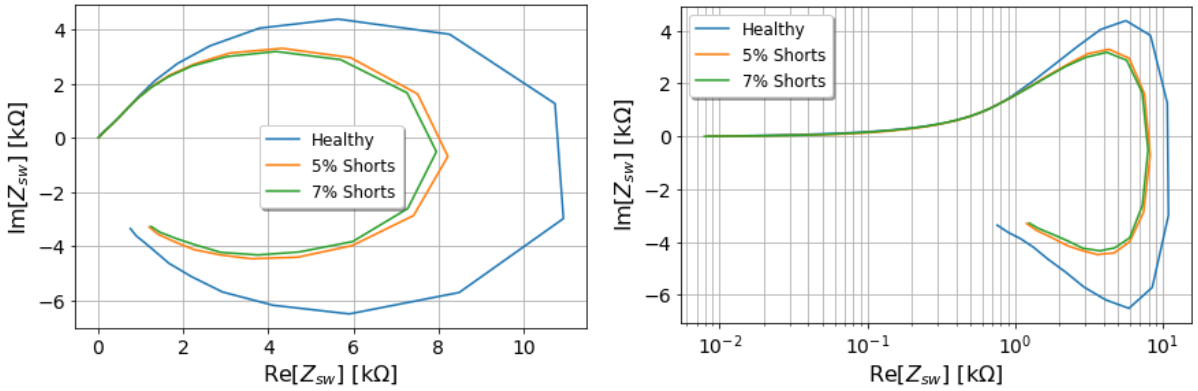

Fig. 7.33: SCIM1 linear and logarithm Nyquist plot at different winding conditions

The current response of the stator winding of the SCIM1 under different conditions are shown in Fig. 7.34. These values strongly depend on the operating frequency of the induction motor. At higher frequencies, the stator winding resistance increases due to the skin and proximity effects caused by winding's eddy current flow. This in turn decreases the current flowing through the winding and is very evident in the plot.

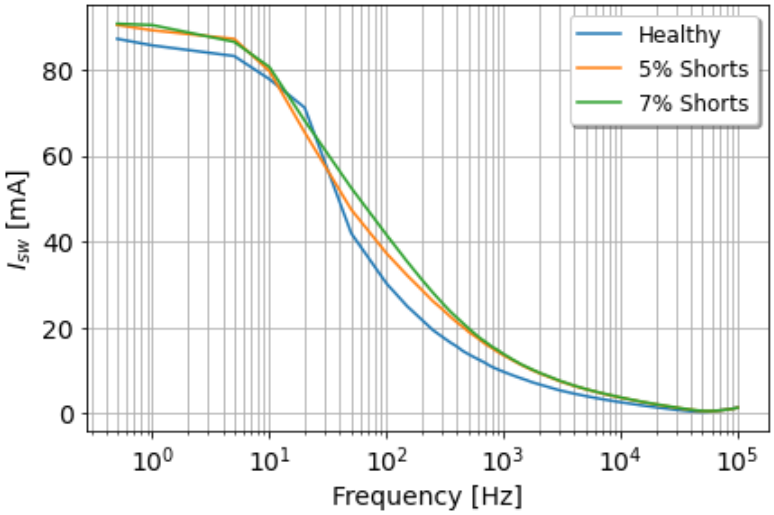

Fig. 7.34: SCIM1 current response at different stator winding conditions

The extracted indicator values (i.e., the resonant frequency and the impedance peak magnitude) from the stator winding impedance response of the SCIM1 using SFRA are shown in Table 7.3. These parameters are used as the basic indicators for this analysis.

Table 7.3: Table of SCIM1 resonant frequency and impedance peak at different conditions

SCIM1 Conditions	Resonant Frequency (Hz)	Impedance Peak (Ω)
Healthy	50,000	11330
5% inter-turns	55,555	8250
7% inter-turns	55,555	7970

The impedance response peak plot against the resonant frequency at different SCIM1 stator winding conditions is represented in Fig. 7.35 and Fig. 7.36, respectively.

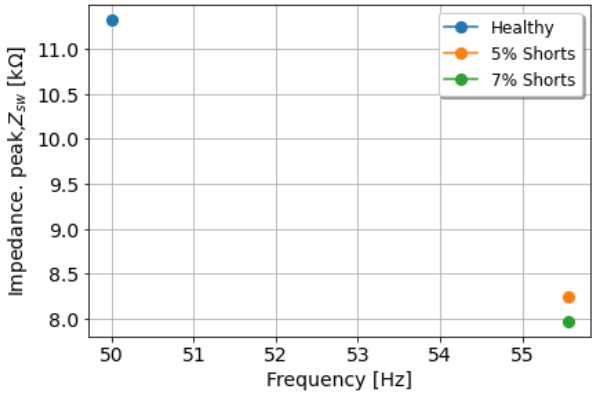

Fig. 7.35: SCIM1 impedance response peak at the resonant frequency

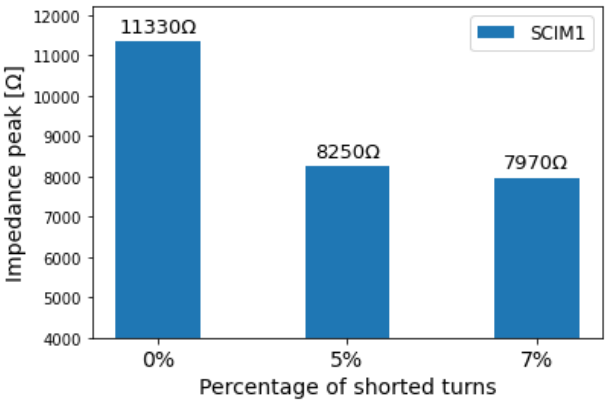

Fig. 7.36: SCIM1 impedance response peak at different stator winding fault conditions

7.3.3 Inter-Turn Fault Detection in Squirrel-Cage Induction Motor 2 (SCIM2)

The SCIM2 impedance frequency response's experimental tests were carried out to validate the proposed methodology for inter-turn fault detection using SFRA. The impedance response results and the imaginary part representing the stator winding equivalent reactance at different percentages of inter-turn fault severities in the stator winding are shown in Fig. 7.37. The SCIM2's baseline impedance response is compared with the measured impedance response under 2% inter-turn short-circuit condition in Fig. 7.37. As expected, the stator winding impedance response magnitude is constant for both conditions at the resistive region. But this value starts increasing at the inductive region up to the resonant frequency, which could be observed in the imaginary plot. At the resonant frequency, the impedance response peak deviates from the baseline value by 759.08 Ω with a shift in resonant frequency of about 5.5 kHz to the right from that of the healthy one. It is observed that there are no significant changes in the capacitive region at both conditions. This result clearly shows that SFRA technique is sensitive to any little change in the stator winding configuration and useful for inter-turn fault detection.

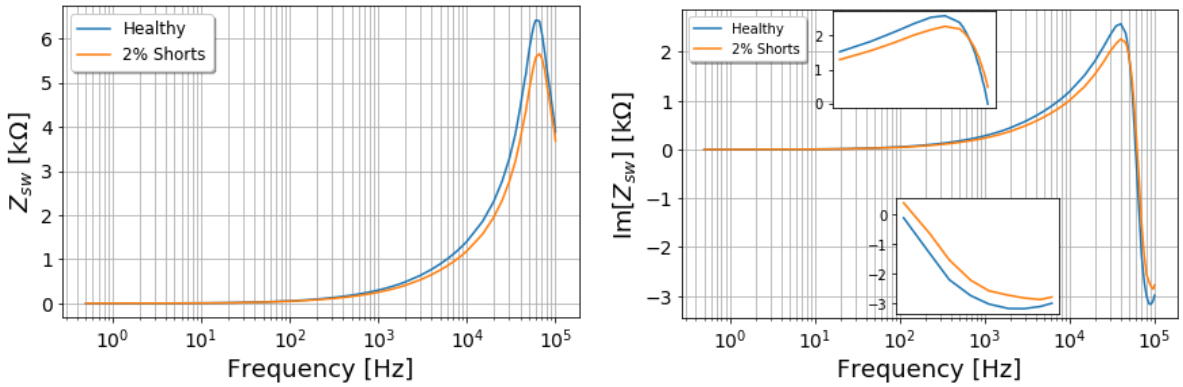

Fig. 7.37: SCIM2 impedance response and it's imaginary part for 2% inter-turn fault

Fig. 7.38 shows the impedance response for the baseline and four different percentages of severity levels of inter-turn fault emulated in the stator winding for SCIM2. At 4% inter-turn short-circuit fault condition, the impedance peak value is 5597.11 Ω, which is about 816 Ω and 57 Ω , below the baseline value and the value at 2% inter-turn short-circuit fault emulated in the stator winding, respectively. Also, at 6% inter-turn short-circuit fault condition, the impedance peak value is 5587.23 Ω, which is about 826 Ω below the baseline value. Finally, considering the 8% inter-turn short-circuit fault condition, the impedance peak value is 5251.69 Ω, which is about 1162 Ω below the baseline value. It is evident that SFRA technique can detect these fault severities using the impedance response peak as an indicator. This value

decreases as the severity level increase due to differences in capacitance. Hence, the percentage level of severity in the stator winding of the SCIM2 is inversely proportional to the impedance response peak value while the resonant frequency at each fault level remains constant.

$$L_{ps} \propto \frac{1}{Z_{sw(pk)}} \tag{7.1}$$

where,

L_{ps}, is the percentage level of severity in the stator winding of the SCIM2

$Z_{sw(pk)}$, is the impedance response peak of the stator winding of the SCIM2.

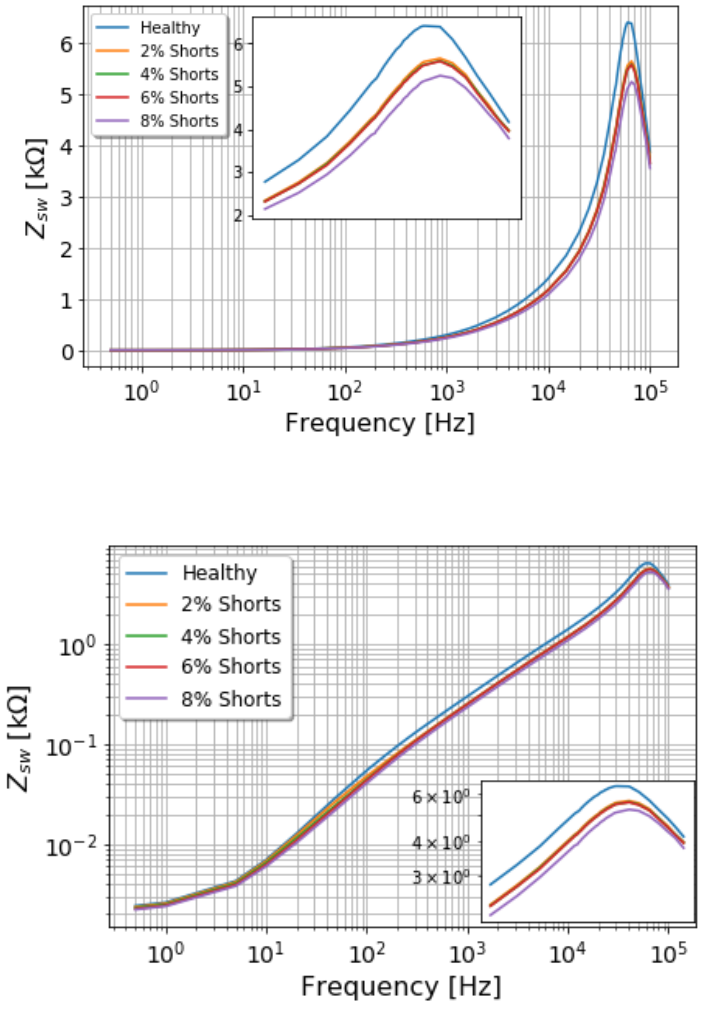

Fig. 7.38: SCIM2 impedance response at different stator winding conditions

Fig. 7.39 shows the imaginary part of impedance responses (i.e., the equivalent reactance of the stator winding) for the baseline condition and the four inter-turn fault severity levels

emulated in the stator winding of the SCIM2. It is evident that the reactance of the stator winding decreases as the fault severity level increases, especially at frequencies above 1 kHz. The reactance starts decreasing at about 30 kHz and becomes negative at frequencies above the resonant frequency. This could be used to diagnose the stator winding of the SCIM as the reactance plot varies at different fault severity.

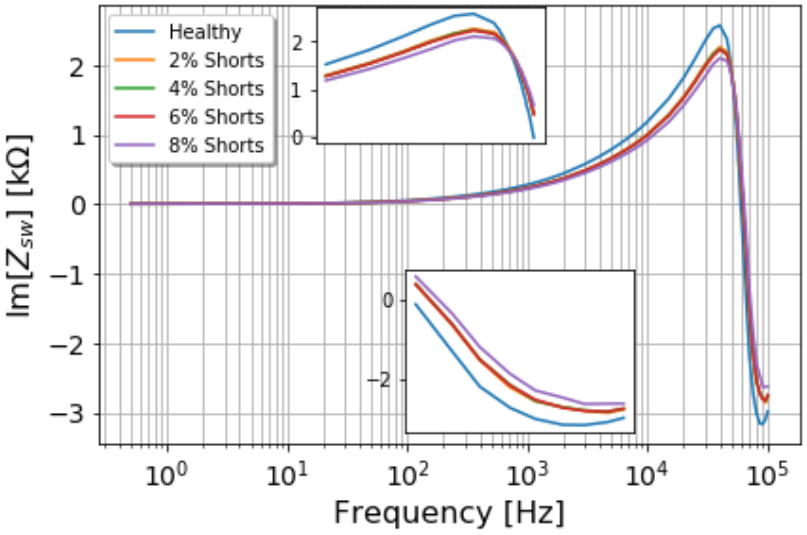

Fig. 7.39: SCIM2 impedance response imaginary part at different fault conditions

Fig. 7.40 shows the relationship between the real and imaginary part of the impedance response at different conditions of the stator winding for the SCIM2. This further shows a clear distinction of the impedance responses of the SCIM2 stator winding at different stator winding conditions. It is observed that at different fault conditions, the Nyquist plot deviates from the baseline curve and moves inward towards the origin as expected. These variations can serve as indicators for the fault detection process.

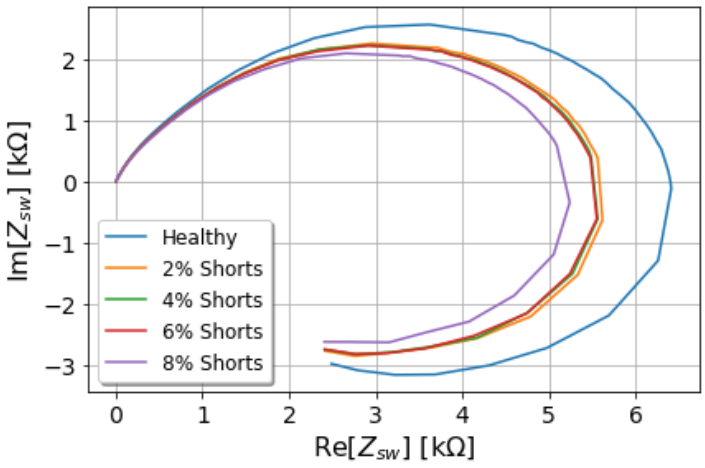

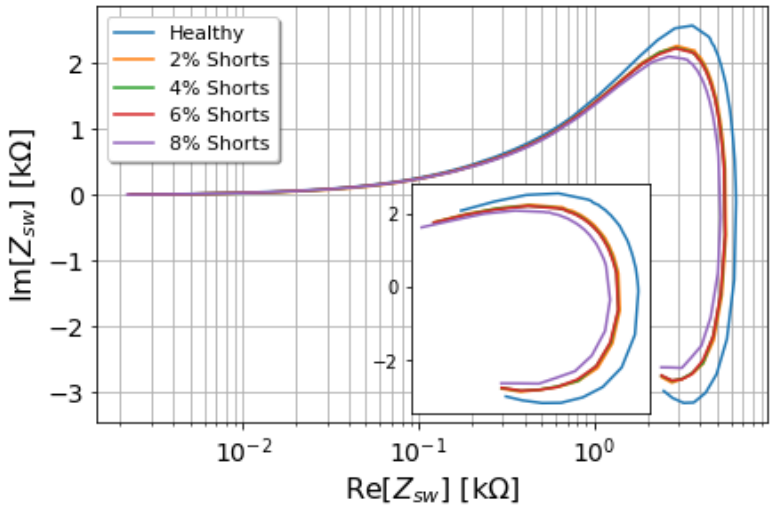

Fig. 7.40: SCIM2 Nyquist plot in linear and logarithmic scale

The extracted impedance response peak and resonant frequency from the magnitude of the stator winding's impedance response for the SCIM2 using SFRA at different percentages of fault severity are shown in Table 7.4. These are used as basic indicators for this analysis. The resonant frequency is the same at every fault condition of the stator winding, while the impedance peak varies as expected.

Table 7.4: SCIM2 resonant frequency and impedance peak at different conditions

SCIM2 Conditions	Resonant Frequency (Hz)	Impedance Peak (Ω)
Healthy	60,240	6414.04
2% inter-turn	65,789	5654.97
4% inter-turn	65,789	5597.11
6% inter-turn	65,789	5587.23
8% inter-turn	65,789	5251.69

The plot of the impedance response peak against the resonant frequency at different stator winding conditions of the SCIM2 is presented in Fig. 7.41. This clearly shows the dependency of the impedance response magnitude peak on the number of turns in the stator winding, which, as expected, reduces due to inter-turn short-circuit fault. This effect could also be observe using the statistical indicator (see Appendix D) as explained in section 3.3.5. It was observed that the

higher the deviation from the baseline impedance responses, the higher the statistical indicator values (for SD, DABS and ASLE) but vice versa in the case of CC indicator.

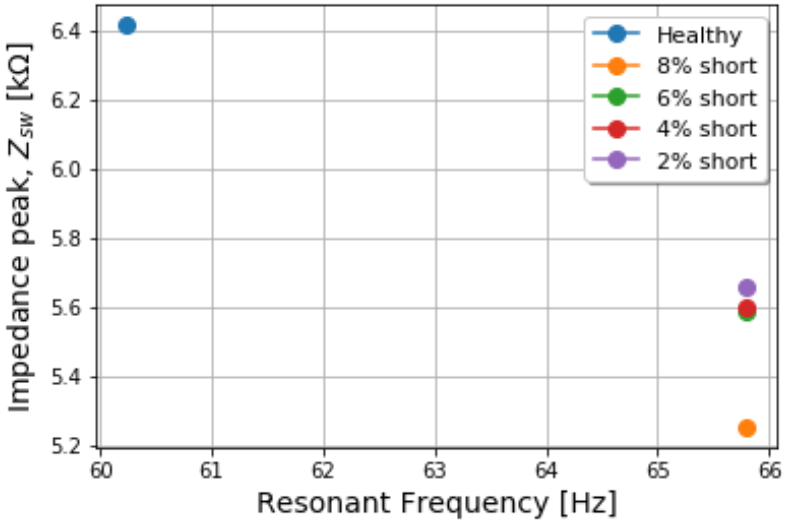

Fig. 7.41: Impedance response peak at the resonant frequency for SCIM2

Comparing the measured impedance response magnitude with the analytical or simulated results at different fault conditions as shown in Fig. 7.42, the following observations have been made, where 0% represents the motor's healthy state. At the healthy state condition, the simulated impedance magnitude peak is about 16 Ω less than its measured value with an error of about 0.25%. At 2% inter-turn fault condition, the simulated impedance magnitude peak is about 63 Ω less than its measured value with an error of about 1.1%. At 4% inter-turn fault condition, the analytical impedance magnitude peak is about 87 Ω less than its measured value with an error of about 1.6%. At 6% inter-turn fault condition, the simulated impedance magnitude peak is about 132 Ω less than its measured value with an error of about 2.4%. Finally, at 8% inter-turn fault condition, the simulated impedance magnitude peak is about 30 Ω less than its measured value with an error of about 0.6%. The impedance magnitude peak values at different stator winding conditions are close with small percentage errors from both analytical and experimental results. Hence, the analytical model agrees with the experimental with a little deviation in the impedance magnitude peak value at different stator winding conditions.

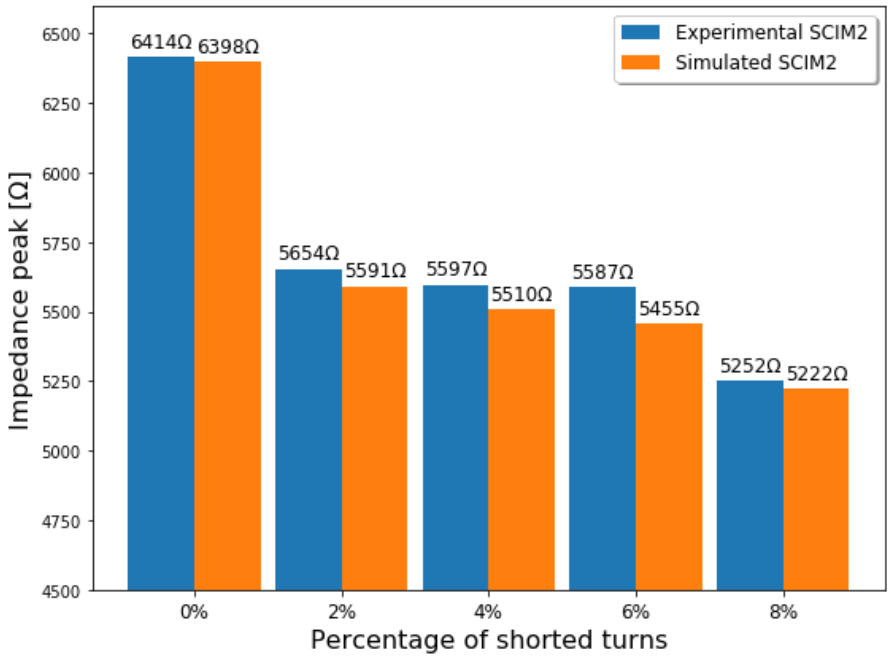

Fig. 7.42: SCIM2 impedance response peak at different stator winding conditions

7.3.4 Inter-Turn Fault Detection in Squirrel-Cage Induction Motor 2 (SCIM2) Without Rotor

To investigates the results for the SCIM2 without a rotor in place, the impedance response as a function of the frequency at different stator winding conditions are presented at different scales as shown in Fig. 7.43. It was observed that the impedance response was mostly affected in the inductive and capacitive regions under fault conditions. This value reduces as the fault severity increases, which reduces the impedance peak as shown in Fig. 7.43. The resistive region is relatively the same at different fault severities.

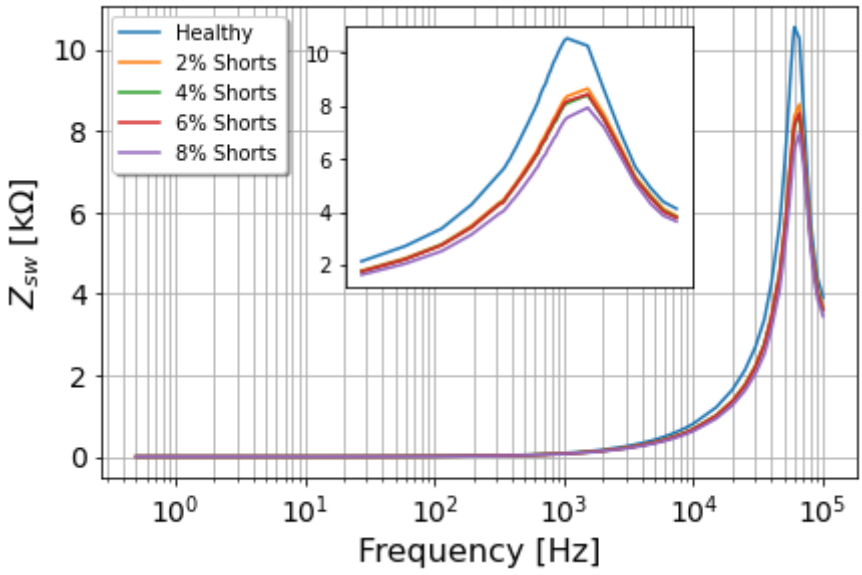

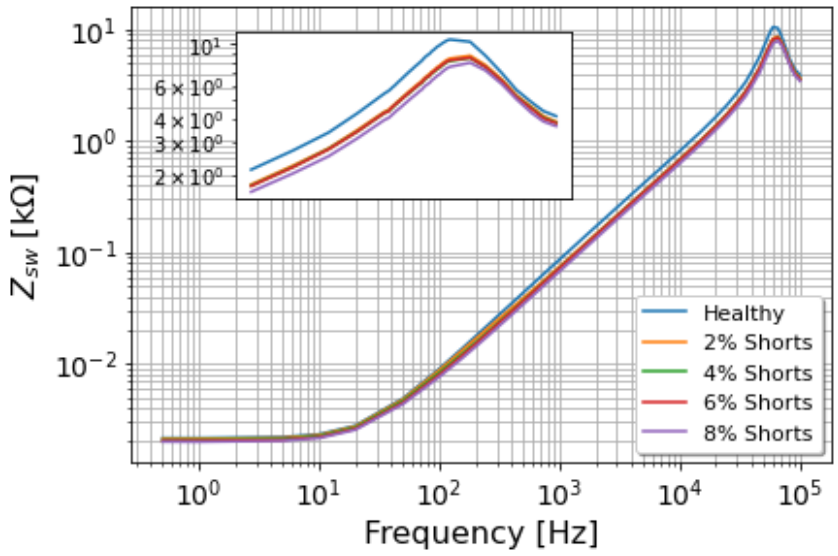

Fig. 7.43: SCIM2 impedance response without rotor for different stator winding conditions

Fig. 7.44 shows the equivalent reactance at different fault conditions. This further shows that the plot patterns at different fault conditions deviate from the baseline plot at the inductive and capacitive regions.

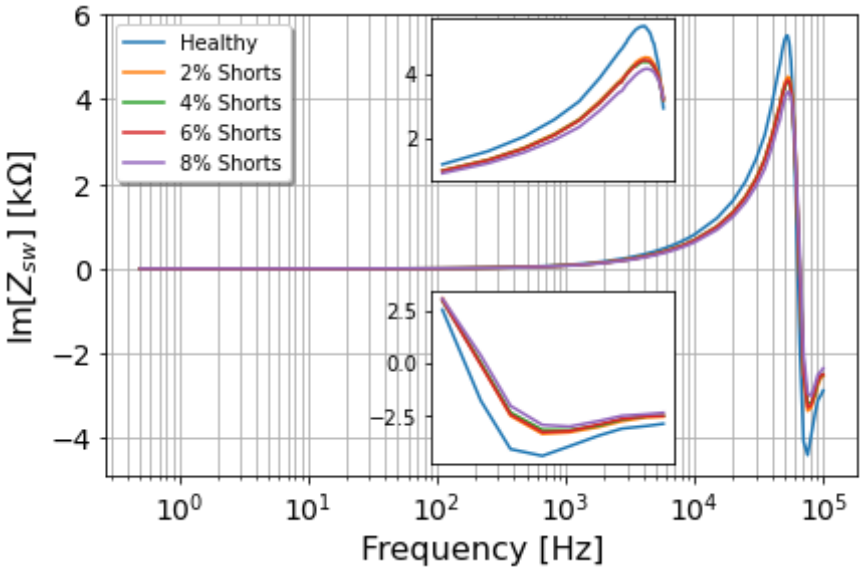

Fig. 7.44: Imaginary part of SCIM2 impedance response without rotor at different fault conditions

Fig. 7.45 shows the impedance response peak at different stator winding conditions of the SCIM2 without the rotor where 0% represents the motor's healthy state. The impedance magnitude peak decreases as the percentage number of shorted turns increases which further shows the capability of SFRA for diagnosing the stator winding of the induction motor.

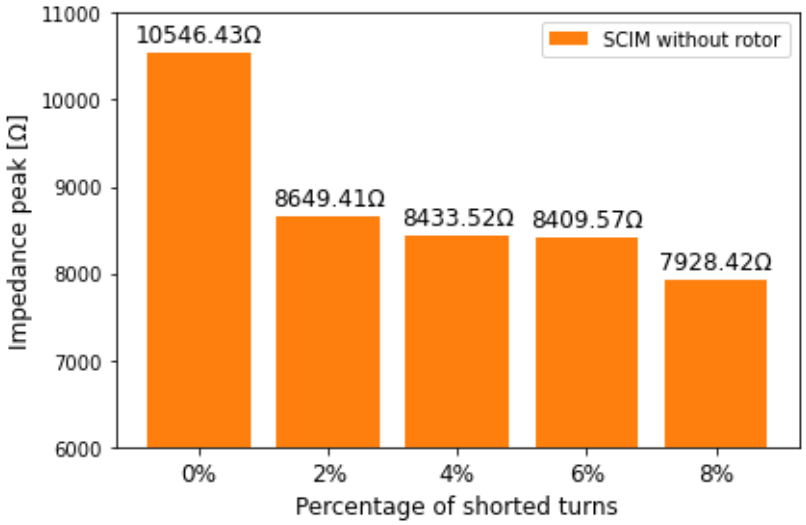

Fig. 7.45: Impedance response peak at different conditions of SCIM2 without rotor

The extracted impedance magnitude peak and resonant frequency from the impedance response of the stator winding of the SCIM2 without rotor in comparison to SCIM2 with the rotor using SFRA are shown in Table 7.5. It is observed that the resonant frequency of the SCIM2 with and without a rotor in place are the same at any stator winding condition. However, this value is different under the fault conditions, and it increases in value. Moreover, the impedance magnitude peak for each of the stator winding conditions for SCIM3 without the rotor are about 2.5 kΩ more than the values with a rotor in place.

Table 7.5: Table of SCIM2 resonant frequency and impedance peak with and without rotor under different stator winding conditions

SCIM2 Conditions		Resonant Frequency (Hz)	Impedance Peak (Ω)
Healthy	*Without rotor*	60,240	10,546.43
	With rotor	60,240	6414.04
2% inter-turn	*Without rotor*	65,789	8649.41
	With rotor	65,789	5654.97
4% inter-turn	*Without rotor*	65,789	8433.52
	With rotor	65,789	5597.11
6% inter-turn	*Without rotor*	65,789	8409.57
	With rotor	65,789	5587.23
8% inter-turn	*Without rotor*	65,789	7928.42
	With rotor	65,789	5251.69

Fig. 7.46 shows the Nyquist plot of the impedance response for the stator winding of a SCIM2 without a rotor in place. This further shows that at different conditions, the resistive regions are almost the same. At the inductive and capacitive region, the Nyquist curves for the faulted windings deviate from a healthy winding curve and tend to move towards the origin.

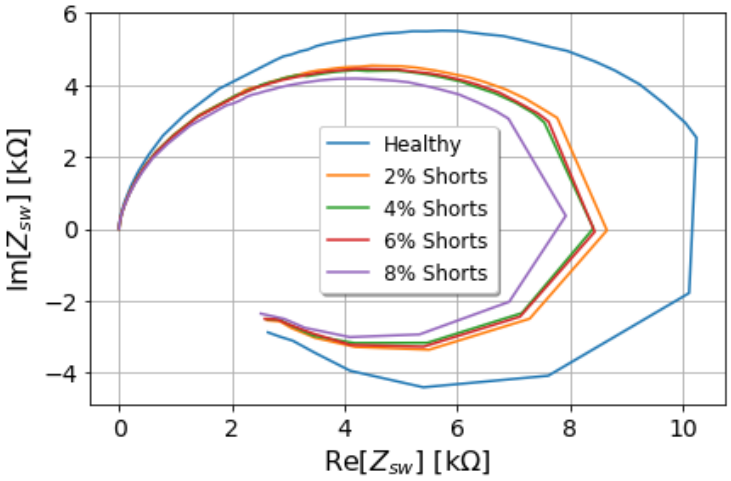

Fig. 7.46: Nyquist plot of SCIM2 without rotor in linear scale

7.4 Conclusion

In this chapter, the experimental diagnosis of inter-turn faults according to the proposed impedance response procedure has been investigated. The impedance response results for the LACOIN, SCIM1 and SCIM2 with and without a rotor in place obtained under the healthy and emulated inter-turn fault conditions have been presented. Any deviation from the baseline impedance response peak signifies that the device under test (DUT) is faulty. It was observed that the resonant frequency of the impedance response increases under the fault conditions. For SCIM1 and SCIM2, the resonant frequency under the fault condition is 9.2% and 11.1% more than its value under healthy conditions. The difference (1.9%) is due to the impact of the winding configuration and geometrical stator winding parameters which is different for both squirrel-cage induction motors. Also, sweep frequency response analysis (SFRA) is very sensitive to the winding geometrical structure, which causes the impedance magnitude peak to reduce as the level of severity increases in the winding of the device under test (DUT).

Hence, from the results of the two SCIMs considered in this study, the sweep frequency response analysis (SFRA) technique using the impedance transfer function measurement has been observed to be suitable for diagnosing the inter-turn short-circuit faults in the stator winding of SCIMs.

Chapter 8

Broken Rotor Bar Fault Detection using the SFRA and Locked-Rotor Test

8.1 Introduction

In this chapter, the squirrel-cage induction motor 3 (SCIM3) with a broken rotor bar fault (BRB) is investigated to determine whether its impedance information can serve as an indicator for broken rotor bar faults since this has not been thoroughly explored before. The experimental study begins by firstly considering the conventional Sweep Frequency Response Analysis (SFRA), after which an adapted approach is pursued, one which is better suited to the nature of the fault but still evident within its impedance. The specification for the SCIM3 has been discussed in section 6.4.

8.2 Impedance Response of the SCIM3 at Different Rotor Angles using the SFRA

SFRA is applied to SCIM3 stator winding to investigate the broken rotor bar (BRB) effect at different rotor angles on its impedance response. In this experiment, the different rotor angle positions of the induction motor under study are achieved by rotating the rotor shaft manually.

The impedance response analysis for the SCIM3 with a healthy rotor bar (HRB) at different rotor angles was conducted using the methodology explained in section 6.7.2, and the results are illustrated in Fig. 8.1. The result shows that there is no significant difference in the impedance response plot pattern for the SCIM3 with a healthy rotor bar at different rotor angles as expected.

In comparison with the SCIM3 with a BRB, the same procedure is applied considering 20 angular positions of the rotor. The results in Fig. 8.2 shows the impedance response of the SCIM3 with a BRB as a function of frequency at different rotor angle positions. It was observed that, there is a clear distinction in the pattern of impedance response plot at different rotor angles compared with the SCIM3 with a healthy rotor bar (HRB).

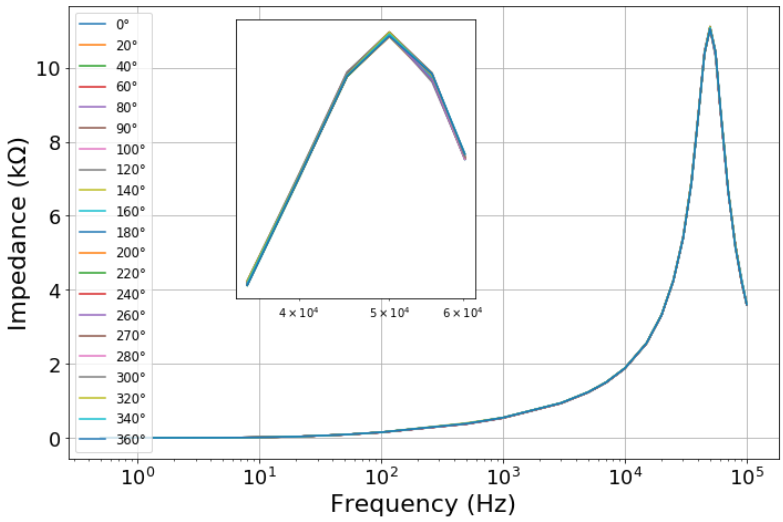

Fig. 8.1: SCIM3 with HRB impedance response at different rotor angle

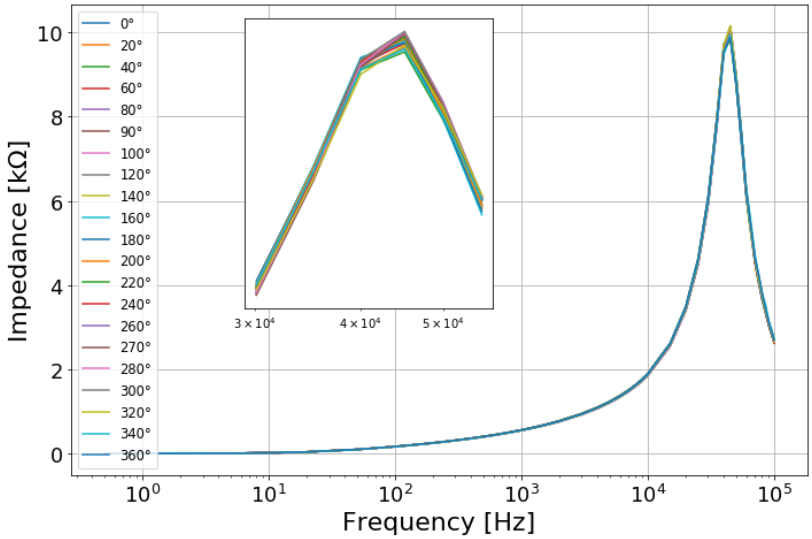

Fig. 8.2: SCIM3 with BRB impedance response at different rotor angle

It is expected that SCIM with a BRB should have a significant effect in the impedance measurement from the stator side since changing the rotor angle position causes differences in the rotor parameters. From the plots (Fig. 8.1 and Fig. 8.2) shown above, this is not evident at the resonant frequency. The resonant frequency of the SCIM3 with a HRB and a BRB is 50 kHz and 45 kHz, respectively which is constant at every rotor angle position. Moreover, the average impedance peak at resonance for the SCIM3 with a HRB and a BRB is about 11108 Ω and 10155 Ω. This further shows that there is no clear distinction in the impedance response behaviour at both conditions at different rotor angles. Hence, the SFRA technique may not be applicable for broken rotor bar detection since it requires a low input voltage, which produces a low current and low magnetic field. Since in a SCIM, the researcher only has access to the

stator winding for parameter extraction and needs further information of the rotor from the stator side, a higher magnetic field which depends on the excitation current up to the rated current of the motor, is required to diagnose SCIM with a broken rotor bar accurately. Hence, impedance extraction under the locked-rotor test is considered in this study for this purpose.

8.3 Impedance Extraction using Locked-Rotor Test

The occurrence of broken rotor bar faults in a SCIM modifies the rotor parameters such that the substitute resistance and inductance changes as a function of rotor position, which forms a sinusoidal shape [83]. Since the rotor with a broken rotor bar exhibits electrical asymmetry, the substitute impedance parameter was obtained using a stationary sinusoidal pulsating magnetic field at different rotor angles with excitation currents much higher than the one applied using the SFRA technique. Hence, measured from the stator side, the impedance parameter will vary with the rotor angle. The squirrel-cage induction motor results under the healthy and broken rotor bar fault conditions are presented in the next section and discussed in detail.

8.3.1 Healthy Rotor Bar Results

The substitute impedance of the SCIM3 with a healthy rotor bar was investigated to understand their behaviours at different rotor angle positions. A stationary sinusoidal pulsating magnetic field is generated in the stator winding with current excitation of about 100% of the rated current to obtain the substitute impedance from the stator side at different rotor angles and frequencies, as shown in Fig. 8.3.

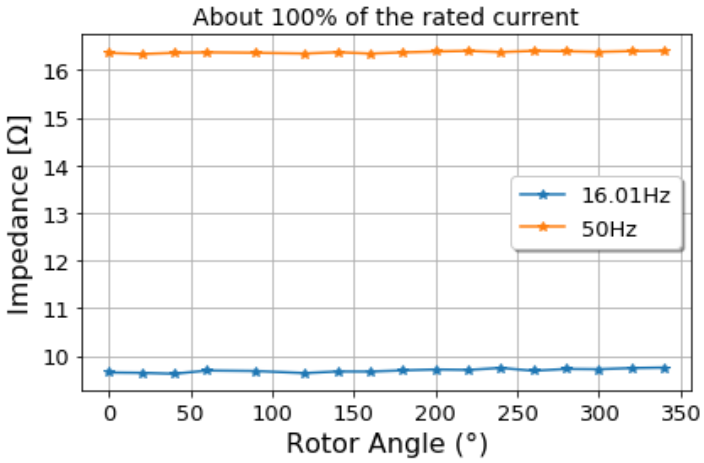

Fig. 8.3: SCIM3 substitute impedance under healthy rotor bar condition

It was observed that, the substitute impedance parameter under this condition is relatively constant at different rotor angle positions. Furthermore, the substitute impedance increases

from about 9.7 Ω at 16.01Hz to about 16.3 Ω at 50Hz. This shows that the substitute impedance is directly proportional to the supply frequency as expected.

8.3.2 Broken Rotor Bar Results

The results in Fig. 8.4 show the substitute impedance parameter's behaviour under the broken rotor bar fault condition as a function of the rotor angle at 16.01 Hz, 25 Hz, 35 Hz, 50 Hz and 75 Hz, respectively. The broken rotor bars' effect was observed on each of the substitute impedance yielding a sinusoidal profile or shape as against being constant when the rotor is healthy at different rotor angle positions. It is observed that the substitute impedance increases as the frequency increases as expected, and the sinusoidal profile at each of the frequencies is well conformed.

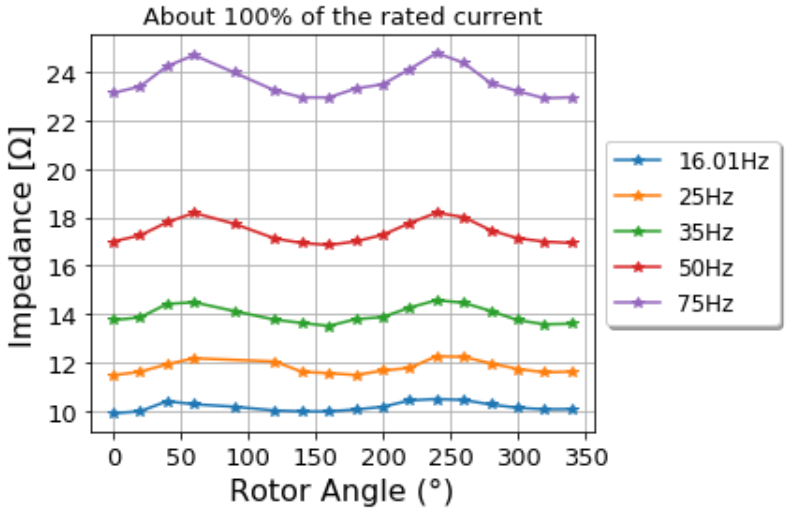

Fig. 8.4: SCIM3 substitute impedance under broken rotor bar fault condition

It was also observed that the sinusoidal profile is more evident at frequencies greater than 25 Hz. This is because the change in the substitute impedance increases in frequency, which is expected due to the eddy current produced by the flux that crosses the slot transversely from tooth to tooth through the conductor's body and tends to flow on the surface through the length of the core. Therefore, the excitation current of about 100% of the rated current (1.8A) at 50 Hz will be considered for further analysis.

Comparing the substitute impedance of the SCIM3 with a HRB and with a BRB, the behaviour of the substitute impedance of about 100% of the rated current at 50 Hz is shown in Fig. 8.5. As expected, the substitute impedance changes at different rotor angles due to the broken rotor bars' magnetic disturbances. This results in a sinusoidal profile of substitute impedance used as an indicator for diagnosing SCIM with broken rotor bars. From the plot, the substitute

impedance of the SCIM3 with a BRB has a maximum and minimum value of about 18.18 Ω and 16.85 Ω, respectively. The change in impedance is about 1.33 Ω. On the other hand, the substitute impedance of the SCIM3 with a HRB is relatively constant as expected. The change in the substitute impedance is about 0.03 Ω which is very small when compared with the change in the substitute impedance of the SCIM3 with a BRB. This could further be observed at 16.01 Hz at about 50%, and 100% of SCIM3 rated current, respectively as shown in Table 8.1. The slight variation of the change in the substitute impedance under the healthy rotor bar condition could be because of manufacturing imperfection.

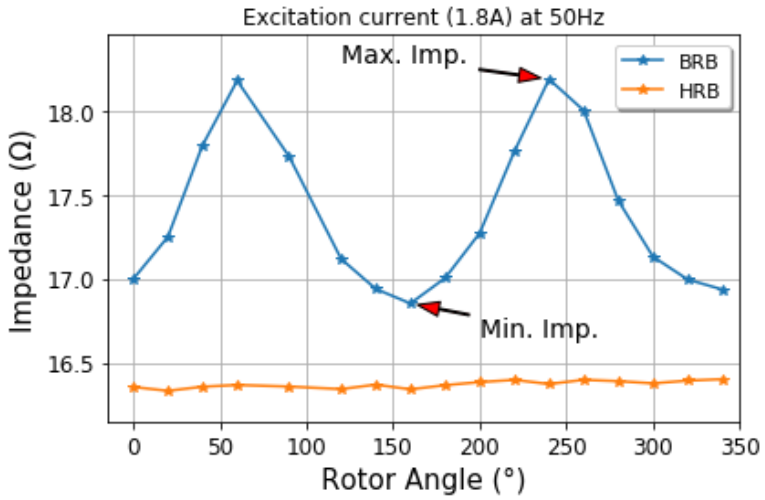

Fig. 8.5: SCIM3 substitute impedance under HRB and BRB at 50 Hz and about 1.8A

The change in the substitute impedance for the SCIM3 with a HRB and a BRB of about 50% and 100% of the rated current at 16.001 Hz and 50 Hz, respectively are shown in Table 8.1.

Table 8.1: Changes in the substitute impedance of the SCIM3 at 16.01 Hz and 50 Hz of different excitation currents.

Frequency	Excitation Current (A)	SCIM3 with HRB change in impedance (Ω)	SCIM3 with BRB change in impedance (Ω)
16.01 Hz	0.9	0.1363	0.5942
	1.8	0.1297	0.5922
50 Hz	0.9	0.1026	1.4691
	1.8	0.0386	1.3345

The results discussed above clearly indicate that a squirrel-cage induction motor with broken rotor bars could be detected using the sinusoidal profile of the substitute impedance as an indicator.

8.3.3 Effect of Current and Frequency on SCIM3 Substitute Impedance

The effect of the frequency and current on the change in the substitute impedance of the SCIM3 is investigated and compared from 16.01 Hz to 200 Hz at about 25% (0.45A), 50% (0.9A), and 100% (1.8A) of SCIM3 nominal current, respectively as shown in Fig. 8.6. It was observed that the change in substitute impedance value increases as the supply frequency increases as expected due to the skin effect, which tends to resist the flux penetration in the conductor. Comparing the results of the change in substituted impedance at a particular frequency across the excitation currents, variation in the change in substitute impedance is not as evident when compared at different frequencies.

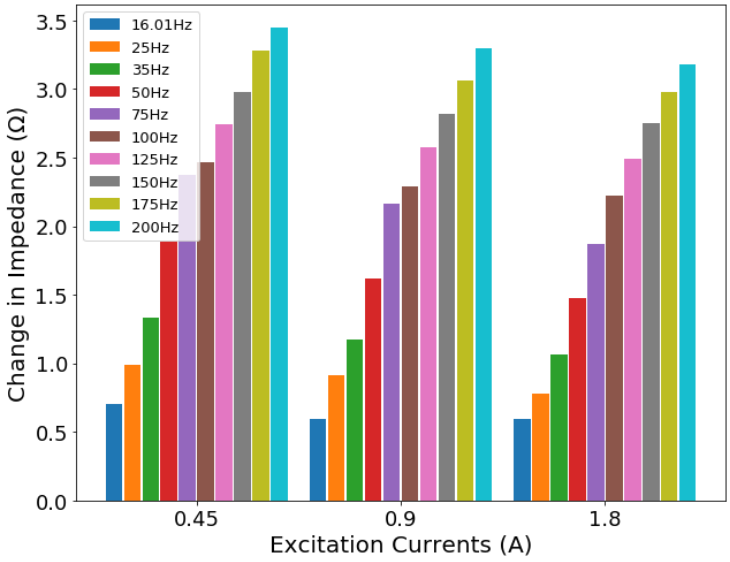

Fig. 8.6: SCIM3 change in substitute impedance at different currents and frequencies

8.4 Conclusion

The results of the impedance response and substitute impedance for SCIM3 with a healthy and broken rotor bar using SFRA and locked-rotor test respectively was presented. It is observed that it is much easier to observe the difference between the SCIM3 with a healthy and a broken rotor bar using the locked rotor-test procedure than the conventional SFRA. The substitute impedance at different supply frequencies and currents were also investigated. The substitute impedance was observed to be evident at higher frequencies due to skin effects which increases the change in the substitute impedance. The appearance of the sinusoidal profile for the substituted parameters indicates that a squirrel-cage induction motor rotor bar is faulty and concluded to be a viable technique for diagnosing squirrel-cage induction motor with broken rotor bars.

Chapter 9

Conclusions and Recommendations

9.1 Conclusions

The squirrel-cage induction motor is reviewed as the power horse mostly used in the industry for electromechanical energy conversion. Diagnostic techniques for squirrel-cage induction motor stator winding inter-turn and broken rotor bar faults have been investigated in this study.

The SFRA was reviewed and the impedance transfer function as one of the SFRA methods was investigated as a desired measurement technique able to provide useful insight towards inter-turn fault diagnosis in SCIMs. For assessing the stator winding condition using impedance frequency response transfer function measurement, the impedance peak magnitude and the frequency at the resonance point were selected as key features.

A silicon steel laminated core inductor was designed and modelled with an equivalent circuit to fully understand the impedance behaviour of a coil to enable a better representation of the stator winding model. The model showed acceptable performance when compared with the experimental result using the proposed methodology of the SFRA.

A distributed parameter model of induction motor stator winding was reduced to a lumped parameter model consisting of a single resistance, inductance, and capacitance. The simulated results agree with the experimental results in two out of the three regions of the stator winding's impedance behaviour. This model reduces simulation time and could be used as the impedance response baseline extraction of the SCIM stator winding during production.

The results of the proposed methodology for impedance transfer function measurement using SFRA applied to the DUT (LACOIN, SCIM1, SCIM2 with a rotor and without rotor) under different percentage level of severities shows that this technique is very sensitive, accurate and overcomes most of the downsides of the existing techniques mentioned in section 2.6. The assembly of the equipment is simple since the major measurand are voltage and current signals. The signals acquired only requires Fast Fourier Transform (FFT) to extract the frequency components for the evaluation of the impedance behaviour of the DUT. Unlike MCSA, vibration analysis and partial discharge which requires advanced signal processing or complex

pattern analysis to evaluate the IM's stator winding's health condition. Therefore, it has the potential to detect inter-turn short-circuit faults and useful for planning a maintenance schedule, thereby avoiding the extra cost associated with downtime and repair as against DC Hipot test.

SFRA was also used for investigations on the SCIM with a broken rotor bar fault. The results show that there is no clear distinction in the impedance response of SCIM under the healthy and broken rotor bar condition. This could be because of the low excitation current since the rotor bar's information is needed from the stator side using the impedance transfer function measurement. However, the rotor side is inaccessible. Hence, this cannot be used to diagnose SCIM with broken rotor bar fault. A different technique (locked-rotor test) was considered.

The locked-rotor test allows a higher current excitation of the SCIM up to the rated current. The substitute impedance measured from the stator side using a pulsating magnetic field by shorting two windings were extracted. It was expected that this parameter should change at different rotor angle positions since the presence of a broken rotor bar creates a magnetic disturbance around the bar which in turn alters this parameter. Analyses were conducted on this parameter to understand its behaviour as a function of the rotor angle position. It was observed that this parameter remains relatively constant when the rotor bar is healthy and forms a sinusoidal profile under the broken rotor bar condition. This sinusoidal profile is regarded as a key indicator of SCIM with a broken rotor bar fault. Also, the change in the substitute impedance of the SCIM3 under the broken rotor bar condition is much larger than its value under the healthy rotor bar condition. Therefore, the sinusoidal profile or shape formed at different rotor angles shows that a locked-rotor test using a pulsating magnetic field is a reliable technique for diagnosing squirrel-cage induction motor with broken rotor bar fault.

9.2 Recommendations

This work has developed a model for studying the impedance behaviour of the stator winding of a squirrel-cage induction motor. The number of stator winding turns was considered as the key factor in the proposed model to emulate the inter-turn short-circuit faults at different severities. The model could be improved by considering the insulation resistance and short-circuit resistance in the equivalent circuit to extend this work.

This work also investigated the detection of broken rotor bars using SFRA, where no clear indication of the impedance response at different rotor angles was observed. This approach could be improved upon to achieve a better result for broken rotor bar fault detection.

List of References

[1] F. J. T. E. Ferreira and A. T. De Almeida, “Overview on energy saving opportunities in electric motor driven systems - Part 1: System efficiency improvement,” *Conf. Rec. - Ind. Commer. Power Syst. Tech. Conf.*, vol. 2016-June, pp. 8–15, 2016, doi: 10.1109/ICPS.2016.7490219.

[2] P. Waide and C. U. Brunner, “Energy-Efficiency Policy Opportunities for Electric Motor-Driven Systems,” *Int. energy agency*, vol. na, no. na, p. 132, 2011, doi: 10.1787/5kgg52gb9gjd-en.

[3] M. Reliability, W. Group, P. Systems, R. Subcommittee, and E. Committee, “Report of Large Motor Reliability Survey of Industrial and Commercial Installations Parts II,” vol. I, no. February 1987, pp. 853–872, 2007.

[4] M. Kaufhold, H. Auinger, M. Berth, J. Speck, and M. Eberhardt, “Electrical Stress and Failure Mechanism of the Winding Insulation in PWM-Inverter-Fed Low-Voltage Induction Motors,” *IEEE Trans. Ind. Electron.*, vol. 47, no. 2, pp. 396–402, 2000, doi: 10.1109/41.836355.

[5] P. O. Donnell, C. Heising, C. Singh, and S. J. Wells, “Report of large motor reliability survey of industrial and commercial installations: part I,” *IEEE Trans. Ind. Appl.*, vol. IA-23, no. 1, pp. 153–158, 1987, doi: 10.1109/TIA.1987.4504880.

[6] A. J. C. Appiarius and D. K. Sharma, “Assessment of the reliability of motors in utility applications,” *IEEE Trans. Energy Convers.*, vol. 1, no. 1, pp. 39–46, 1986.

[7] K.-H. Kim, D.-U. Choi, B.-G. Gu, and I.-S. Jung, “Fault Model and Performance Evaluation of an Inverter-Fed Permanent Magnet Synchronous Motor under Winding Shorted Turn and Inverter Switch Open,” *IET Electr. Power Appl.*, vol. 4, no. 4, p. 214, 2010, doi: 10.1049/iet-epa.2009.0183.

[8] S. Zolfaghari, S. Noor, M. Rezazadeh Mehrjou, M. Marhaban, and N. Mariun, “Broken Rotor Bar Fault Detection and Classification Using Wavelet Packet Signature Analysis Based on Fourier Transform and Multi-Layer Perceptron Neural Network,” *Appl. Sci.*, vol. 8, no. 1, p. 25, Dec. 2017, doi: 10.3390/app8010025.

[9] H. Yaghobi *et al.*, “Motor current signature analysis to detect faults in induction motor

drives-fundamentals, Data interpretation, and industrial case histories," *IEEE Trans. Ind. Electron.*, 2017.

[10] P. Neti, M. R. Shah, K. Younsi, J. Krahn, J. Y. Zhou, and C. D. Whitefield, "Motor current signature analysis during accelerated life testing of form wound induction motors," *Proc. 2010 IEEE Int. Power Modul. High Volt. Conf. IPMHVC 2010*, pp. 106–109, 2010, doi: 10.1109/IPMHVC.2010.5958306.

[11] G. C. Stone, I. Culbert, E. A. Boulter, and H. Dhirani, *Electrical insulation for rotating machines: design, evaluation, aging, testing, and repairs*, Second. Hoboken, New Jersey: John Wiley & Sons, Inc., 2014.

[12] E.P. Dick and C. C. Erven, "Transformer diagnostic desting by frequency response analysis," *IEEE Trans. Power Appar. Syst.*, vol. PAS-97, no. 6, pp. 2144–2153, 1978, doi: 10.3362/9781780440484.010.

[13] P. Waide and C. U. Brunner, "Energy-efficiency policy opportunities for electric motor-driven systems," *Int. energy agency*, vol. na, no. na, p. 132, 2011, doi: 10.1787/5kgg52gb9gjd-en.

[14] A. Jacob, V. Jose, and D. Sebastian, "Stator fault detection in induction motor under unbalanced supply voltage," *2014 Annu. Int. Conf. Emerg. Res. Areas Magn. Mach. Drives, AICERA/iCMMD 2014 - Proc.*, 2014, doi: 10.1109/AICERA.2014.6908171.

[15] P. O. Donnell, C. Heising, C. Singh, and S. J. Wells, "Report of large motor reliability survey of industrial and commercial installations: part II," *IEEE Trans. Ind. Appl.*, vol. IA-23, no. 1, pp. 153–158, 1987, doi: 10.1109/TIA.1987.4504880.

[16] P. O. Donnell, C. Heising, C. Singh, and S. J. Wells, "Report of large motor reliability survey of industrial and commercial installations: part 3," *IEEE Trans. Ind. Appl.*, vol. IA-23, no. 1, pp. 153–158, 1987, doi: 10.1109/TIA.1987.4504880.

[17] R. K. Roy, A. Chatterjee, and D. Chatterjee, "A current signature based stator main winding fault detection technique for single-phase induction machine," *2016 2nd Int. Conf. Control. Instrumentation, Energy Commun. CIEC 2016*, pp. 284–288, 2016, doi: 10.1109/CIEC.2016.7513837.

[18] S. Karmakar, S. Chattopadhyay, M. Mitra, and S. Sengupta, *Induction Motor Fault Diagnosis: Approach through Current Signature Analysis*. 2003.

[19] K. Drobnič, M. Nemec, R. Fišer, and V. Ambrožič, “Influence of broken rotor bars on magnetic quantities in induction machine,” *Int. Conf. Compat. Power Electron. , CPE*, pp. 231–234, 2013, doi: 10.1109/CPE.2013.6601160.

[20] H. du Preez, “Induction Motor Rotor Bars,” 2006.

[21] N. Arthur and J. Penman, “Induction machine condition monitoring with higher order spectra,” *October*, vol. 47, no. 5, pp. 1031–1041, 2000.

[22] V. Climente-Alarcon, J. A. Antonino-Daviu, F. Vedreño-Santos, and R. Puche-Panadero, “Vibration transient detection of broken rotor bars by PSH sidebands,” *IEEE Trans. Ind. Appl.*, vol. 49, no. 6, pp. 2576–2582, 2013, doi: 10.1109/TIA.2013.2265872.

[23] J. Penman, H. . Sedding, and ., “Detection and location of interturn short circuits in the stator winding of operating motors,” *IEEE Trans. Energy Convers.*, vol. 9, no. 4, pp. 652–658, 1994.

[24] T. Assaf, H. Henao, and G. A. Capolino, “Simplified axial flux spectrum method to detect incipient stator inter-turn short-circuits in induction machine,” *IEEE Int. Symp. Ind. Electron.*, vol. 2, pp. 815–819, 2004, doi: 10.1109/ISIE.2004.1571918.

[25] S. W. Clark and D. Stevens, “Induction motor rotor bar damage evaluation with magnetic field analysis,” *IEEE Trans. Ind. Appl.*, vol. 52, no. 2, pp. 1469–1476, 2016, doi: 10.1109/TIA.2015.2508424.

[26] H. Henao, C. Demian, and G. A. Capolino, “A frequency-domain detection of stator winding faults in induction machines using an external flux sensor,” *IEEE Trans. Ind. Appl.*, vol. 39, no. 5, pp. 1272–1279, 2003, doi: 10.1109/TIA.2003.816531.

[27] M. Y. Chow, S. O. Yee, and P. M. Mangum, “A neural network npproach to real-time nondition monitoring of induction motors,” *IEEE Trans. Ind. Electron.*, vol. 38, no. 6, pp. 448–453, 1991, doi: 10.1109/41.107100.

[28] F. Filippetti, G. Franceschini, and C. Tassoni, “Neural networks aided on-line diagnostics of induction motor rotor faults,” *IEEE Trans. Ind. Appl.*, vol. 31, no. 4, pp. 892–899, 1995, doi: 10.1109/28.395301.

[29] S. Choi, E. Pazouki, J. Baek, and H. R. Bahrami, “Iterative condition monitoring and fault diagnosis scheme of electric motor for harsh industrial application,” *IEEE Trans. Ind. Electron.*, vol. 62, no. 3, pp. 1760–1769, 2015, doi: 10.1109/TIE.2014.2361112.

[30] A. J. Marques Cardoso, S. M. A. Cruz, and D. S. B. Fonseca, “Inter-turn stator winding fault diagnosis in three-phase induction motors, by Park’s vector approach,” *IEEE Trans. Energy Convers.*, vol. 14, no. 3, pp. 595–598, 1999, doi: 10.1109/60.790920.

[31] F. Ciancetta, A. Del Pizzo, C. Olivieri, N. Rotondale, L. Castellini, and M. D’Andrea, “SFRA technique applied to fault diagnosis on stators of electric motors,” *2014 Int. Symp. Power Electron. Electr. Drives, Autom. Motion, SPEEDAM 2014*, pp. 515–520, 2014, doi: 10.1109/SPEEDAM.2014.6871937.

[32] G. Bucci, F. Ciancetta, and E. Fiorucci, “Apparatus for online continuous diagnosis of induction motors based on the SFRA technique,” *IEEE Trans. Instrum. Meas.*, vol. 69, no. 7, pp. 4134–4144, 2020, doi: 10.1109/TIM.2019.2942172.

[33] R. Khalilisenobari and J. Sadeh, “A novel numerical index for assessing results of frequency response analysis (FRA): an experimental study on electrical machines,” *52nd North Am. Power Symp.*, 2021.

[34] F. Kreith, *The CRC Handbook of Mechanical Engineering*, vol. 125, no. 18. 6000 Broken Sound Parkway NW, Suite 300 Boca Raton: Taylor & Francis Group, 2005.

[35] P. C. Sen, *Principles of Electric Machines and Power Electronics*, 3rd ed. John Wiley & Sons, Inc., 2014.

[36] A. Ivanov-Smolensky, *Electrical Machines*, vol. 2, no. 2019.

[37] Electrical4u, “Construction of three phase induction motor,” *www.Electrical4U.Com*, 2020. .

[38] J. F. Gieras, *Electrical Machines: Fundamentals of Electromechanical Energy Conversion*. 6000 Broken Sound Parkway NW, Suite 300 Boca Raton: Taylor & Francis Group, LLC, 2017.

[39] W. Tong, *Mechanical design of electric motors*, vol. 53, no. 9. 6000 Broken Sound Parkway NW, Suite 300 Boca Raton: CRC Press, Taylor & Francis Group, 2013.

[40] S. N. Vukosavic, *Electrical machines*. New York Heidelberg Dordrecht London: Springer, 2013.

[41] J. Pyrhonen, V. Hrabovcova, and R. S. Semken, *Electrical Machine Drives Control: An Introduction*. John Wiley & Sons, Ltd, 2016.

[42] D. Fink and H. Beaty, *Standard Handbook for Electrical Engineers*. McFraw-Hill, 2006.

[43] M. Drif and A. J. M. Cardoso, "Stator fault diagnostics in squirrel cage three-phase induction motor drives using the instantaneous active and reactive power signature analyses," *IEEE Trans. Ind. Informatics*, vol. 10, no. 2, pp. 1348–1360, 2014, doi: 10.1109/TII.2014.2307013.

[44] A. H. Bonnett and G. C. Soukup, "Cause and analysis of stator and rotor failures in three-phase squirrel-cage induction motors," *IEEE Trans. Ind. Appl.*, vol. 28, no. 4, pp. 921–937, 1992, doi: 10.1109/28.148460.

[45] P. Zhang, Y. Du, T. G. Habetler, and B. Lu, "A survey of condition monitoring and protection methods for medium-voltage induction motors," *IEEE Trans. Ind. Appl.*, vol. 47, no. 1, pp. 34–46, 2011, doi: 10.1109/TIA.2010.2090839.

[46] S. Kumar *et al.*, "A comprehensive review of condition based prognostic maintenance for induction motor," *IEEE Access*, vol. 7, pp. 90690–90704, 2019, doi: 10.1109/ACCESS.2019.2926527.

[47] N. Klingerman, D. Finney, S. Samineni, N. Fischer, and D. Haas, "Understanding generator stator ground faults and their protection schemes," *69th Annu. Conf. Prot. Relay Eng. CPRE 2016*, 2017, doi: 10.1109/CPRE.2016.7914921.

[48] S. Nandi, H. A. Toliyat, and X. Li, "Condition monitoring and fault diagnosis of electrical motors - A review," *IEEE Trans. Energy Convers.*, vol. 20, no. 4, pp. 719–729, 2005, doi: 10.1109/TEC.2005.847955.

[49] A. Bentounsi, A. Lebaroud, A. Khezzar, and M. Boucherma, "Analysis of broken bars effects under asymmetrical and distorted induction motor current," no. September, 2004.

[50] M. Nemec, K. Drobnic, R. Fiser, and V. Ambrozic, "Simplified model of induction machine with broken rotor bars," *Proc. - 2016 IEEE Int. Power Electron. Motion Control Conf. PEMC 2016*, pp. 1085–1090, 2016, doi: 10.1109/EPEPEMC.2016.7752145.

[51] S. Kumar *et al.*, "A comprehensive review of condition based prognostic maintenance (CBPM) for induction motor," *IEEE Access*, vol. 7, pp. 90690–90704, 2019, doi: 10.1109/ACCESS.2019.2926527.

[52] R. M. Tallam, T. G. Habetler, and R. G. Harley, "Experimental testing of a neural-

network-based turn-fault detection scheme for induction machines under accelerated insulation failure conditions," *IEEE Int. Symp. Diagnostics Electr. Mach. Power Electron. Drives, SDEMPED 2003 - Proc.*, pp. 58–62, 2003, doi: 10.1109/DEMPED.2003.1234547.

[53] X. Boqiang, L. Heming, and S. Liling, "Feature signal extraction of inter-turn short circuit fault in stator winding of induction machine," *IEEE Int. Conf. Ind. Technol.*, pp. 97–100, 2002.

[54] K. Toni, M. Slobodan, and B. Aleksandar, "Detection of turn to turn faults in stator winding with axial magnetic flux in induction motors," *Proc. IEEE Int. Electr. Mach. Drives Conf. IEMDC 2007*, vol. 1, pp. 826–829, 2007, doi: 10.1109/IEMDC.2007.382775.

[55] S. Williamson and K. Mirzoian, "Analysis of cage induction motors with stator winding faults," *IEEE Power Eng. Rev.*, vol. PER-5, no. 7, pp. 50–51, 1985, doi: 10.1109/MPER.1985.5528481.

[56] J. Sottile, F. C. Trutt, and J. L. Kohler, "Condition monitoring of stator windings in induction motors: Part II - Experimental investigation of voltage mismatch detectors," *IEEE Trans. Ind. Appl.*, vol. 38, no. 5, pp. 1454–1459, 2002, doi: 10.1109/TIA.2002.802921.

[57] S. Bin Lee, R. M. Tallam, and T. G. Habetler, "A robust, on-line turn-fault detection technique for induction machines based on monitoring the sequence component impedance matrix," *IEEE Trans. Power Electron.*, vol. 18, no. 3, pp. 865–872, 2003, doi: 10.1109/TPEL.2003.810848.

[58] M. Eftekhari, M. Moallem, S. Sadri, and M. F. Hsieh, "Online detection of induction motor's stator winding short-circuit faults," *IEEE Syst. J.*, vol. 8, no. 4, pp. 1272–1282, 2014, doi: 10.1109/JSYST.2013.2288172.

[59] S. Bindu and V. T. Vinod, "Diagnoses of internal faults of three phase squirrel cage induction motor - a review," *Int. Conf. Adv. Energy Convers. Technol.*, pp. 48–54, 2014.

[60] I. Ishkova and O. Vitek, "Diagnosis of eccentricity and broken rotor bar related faults of induction motor by means of motor current signature analysis," *Proc. 2015 16th Int. Sci. Conf. Electr. Power Eng. EPE 2015*, pp. 682–686, 2015, doi:

10.1109/EPE.2015.7161130.

[61] I. P. Engineering, O. Conference, and T. Jewel, “Detection and classification of induction motor faults using motor current signature analysis and multilayer perceptron,” *Proc. 2014 IEEE 8th Int. Power Eng. Optim. Conf. PEOCO 2014*, no. March, pp. 35–40, 2014, doi: 10.1109/PEOCO.2014.6814395.

[62] W. T. Thomson and M. Fenger, “Current signature analysis to detect induction motor faults,” *IEEE Ind. Appl. Mag.*, no. August, 2001.

[63] P. S. Barendse, B. Herndler, M. A. Khan, and P. Pillay, “The application of wavelets for the detection of inter-turn faults in induction machines,” *2009 IEEE Int. Electr. Mach. Drives Conf. IEMDC ’09*, pp. 1401–1407, 2009, doi: 10.1109/IEMDC.2009.5075386.

[64] S. M. K. Zaman, H. U. M. Marma, and X. Liang, “Broken rotor bar fault diagnosis for induction motors uusing power spectral density and complex continuous wavelet transform methods,” *2019 IEEE Can. Conf. Electr. Comput. Eng. CCECE 2019*, pp. 16–19, 2019, doi: 10.1109/CCECE.2019.8861517.

[65] J. Pons-llinares *et al.*, “Advance induction motor rotor fault diagnosis via continuous and discrete Time – frequency tools,” *IEEE Trans. Ind. Electron.*, vol. 62, no. 3, pp. 1791–1802, 2015.

[66] S. Das, P. Purkait, D. Dey, and S. Chakravorti, “Monitoring of inter-turn insulation failure in induction motor using advanced signal and data processing tools,” *IEEE Trans. Dielectr. Electr. Insul.*, vol. 18, no. 5, pp. 1599–1608, 2011, doi: 10.1109/TDEI.2011.6032830.

[67] W. G. Zanardelli, E. G. Strangas, and S. Aviyente, “Identification of intermittent electrical and mechanical faults in permanent-magnet AC drives based on time-frequency analysis,” *IEEE Trans. Ind. Appl.*, vol. 43, no. 4, pp. 971–980, 2007, doi: 10.1109/TIA.2007.900446.

[68] E. G. Strangas, S. Aviyente, and S. S. H. Zaidi, “Time-frequency analysis for efficient fault diagnosis and failure prognosis for interior permanent-magnet AC motors,” *IEEE Trans. Ind. Electron.*, vol. 55, no. 12, pp. 4191–4199, 2008, doi: 10.1109/TIE.2008.2007529.

[69] S. Jokic, N. Cincar, and B. Novakovic, “The analysis of vibration measurement and

current signature in motor drive faults detection," *2018 17th Int. Symp. INFOTEH-JAHORINA, INFOTEH 2018 - Proc.*, vol. 2018-Janua, no. March, pp. 1–6, 2018, doi: 10.1109/INFOTEH.2018.8345531.

[70] A. Glowacz, "Acoustic-based fault diagnosis of commutator motor," *Electron.*, vol. 7, no. 11, 2018, doi: 10.3390/electronics7110299.

[71] A. Glowacz, "Acoustic based fault diagnosis of three-phase induction motor," *Appl. Acoust.*, vol. 137, no. February, pp. 82–89, 2018, doi: 10.1016/j.apacoust.2018.03.010.

[72] F. Guastavino, F. Porcile, A. Ratto, D. Cordano, and G. Secondo, "Electrical aging test and repetitive partial discharge inception voltage on random wire wound winding insulation," *2014 IEEE Conf. Electr. Insul. Dielectr. Phenomena, CEIDP 2014*, pp. 510–513, 2014, doi: 10.1109/CEIDP.2014.6995806.

[73] IEEE Power and Energy Society, *IEEE Std C57.149-2012, guide for the application and interpretation of frequency response analysis for Oil-immersed transformers*, no. March. 2013.

[74] P. Picher, "Mechanical condition assessment of transformer windings using frequency response analysis (fra)," *CIGRE*, no. April, pp. 30–34, 2008.

[75] F. R. Blanquez, C. A. Platero, E. Rebollo, and F. Blanquez, "Evaluation of the applicability of fra for inter-turn fault detection in stator windings," *Proc. - 2013 9th IEEE Int. Symp. Diagnostics Electr. Mach. Power Electron. Drives, SDEMPED 2013*, pp. 177–182, 2013, doi: 10.1109/DEMPED.2013.6645714.

[76] P. Shi, Z. Chen, Y. Vagapov, A. Davydova, and S. Lupin, "Broken bar fault diagnosis for induction machines under load variation condition using discrete wavelet transform," *Proc. IEEE East-West Des. Test Symp. EWDTS 2014*, 2014, doi: 10.1109/EWDTS.2014.7027059.

[77] D. G. Jerkan, D. D. Reljic, and D. P. Marcetic, "Broken rotor bar fault detection of IM based on the counter-current braking method," *IEEE Trans. Energy Convers.*, vol. 32, no. 4, pp. 1356–1366, 2017, doi: 10.1109/TEC.2017.2696578.

[78] A. Bellini, F. Filippetti, G. Franceschini, C. Tassoni, and G. B. Kliman, "Quantitative evaluation of induction motor broken bars by means of electrical signature analysis," *IEEE Trans. Ind. Appl.*, vol. 37, no. 5, pp. 1248–1255, 2001, doi: 10.1109/28.952499.

[79] D. Morinigo-Sotelo, R. D. J. Romero-Troncoso, P. A. Panagiotou, J. A. Antonino-Daviu, and K. N. Gyftakis, “Reliable detection of rotor bars breakage in induction motors via MUSIC and ZSC,” *IEEE Trans. Ind. Appl.*, vol. 54, no. 2, pp. 1224–1234, 2018, doi: 10.1109/TIA.2017.2764846.

[80] M. Nemec, V. Ambrožič, R. Fišer, and D. Makuc, “Parameters Estimation using Single Phase Measurement of Three Phase Induction Machine,” *Prz. Elektrotechniczny*, vol. 87, no. 3, pp. 129–132, 2011.

[81] M. Nemec, D. Makuc, V. Ambrožič, and R. Fišer, “Simplified model of induction machine with electrical rotor asymmetry,” *19th Int. Conf. Electr. Mach. ICEM 2010*, pp. 2–7, 2010, doi: 10.1109/ICELMACH.2010.5608048.

[82] D. Makuc, K. Drobnič, V. Ambrožič, D. Miljavec, R. Fišer, and M. Nemec, “Estimation of parameters of induction motor with broken rotor bars,” *2011 7th Int. Conf. Compat. Power Electron. CPE 2011 - Conf. Proc.*, pp. 246–251, 2011, doi: 10.1109/CPE.2011.5942240.

[83] R. Fiser, K. Drobnic, H. Lavric, M. Nemec, V. Ambrozic, and D. Makuc, “Induction motor parameters in case of rotor electrical asymmetry,” *Proc. - 2013 IEEE Work. Electr. Mach. Des. Control Diagnosis, WEMDCD 2013*, pp. 271–278, 2013, doi: 10.1109/WEMDCD.2013.6525186.

[84] R. K. Bhatnagar and A. K. Mukherjee, “Mecahnical integrity checking of generator stator overhang by natural frequency measurement,” *Iris Rotating Mach. Conf.*, no. June, pp. 1–5, 2007.

[85] G. Stojcic and T. M. Wolbank, “Detection of defects in stator winding of inverter fed induction machines,” *Proc. 2013 IEEE Int. Electr. Mach. Drives Conf. IEMDC 2013*, pp. 111–116, 2013, doi: 10.1109/IEMDC.2013.6556241.

[86] S. Alsuhaibani, Y. Khan, A. Beroual, and N. H. Malik, “A review of frequency response analysis methods for power transformer diagnostics,” *Energies*, vol. 9, no. 11, 2016, doi: 10.3390/en9110879.

[87] M. Bagheri, M. Lu, M. S. Naderi, and B. T. Phung, “Transformer frequency response: A new technique to analyze and distinguish the low-frequency band in the frequency response analysis spectrum,” *IEEE Electr. Insul. Mag.*, vol. 34, no. 5, pp. 39–49, 2018,

doi: 10.1109/MEI.2018.8445433.

[88] H. Rahimpour, S. Mitchell, and J. Tusek, “The application of sweep frequency response analysis for the online monitoring of power transformers,” *Proc. 2016 Australas. Univ. Power Eng. Conf. AUPEC 2016*, pp. 11–16, 2016, doi: 10.1109/AUPEC.2016.07749347.

[89] F. R. Blanquez, C. A. Platero, E. Rebollo, and F. Blanquez, “Evaluation of the applicability of FRA for inter-turn fault detection in stator windings,” *Proc. - 2013 9th IEEE Int. Symp. Diagnostics Electr. Mach. Power Electron. Drives, SDEMPED 2013*, pp. 177–182, 2013, doi: 10.1109/DEMPED.2013.6645714.

[90] V. Behjat, A. Vahedi, A. Setayeshmehr, H. Borsi, and E. Gockenbach, “Sweep frequency response analysis for diagnosis of Low level short circuit faults on the windings of power transformers: an experimental study,” *Int. J. Electr. Power Energy Syst.*, vol. 42, no. 1, pp. 78–90, 2012, doi: 10.1016/j.ijepes.2012.03.004.

[91] R. C. Dorf, *Circuits, Signals, and Speech and Image Processing*, Third. 6000 Broken Sound Parkway NW, Suite 300 Boca Raton: Taylor & Francis Group, 2006.

[92] M. Brandt and M. Gutten, “Diagnostic of Induction Motor Using SFRA Method,” *2016 Conf. Diagnostics Electr. Eng.*, pp. 1–4, doi: 10.1109/DIAGNOSTIKA.2016.7736474.

[93] S. Tenbohlen and S. Ryder, “Making frequency response analysis measurements: a comparison of the swept frequency and low voltage impulse methods,” *XIII th Int. Symp. high Volt. Eng.*, pp. 1–4, 2003.

[94] K. Patel, N. Das, A. A., and S. Islam, “Power transformer winding fault analysis,” *Autralasian Univ. Power Eng. Conf.*, no. October, pp. 3–5, 2013.

[95] K. Ogata, *Modern Control Engineering*, Fifth. One Lake street, Upper Saddle River, New Jersey: Pearson Education, Inc., 2010.

[96] K. Patel, N. Das, A. Abu-Siada, and S. Islam, “Power transformer winding fault analysis using transfer function,” *2013 Australas. Univ. Power Eng. Conf. AUPEC 2013*, no. October, pp. 3–5, 2013, doi: 10.1109/aupec.2013.6725438.

[97] J. A. S. B. Jayasinghe, Z. D. Wang, P. N. Jarman, and A. W. Darwin, “Winding movement in power transformers: a comparison of FRA measurement connection methods,” *IEEE Trans. Dielectr. Electr. Insul.*, vol. 13, no. 6, pp. 1342–1349, 2006, doi:

10.1109/TDEI.2006.258206.

[98] F. Marek and F. Jakub, “Detection of transformer winding deformations based on the transfer function—measurements and simulations,” *Meas. Sci. Technol.*, vol. 14, no. 11, p. 1986, 2003, [Online]. Available: http://stacks.iop.org/0957-0233/14/i=11/a=017.

[99] S. A. Ryder, “Diagnosing transformer faults using frequency response analysis,” *IEEE Electr. Insul. Mag.*, vol. 19, no. 2, pp. 16–22, 2003, doi: 10.1109/MEI.2003.1192032.

[100] M. H. Samimi, S. Tenbohlen, A. A. S. Akmal, and H. Mohseni, “Evaluation of numerical indices for the assessment of transformer frequency response,” *IET Gener. Transm. Distrib.*, vol. 11, no. 1, pp. 218–227, 2017, doi: 10.1049/iet-gtd.2016.0879.

[101] V. Behjat and M. Mahvi, “Statistical approach for interpretation of power transformers frequency response analysis results,” *IET Sci. Meas. Technol.*, vol. 9, no. 3, pp. 367–375, 2015, doi: 10.1049/iet-smt.2014.0097.

[102] G. D. Bergland, “A guided tour of the fast Fourier Transform,” *IEEE Spectr.*, vol. 6, no. 7, pp. 41–52, 1969, doi: 10.1109/MSPEC.1969.5213896.

[103] E. O. Brigham, *The Fast Fourier Transform and its Applications*, vol. 27, no. 3. Englewood Cliffs, New Jersey: Prentice-Hall, Inc., 1990.

[104] J. W. Tukey and J. W. Cooley, “An algorithm for the machine calculation of complex fourier Series,” *Math. Comput.*, vol. 19, no. 90, pp. 297–301, 1965.

[105] K. Iizuka, “The fast fourier transform (FFT),” *Springer Ser. Opt. Sci.*, vol. 35, pp. 161–179, 2008, doi: 10.1007/978-0-387-75724-7_7.

[106] Y. Li, L. Wang, Q. Yang, J. Zhu, and C. Zhang, “Comprehensive magnetic properties measurement of the laminated silicon steel by 3-D magnetic tester,” *Int. J. Appl. Electromagn. Mech.*, vol. 55, no. S1, pp. S177–S191, 2017, doi: 10.3233/JAE-172272.

[107] P. L. Dowell, “Effects of eddy currents in transformer windings,” *Proc. Inst. Electr. Eng.*, vol. 113, no. 8, p. 1387, 1966, doi: 10.1049/piee.1966.0236.

[108] C. Boniface and P. Barendse, “Impedance behavioural study of silicon steel laminated core inductor,” 2020, doi: 10.1109/SAUPEC/RobMech/PRASA48453.2020.9041022.

[109] C. P. Yue and S. S. Wong, “Design strategy of on-chip inductors for highly integrated RF systems,” *Proc. - Des. Autom. Conf.*, pp. 982–987, 1999.

[110] A. M. Urling, G. R. Skuttt, and T. G. Wilson, “Characterizing high-frequency effects in transformer windings-a guide to several significant articles,” *Current*, pp. 373–385, 1989.

[111] C. McLyman, *“Transformer and Inductor Design Handbook,”* Fourth Edi. NewYork: Taylor & Francis Group, 2011.

[112] G. Grandi, M. K. Kazimierczuk, A. Massarini, U. Reggiani, and G. Sancineto, “Model of laminated iron-core inductors for high frequencies,” *IEEE Trans. Magn.*, vol. 40, no. 4 I, pp. 1839–1845, 2004, doi: 10.1109/TMAG.2004.830508.

[113] M.P. Perry, “Multiple layer series connected winding design for minimum losses,” *Trial*, no. l, pp. 116–123, 1979.

[114] E. Bennett and S. C. Larson, “Effective resistance to alternating currents of multilayer windings,” *Electr. Eng.*, vol. 59, no. 12, pp. 1010–1016, 2013, doi: 10.1109/ee.1940.6435274.

[115] M. S. Naderi, M. Vakilian, T. R. Blackburn, B. T. Phung, M. S. Naderi, and A. Nasiri, “A hybrid transformer model for determination of partial discharge location in transformer winding,” *IEEE Trans. Dielectr. Electr. Insul.*, vol. 14, no. 2, pp. 436–443, 2007, doi: 10.1109/TDEI.2007.344625.

[116] Paul R.Clayton, *Introduction to Electromagnetic Compatibility*, Second Edi. Hoboken, New Jersey: JOHN WILEY & SONS, INC., 2006.

[117] M. K. Kazimierczuk, G. Sancineto, G. Grandi, U. Reggiani, and A. Massarini, “High-Frequency Small-Signal Model,” *IEEE Trans. Magn.*, vol. 35, no. 5, pp. 4185–4191, 1999.

[118] A. M. Bartoli and M. K. Kazimierczuk, “Modeling Iron-Powder Inductors at High Frequencies,” *IEEE*, vol. 480, pp. 1225–1232, 1995.

[119] L. Dalessandro, F. da Silveira Cavalcante, and J. W. Kolar, “Self-capacitance of high-voltage transformers,” *IEEE Trans. Power Electron.*, vol. 22, no. 5, pp. 2081–2092, 2007, doi: 10.1109/TPEL.2007.904252.

[120] A. Massarini and M. K. Kazimierczuk, “Self-capacitance of inductors,” *IEEE Trans. Power Electron.*, vol. 12, no. 4, pp. 671–676, 1997, doi: 10.1109/63.602562.

[121] Marian K. Kazimierczuk, *"High Frequency Magnetic Components,"* Second Edi., vol. 111, no. 479. United Kingdom: John Wiley & Sons, Ltd, 1965.

[122] A. Massarini, M. K. Kazimierczuk, and G. Grandi, "Lumped parameter models for single- and multiple-layer inductors," *PESC Rec. - IEEE Annu. Power Electron. Spec. Conf.*, vol. 1, pp. 295–301, 1996.

[123] J. A. Martinez-Velasco, *Power System Transients: Parameter Determination*. 6000 Broken Sound Parkway NW, Suite 300 Boca Raton: Taylor $ Francis Group, LLC, 2010.

[124] C. Q. Su, *Electromagnetic Transients in Transformer and Rotating Machine Windings*, 1st ed. USA: Information Science Reference (an imprint of IGI Global), 2012.

[125] R. G. Rhudy, E. L. Owen, and D. K. Sharma, "Voltage distribution among the coils and turns of a form wound AC rotating machine exposed to impulsed voltage," *IEEE Trans. Energy Convers.*, vol. EC-1, no. 2, pp. 50–60, 1986.

[126] J. Pyrhönen, T. Jokinen, and V. Hrabovcová, *Design of Rotating Electrical Machines*. The Atrium, Southern Gate, Chichester, West Sussex, PO19 8SQ, United Kingdom: John Wiley & Sons, Ltd, 2008.

[127] A. B. Field, "Eddy currents in large slot-wound conductors," *Trans. Am. Inst. Electr. Eng.*, vol. 24, pp. 761–768, 1905.

[128] I. Boldea and A. N. Syed, *The Induction Machines Design Handbook*, Second Edi. 6000 Broken Sound Parkway NW, Suite 300 Boca Raton: Taylor and Francis Group, 2010.

[129] J. Pyrhonen, J. Tapani, and V. Hrabovcová, *Design of rotating electrical machines*, 2nd ed. John Wiley & Sons, Ltd, 2014.

[130] L. Stoyanov, V. Lazarov, Z. Zarkov, and E. Popov, "Influence of skin effect on stator windings resistance of AC machines for electric drives," *2019 16th Conf. Electr. Mach. Drives Power Syst. ELMA 2019 - Proc.*, no. June, pp. 6–8, 2019, doi: 10.1109/ELMA.2019.8771551.

[131] D. C. Hanselman and W. H. Peake, "Eddy-current effects in slot-bound conductors," *IEE Proc. B Electr. Power Appl.*, vol. 142, no. 2, pp. 131–136, 1995.

[132] T. A. Lipo, *Analysis of Synchronous Machines*, 2nd ed. Taylor and Francis Group, LLC, 2017.

[133] J. Pyrhönen, T. Jokinen, and V. Hrabovcová, *"Design of Rotating Electrical Machines."* 2008.

[134] Clayton R. Paul, *Inductance: Loop and Partial*. Hoboken, New Jersey: John Wily & Sons, Inc, 2010.

[135] H. K. Yun, Y. C. Kim, C. Y. Won, Y. R. Kim, Y. S. Kim, and S. W. Choi, "A Study on Inverter and Motor Winding for Conducted EMI Prediction," 2001, doi: 10.1109/isie.2001.931561.

[136] N. B. Chagas and T. B. Marchesan, "Methodology for calculating the value of static capacitance between conductors of circular cross-section," *14th Brazilian Power Electron. Conf. COBEP 2017*, vol. 2018-Janua, pp. 1–5, 2017, doi: 10.1109/COBEP.2017.8257289.

[137] X. Liu, Y. Wang, J. Zhu, Y. Guo, G. Lei, and C. Liu, "Calculation of capacitance in high-frequency transformer windings," *IEEE Trans. Magn.*, vol. 52, no. 7, pp. 18–21, 2016, doi: 10.1109/TMAG.2016.2522976.

[138] B. Ehsani, *Data Acquisition using LabVIEW*, vol. 53, no. 9. Birmingham, UK: Packt Publishing Ltd., 2016.

[139] National Instrument, *LabVIEW Basics I - Introduction Course Manual*. 2008.

[140] V. Nurmanova, Y. Akhmetov, M. Bagheri, A. Zollanvari, G. B. Gharehpetian, and T. Phung, "A new transformer FRA test setup for advanced interpretation and winding short-circuit prediction," *Proc. - 2020 IEEE Int. Conf. Environ. Electr. Eng. 2020 IEEE Ind. Commer. Power Syst. Eur. EEEIC / I CPS Eur. 2020*, 2020, doi: 10.1109/EEEIC/ICPSEurope49358.2020.9160545.

[141] R. Khalili Senobari, J. Sadeh, and H. Borsi, "Frequency response analysis (FRA) of transformers as a tool for fault detection and location: A review," *Electr. Power Syst. Res.*, vol. 155, pp. 172–183, 2018, doi: 10.1016/j.epsr.2017.10.014.

[142] J. Christian and K. Feser, "Procedures for detecting winding displacements in power transformers by the transfer function method," *IEEE Trans. Power Deliv.*, vol. 19, no. 1, pp. 214–220, 2004, doi: 10.1109/TPWRD.2003.820221.

Appendix A

A.1 Frequency Response Analysis Test Configurations

There are four different configurations normally used for making FRA measurements. These are: end to end open circuit test; end to end short-circuit test; capacitive inter-winding test and inductive inter-winding test.

A.1.1 End to End Open Circuit Test

This mode of test configuration is the most common FRA test performed [140]. The input signal is connected to one end of the winding while the output signal is measured from the other end of the winding. This can be applied to both single and three-phase induction motor and applies to wye and delta connected windings. The term open circuit indicates that the winding of the other phases is left floating during the measurement. This test is most influenced by the effect of the core and main windings. Depending on the winding configuration, the low frequency section will usually take on a distinct shape.

A.1.2 End to End Short-Circuit Test

This mode of test configuration is made from one end of a winding to another while the other winding is shorted. Voltages with reference to ground are measured at each end of the excited winding. This connection removes the influence of magnetizing inductance of the core from the response and allows inspection of the winding without the influence of the core. Due to the absence of the core, the response in the low frequency region is characterized by only leakage the inductance of the winding.

A.1.3 Capacitive Inter-Winding Test

The capacitive inter-winding test also known as the inter-winding measurement is performed between two electrically isolated windings. This is made from one end of a winding and the response signal is measured through one of the terminals of another winding, with all other terminals floating. Capacitive inter-winding measurements are capacitive in nature and exhibit a high impedance at low frequencies (< 100 Hz) which generally decreases as frequency increases.

A.1.4 Inductive Inter-Winding Test

The inductive inter-winding test (also known as the transfer voltage measurement) is performed between two windings with one end of each winding grounded while other winding terminals

not under test remains floating. This mode of test configuration closely resembles the turns ratio test properties at or around the fundamental power frequency.

A.2 Methods Used to Assess Measured Traces

Evaluation of FRA results require comparison of both actual data with reference data by visual inspection or using processed data [74]. There are three methods used to assess the measured traces: time-based comparison, type-based comparison and phase-based comparison which are discussed below.

A.2.1 Time-based comparison

In this mode of assessing the stator winding integrity of induction motor, the reference or baseline data is the result of a former FRA test when it is in good condition and is called fingerprint or signature of the induction motor. This can be gotten from the factory along with the induction motor when purchased or performed immediately after installation. This method is the most reliable way for evaluating or assessing FRA measurements. In a situation where this is not available, the type- and phase-based comparison are the alternative.

A.2.2 Type-based comparison

The FRA results of the identically designed, manufactured and constructed induction motor can be used for evaluating the actual test responses when the fingerprint data are not available [141]. These similar motors are sometimes referred to as twin or sister induction motors. There might be a slight deviation in the results due to manufacturing tolerance or core magnetization effects [142]. This method is particularly useful for single-phase induction motor. In a situation where the twin induction motor is not available, phase comparison is applied to test the integrity of the stator winding of a three-phase squirrel-cage induction motor.

A.2.3 Phase-based comparison

In this mode of assessing the induction motor, the FRA test results of the other phases of a three-phase winding could be used as reference data due to symmetry in the construction.

A.3 Application of FRA Measurement

There are two distinct categories for the application of FRA measurements: baseline measurement and diagnostic measurement. The procedure and precautions to generate a good measurement are both the same. However, there is a difference in the motivation for the tests in each categories [73].

A.3.1 FRA Baseline Measurements

The baseline FRA measurement is performed in either the factory or the field and provides information that can be used for future need. The several distinct reasons why this measurement should be carried out are [73]:

- To provide a standard of comparison for future diagnostic FRA measurements.
- Quality assurance to test the integrity of the winding structures and the core.
- Transportation diagnostics prior to relocation.
- Required by customer specification.

It is of great important to document the methods or mode of connection when performing baseline FRA measurements. If different modes are used for the two categories (i.e., baseline and diagnostic measurements), it may affect the diagnostic results and effective comparison may not be achieved. Therefore, it is important to document the test configuration and connections for future test repeatability.

A.3.2 FRA Diagnostic Measurements

The following are the main reasons why this category of FRA application measurement should be carried out [73]:

- Verification that no damage occurred during a short-circuit test.
- Evaluation of used or spare induction motor.
- Condition assessment of older induction motor.
- Relocation of induction motor.
- Routine diagnostic purposes.

It is of great interest to match the setup and instrumentation parameters used for the baseline measurements.

Appendix B

B.1 LabVIEW Code

LabVIEW is a programming language used for acquiring data from instruments (e.g., National instruments (NI)), process data (e.g., transform, filter), analyse data and control instruments and equipment. A LabVIEW program consist of two windows: the front panel and block diagram window.

B.1.1 Front Panel for signal acquisition and monitoring

The front panel window used in this study reads the voltage from the signal generated or programmable power supply, the voltage across the device under test (DUT), process the data by calculating the current through the DUT, and transform the voltages and currents in time domain to frequency domain to calculate the impedance at different supply frequency.

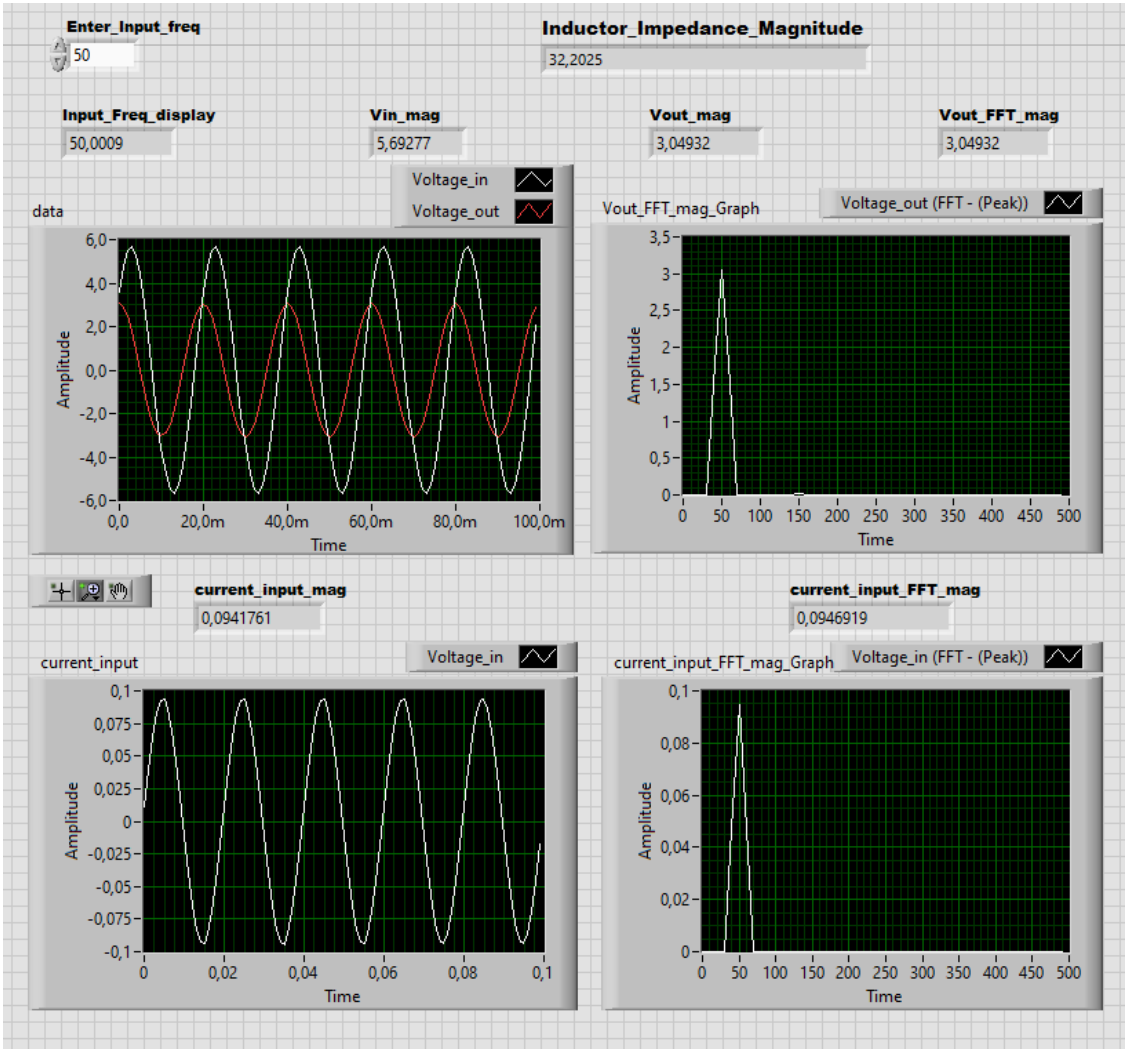

B.1.2 Block diagram for signal acquisition and data processing

Block diagram window consist of block objects which includes terminals, subVIs, functions, constants, structures, and wires, which transfer dtat among other block diagram objects. This is where data processing takes place.

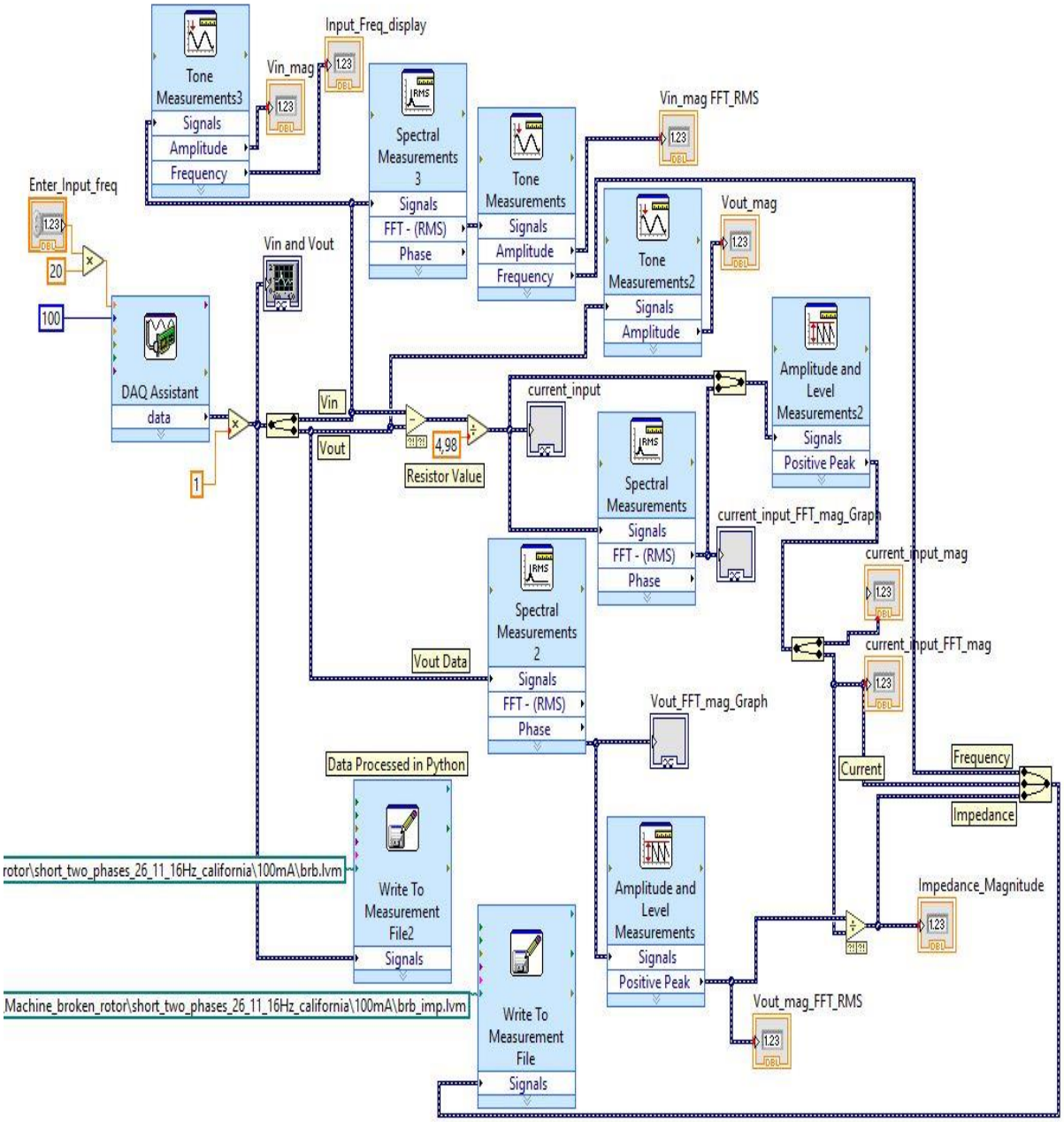

Appendix C

C.1 Python Code

The raw data acquired from the NI DAQ device were further processed using python programming language to extract the impedance information for the device under test.

The below snippet was use for impedance extraction in laminated core inductor, SCIM at different fault conditions.

Processing raw signal data from the DAQ

```
import numpy as np
import pandas as pd
import matplotlib. pyplot as plt
from scipy import fftpack
```

For a signal at a particular frequency

```
signal_data  = pd.read_csv('healthy_20_08/healthy_1.lvm',
                   delimiter='\t',
                   names=['time', 'v_in', 'v_out'],
                  decimal=',')
# Get this values
voltage_in = []; voltage_out = []; current_in = []; complex_z = []
z_mag = []; freq = []; z_phase_rad = []; z_phase_deg = []

def data_processing(signal_data):
    signal_data.dropna(inplace=True)
    signal_data.drop_duplicates(subset=['time'], inplace=True, keep='last')
    time = signal_data.time.values
    v_in = signal_data.v_in.values
    v_out = signal_data.v_out.values

    # current through the circuit
    i_in = (v_in - v_out)/47
    signal_data['i_in'] = i_in
    #print(signal_data.head())

    plt.figure(figsize=(15, 10))
    plt.subplot(221)
    plt.plot(time, v_in, linewidth=2, label="V_in")
    plt.plot(time, v_out, label="V_L")
    plt.plot(time, i_in, label="I_in")
    plt.xlabel('Time (s)', fontsize=14)
    plt.ylabel('Inductor voltage (V)', fontsize=14)
    plt.grid(True)
    plt.legend(loc='upper right')

    N = len(time)
```

```
# At what intervals time points are sampled
samplingInterval = time[1]-time[0]

# The FFT of the signal
sig_fft_v_in = fftpack.fft(v_in)
sig_fft_v_out = fftpack.fft(v_out)
sig_fft_i_in = fftpack.fft(i_in)

# And the power (sig_fft is of complex dtype)
power_v_in = np.abs(sig_fft_v_in)*2/N   # Normalize amplitude
voltage_in.append(power_v_in.max())  # input voltage magnitude
power_v_out = np.abs(sig_fft_v_out)*2/N   # Normalize amplitude
voltage_out.append(power_v_out.max())  # output voltage magnitude
power_i_in = np.abs(sig_fft_i_in)*2/N   # Normalize amplitude
current_in.append(power_i_in.max())  # input current magnitude

# # The corresponding frequencies
sample_freq = fftpack.fftfreq(v_in.size, samplingInterval)
```

```
plt.subplot(222)
plt.plot(sample_freq[range(int(len(sample_freq)/2))], power_v_in[range(int(len(sample_freq)/2))])
plt.xlabel('Frequency [Hz]', fontsize=14)
plt.ylabel('V_in', fontsize=14)
plt.grid(True)

plt.subplot(223)
plt.plot(sample_freq[range(int(len(sample_freq)/2))], power_v_out[range(int(len(sample_freq)/2))])
plt.xlabel('Frequency [Hz]', fontsize=14)
plt.ylabel('V_out', fontsize=14)
plt.grid(True)

plt.subplot(224)
plt.plot(sample_freq[range(int(len(sample_freq)/2))], power_i_in[range(int(len(sample_freq)/2))])
plt.xlabel('Frequency [Hz]', fontsize=14)
plt.ylabel('I_in', fontsize=14)
plt.grid(True)

impedance_mag = power_v_out.max()/power_i_in.max()
z_mag.append(impedance_mag)   # Impedance Magnitude
#print("impedance in frequency domain ", impedance_mag)

# Get the index of the maximum output voltage amplitude
index_max_v_out = (list(power_v_out)).index(power_v_out.max())

# Get the index of the maximum input current amplitude
index_max_i_in = (list(power_i_in)).index(power_i_in.max())

# Get the corresponding complex number
complex_v_out = sig_fft_v_out[index_max_v_out]
complex_i_in = sig_fft_i_in[index_max_i_in]

# Get the complex impedance
complex_impedance = complex_v_out/complex_i_in
complex_z.append(complex_impedance)   # Impedance complex value
#print("The complex impedance and it's magnitude is ", complex_impedance, abs(complex_impedance))

# Get the impedance phase
z_phase_rad.append(np.angle(complex_impedance))
z_phase_deg.append(np.angle(complex_impedance, deg=True))

# Print the input frequency
frequency = sample_freq[index_max_v_out]
freq.append(frequency)
```

```
# Create DataFrame
df_healthy = pd.DataFrame([])
df_healthy['frequency'] = freq
df_healthy['voltage_in'] = voltage_in
df_healthy['voltage_out'] = voltage_out
df_healthy['current_in'] = current_in
df_healthy['impedance_complex'] = complex_z
df_healthy['impedance_magnitude'] = z_mag
df_healthy['impedance_phase_rad'] = z_phase_rad
df_healthy['impedance_phase_deg'] = z_phase_deg
df_healthy['inductance'] = df_healthy['impedance_complex'].values.imag/(2*np.pi*df_healthy.frequency)
#df_healthy.drop_duplicates(subset=['frequency'], inplace=True, keep='last')
df_healthy
```

	frequency	voltage_in	voltage_out	current_in	impedance_complex	impedance_magnitude	impedance_phase_rad	impedance_phase_deg	inductance
0	0.500000	5.001570	0.295051	0.100173	2.928285+0.317157j	2.945410	0.107887	6.181494	0.100954
1	1.000000	5.001741	0.299615	0.100185	2.921095+0.641112j	2.990622	0.216051	12.378816	0.102036
2	5.000000	5.011883	0.437906	0.100113	2.958662+3.221694j	4.374127	0.827932	47.437003	0.102550
3	10.000000	5.037094	0.709688	0.099917	2.999999+6.438119j	7.102773	1.134738	65.015682	0.102466
4	20.000000	5.130852	1.313091	0.099215	3.087789+12.869622j	13.234864	1.335319	76.508141	0.102413
...	...	...	...	...	...	...	...	...	...
56	80645.161290	9.968382	9.952694	0.002031	782.754974-4838.329451j	4901.238335	-1.410404	-80.810194	-0.009549
57	86206.896552	9.806528	9.790801	0.002202	652.631473-4397.827358j	4445.988452	-1.423473	-81.558989	-0.008119
58	90909.090909	9.876017	9.859602	0.002361	594.940980-4133.951917j	4176.543215	-1.427862	-81.810463	-0.007237

```
#plt.figure(figsize=(10, 7))
plt.semilogx(df_healthy['frequency'], df_healthy['impedance_magnitude']*0.001, label='Healthy')
plt.semilogx(df_1turn['frequency'], df_1turn['impedance_magnitude']*0.001, label='1 turn')
plt.semilogx(df_4turns['frequency'], df_4turns['impedance_magnitude']*0.001, label='4 turns')
plt.semilogx(df_8turns['frequency'], df_8turns['impedance_magnitude']*0.001, label='8 turns')
# plt.semilogx(df_10turns['frequency'], df_10turns['impedance_magnitude']*0.001, '#9467bd', label='10_turns')
plt.xlabel("Frequency [Hz]", fontsize=14)
plt.ylabel("$Z_{L}$ [k\u03A9]", fontsize=14)
plt.grid(which='both')
plt.legend()
plt.tight_layout(pad=0.4, w_pad=0.5, h_pad=1.0)
# An inner plot to show the peak frequency
axes = plt.axes([0.35, 0.35, 0.3, 0.5])
plt.semilogx(df_healthy[df_healthy['frequency'] >500]['frequency'], df_healthy[df_healthy['frequency'] >500]['impedance_magnitud
e']*0.001, label='Healthy')
plt.semilogx(df_1turn[df_1turn['frequency'] >500]['frequency'], df_1turn[df_1turn['frequency'] >500]['impedance_magnitude']*0.00
1, label='1_turn')
plt.semilogx(df_4turns[df_4turns['frequency'] >500]['frequency'], df_4turns[df_4turns['frequency'] >500]['impedance_magnitude']*
0.001, label='4_turns')
plt.semilogx(df_8turns[df_8turns['frequency'] >500]['frequency'], df_8turns[df_8turns['frequency'] >500]['impedance_magnitude']*
0.001, label='8_turns')
# plt.semilogx(df_10turns[df_10turns['frequency'] >500]['frequency'], df_10turns[df_10turns['frequency'] >500]['impedance_magnit
ude']*0.001, label='8_turns')
#plt.setp(axes, yticks=[]) # this removes the yticks and its values
#plt.title("Impedance plot")
```

Appendix D

D.1 Diagnosis using Statistical Indicators

The four statistical indicators explained in section 3.3.5 are applied to the impedance response experimental results for each of the DUT (LACOIN, SCIM1, and SCIM2 with and without rotor) to find the most accurate and sensitive ones for diagnosis. These results are shown in Table's D.1-D.3. The correlation coefficient (CC) is designed to tend towards zero if two responses are uncorrelated and towards one if they are correlated (similar). This can be seen in each of the tables where CC of the DUT in healthy condition is unity and less than one under fault conditions. The higher the severity the more CC values approaches zero. For the other three indicators i.e., standard deviation (SD), maximum absolute difference (DABS) and absolute sum of logarithm error (ASLE), the values are zero when the DUT is in good condition as this basically determines the distance between two impedance responses. The higher the deviation from the baseline impedance responses, the higher the indicator values. The effect of rotor on the impedance response could also be seen from each of the indicator. The values of the indicators (SD and DABS) without rotor are almost twice the values of the indicator (SD and DABS) with rotor which reflects reduction in impedance responses. However, based on the data extracted from the impedance response for each of the DUT, all the four statistical indicators are good performance for SFRA assessment.

Table D.1: Table of statistical indicators for LACOIN impedance response

LACOIN Conditions	Statistical Indicators			
	CC	SD	DABS	ASLE
Healthy	1.000	0.000	0.000	0.000
1% inter-turns	0.799	3863.266	1758.867	0.130
3% inter-turns	0.531	5537.947	2970.045	0.386
6% inter-turns	0.508	5626.305	3059.353	0.505

Table D.2: Table of statistical indicators for SCIM1 impedance response

SCIM1 Conditions	Statistical Indicators			
	CC	SD	DABS	ASLE
Healthy	1.0000	0.000	0.000	0.000
5% inter-turns	0.9785	1049.00	492.826	0.119
7% inter-turns	0.9768	1114.46	521.182	0.133

Table D.3: Table of statistical indicators for SCIM2 impedance response

SCIM2 Conditions		Statistical Indicators			
		CC	SD	DABS	ASLE
Healthy	*Without rotor*	1.0000000	0.0000	0.000	0.0000
	With rotor	1.0000000	0.0000	0.000	0.0000
2% inter-turns	*Without rotor*	0.9985321	1026.93	648.921	0.0692
	With rotor	0.9993748	546.083	390.216	0.0648
4% inter-turns	*Without rotor*	0.9984224	1115.75	705.948	0.0802
	With rotor	0.9993225	578.871	413.736	0.0711
6% inter-turns	*Without rotor*	0.9982284	1295.95	797.956	0.0828
	With rotor	0.9993219	593.969	426.649	0.0735
8% inter-turns	*Without rotor*	0.9975536	1409.83	903.244	0.1122
	With rotor	0.9986753	815.144	583.175	0.1029